BOLT BERANEK AND NEWMAN INC

CONSULTING • DEVELOPMENT • RESEARCH

NASA CR-111960

UNSTEADY AERODYNAMIC LOADS DURING REENTRY OF THE STRAIGHT-WING ORBITER CONFIGURATION

Hanno H. Heller
D. Graham Holmes

Bolt Beranek and Newman Inc.
50 Moulton Street
Cambridge, Massachusetts 02138

Final Report No. 2118
September 1971
Contract No. NAS1-9559-5

Submitted to:

National Aeronautics and Space Administration
Langley Research Center
Langley Station
Hampton, Virginia 23365

Attention: Mr. Harry L. Runyan, Jr.
Mail Stop 242

NASA CR-111960

UNSTEADY AERODYNAMIC LOADS DURING REENTRY OF THE STRAIGHT-WING ORBITER CONFIGURATION

By Hanno H. Heller
D. Graham Holmes

Prepared under Contract No. NAS1-9559-5 by

Bolt Beranek and Newman Inc.
50 Moulton Street
Cambridge, Massachusetts 02138

for

NATIONAL AERONAUTICS AND SPACE ADMINISTRATION

TABLE OF CONTENTS

LIST OF FIGURES

LIST OF FIGURES *(Continued)*

page

LIST OF FIGURES *(Continued)*

LIST OF FIGURES *(Continued)*

LIST OF FIGURES *(Continued)*

page

LIST OF TABLES

UNSTEADY AERODYNAMIC LOADS DURING REENTRY OF THE STRAIGHT-WING ORBITER CONFIGURATION

By Hanno H. Heller and D. Graham Holmes
Bolt Beranek and Newman Inc.

SUMMARY

A wind tunnel study was conducted to determine overall levels and spectra of the pressure fluctuations acting on the leeward side of the straight-wing space shuttle orbiter configuration during reentry. Scaled models (1:250 and 1:125) at 60° attitude were exposed to free-stream flow speeds corresponding to Mach numbers of 4 and 2.5. Tests on these orbiter models were supplemented by a study of pressure fluctuations on an 8° half-angle cone/flat-base configuration at free-stream Mach numbers of 4, 2.5, and 0.67.

The results of these studies, and comparison with data available in the open literature, suggest that, at free-stream Mach numbers of 4 and 2.5, the values of the overall pressure-coefficient $\left[(p_{rms})_{OA} \Big/ (1/2\rho U^2)\right]$ are 0.03 nearly everywhere on the leeward side of the fuselage, and are about 0.1 in areas affected by wing wakes and wing shocks, where p_{rms} is the fluctuating pressure, ρ is the density, and U is the free-stream velocity. Although no data was obtained at transonic speeds, levels are likely to be even higher at reentry speeds near Mach number 1.

INTRODUCTION

At the time this study was initiated (May 1970), the two prime orbiter configurations being considered for the newly proposed space shuttle transportation system were (1) the Low Cross-Range Orbiter with straight wings proposed by the NASA Manned Spacecraft Center (Fig. 1a) and (2) the High Cross-Range

Orbiter with delta wings proposed by the North American Rockwell Corporation (Fig. 1b). Since then, the straight-wing orbiter concept has been dropped in favor of the delta-wing concept, which represents the more versatile vehicle.

However, since the initiation of the space shuttle development program, many studies pertaining to straight-wing configurations have been performed; these are still of great scientific value, if only to emphasize the respective advantages and disadvantages of the two configurations.

The state of the art pertaining to space shuttle vehicles as of mid-1970 is documented in the "Space Transportation Systems Technology Symposium," NASA Tech. Memorandum X-52876 [1]. The "Space Shuttle Technology Conference" held at the NASA-Langley Research Center in March 1971 summarizes the state of the art as of early 1971.

One major problem area of the dynamics of shuttle vehicles is the unsteady aerodynamic loads and the resulting structural response during various mission phases. The purpose of this study was to assess the fluctuating pressure characteristics from aerodynamic sources acting on the straight-wing orbiter configuration during the reentry phase.

Background and Objective of Study

Within a typical mission profile, the space shuttle undergoes three critical phases during which high unsteady loads can be expected: lift-off, early boost, and reentry. While the relatively short lift-off phase is characterized by high *acoustic* intensities associated with the rocket exhaust, the boost phase and the comparatively long reentry phase are characterized by large unsteady

aerodynamic loads acting on the exterior vehicle structure. It is yet to be determined which of these three phases is the most critical with respect to structural design.

This study investigated the characteristics of the fluctuating pressure field at various strategic locations on the leeward side of the low cross-range orbiter (LCRO) during the reentry phase. Small-scale models of the LCRO were exposed to flow in a supersonic wind tunnel. Microphones were used to measure surface pressure spectra at several Mach numbers and Reynolds numbers. Additional information was obtained through Schlierenoptical and oil-flow visualization.

Because of the complex shape of the configuration under test, a supplementary pilot study was conducted on a slender pointed cone with a flat base to relate the data obtained under well-behaved flow to the data obtained on the orbiter configuration. Our results are therefore presented in two parts. Part I of this report deals with experiments on the slender-cone/flat-base configuration; Part II deals with the low cross-range orbiter configuration. The implications of the slender-cone study with regard to interpretation of the results of the LCRO study are discussed in Part III. Some information on pressure field convection velocities on the models was obtained through correlation measurements. Data are presented in the Appendix.

Aerodynamic Loads During Orbiter Reentry

The orbiter reenters the earth's atmosphere at a free-flight Mach number of approximately 20 and at a high angle of attack — on the order of 60°. Figure 2 shows predicted dynamic pressures, q, and unit Reynolds numbers, Re/ft, along the reentry trajectory.

Early in the reentry phase there is a transition along the windward side from laminar to turbulent flow at rather low dynamic pressures. Flow behind the bow-shock heats up quickly, thus effectively reducing the local Mach number along the vehicle skin. The rapid increase in dynamic pressure during reentry increases the aerodynamic loads on the vehicle quite dramatically. While the forward (windward) vehicle structure may experience considerable yet not necessarily damaging unsteady pressures because the flow is essentially attached, the separated flow on the rearward (leeward) vehicle structure causes very strong fluctuating pressures that might very well represent the most damaging load during the entire mission. Conditions during reentry are therefore critical for two reasons: (1) high temperatures occur at the same time as high fluctuating pressures, (2) the combined aerodynamic and thermal loads last for an extended period of time (typically 20 min) as compared to the rather short load peaks during lift-off and boost.

Loads due to attached and separated turbulent flow will peak in the transonic speed range, where dynamic pressures are very high. Additional loads due to oscillating shocks and shock/boundary-layer interaction will also occur over a brief time period in the transonic flight regime.

PART I: FLUCTUATING PRESSURE CHARACTERISTICS ON SLENDER-CONE/FLAT-BASE CONFIGURATION

EXPERIMENTAL SET-UP

Wind Tunnel and Model Support

The experiments were conducted in the Massachusetts Institute of Technology Naval Supersonic Wind Tunnel, a continuous flow unit with a test section 18 in. wide by 24 in. high.

The model, an 8° half-angle flat-base cone, was designed to provide preliminary data with regard to the effects of Mach number, Reynolds number, angle of attack, etc., on the pressure fluctuations. Although this configuration does not resemble any of the proposed full-scale shuttle vehicles, it does retain two essential sources of the unsteady aerodynamic loads:

1. fluctuating pressures in the attached turbulent boundary layer at the front of the cone and

2. pressure fluctuations in the separated base flow.

Tests were conducted at Mach numbers 4, 2.5, and 0.67, over a wide range of stagnation pressures, and at angles of attack of 0° and 10°. Measurements of fluctuating pressures were made with microphones located on the front of the cone and on the flat base. Supplementary measurements included static pressure measurements on the cone surface and the flat base and Pitot-tube surveys of the boundary layer on the cone forebody. Schlieren photographs of the flow were taken as necessary.

Model

Figure 3 shows the cone model installed in the MIT tunnel. Figure 4 presents a schematic of the configuration. Several interchangeable nose sections were used: a smooth section in tests

calling for natural boundary layer transition, and other sections incorporating such boundary-layer tripping provisions as a band of No. 40 carborundum grit, (about 1 in. wide, located 2-1/2 in. to 3-1/2 in. aft of the tip) and a small-diameter wire ring (about 3 in. aft of the tip).

The simplest model support available in the MIT tunnel is a conventional sting. However, although there is no mention in the available literature of the effect of a sting on the unsteady component of the base pressure, such an effect probably exists. Therefore, we decided to support the model with a streamlined pylon bolted to the tunnel floor. The supporting pylon was rigidly attached to the cone mid-section at an angle of 45°. The junction between the cone and the pylon was faired so as to produce as little flow disturbance as possible. Angle-of-attack changes were made via a wedge at the foot of the pylon. With the wedge in place, the angle of attack was 0°; without the wedge, the angle of attack was 10°.

Tests were carried out to assess the interference effect of the pylon on the unsteady base pressures and, using a dummy sting, to estimate any sting interference effects that could have occurred.

Instrumentation

Free-Stream Data. — The free-stream data recorded at the tunnel console were the stagnation temperature, the stagnation pressure, and the static pressure. The static pressure was recorded only at subsonic speeds. At supersonic speeds, the low static pressures may better be calculated from the free-stream Mach number and the stagnation pressure.

Boundary-Layer Data. — A small Pitot tube, mounted near microphones #3 and #4 and traversing the boundary layer, was used to determine the boundary-layer profiles. The local Mach number M was computed from the Pitot pressure P_1 and the static pressure P_2 (obtained by means of a static pressure tap located at the surface immediately under the Pitot tube) with the Rayleigh Pitot formula:

$$P_1/P_2 = \left[1 + \frac{\gamma-1}{2} M^2\right]^{\gamma/\gamma-1} ; \quad M \leq 1$$

$$P_1/P_2 = \left[\frac{\gamma+1}{2} M^2\right]^{\gamma/\gamma-1} \Bigg/ \left[\frac{2\gamma}{\gamma+1} M^2 - \frac{\gamma-1}{\gamma+1}\right]^{1/\gamma-1} ; \quad M \geq 1 ,$$

where γ represents the ratio of specific heats.

The velocity U in the boundary layer is then given by

$$U = a_0 M \left[1 + \frac{\gamma-1}{2} M^2\right]^{-\frac{1}{2}} ,$$

where a_0 is the stagnation sound speed, which one may calculate from a_0 (ft/sec) = $49.02(T_0)^{\frac{1}{2}}$, where T_0 is the stagnation temperature in degrees Rankine. Two adequately valid assumptions are implicit in these formulae: (1) the static pressure is constant across the boundary layer, and (2) the stagnation temperature is constant across the layer and equal to the measured tunnel stagnation temperature.

Fluctuating Pressure Data. — Fluctuating pressures were measured using BBN 1/10-in. diameter piezoelectric microphones, as shown in Fig. 4. Microphones 1, 2, 3, 4, and 6, which were constructed specially for this program, had a frequency response flat

to 100 kHz. Microphones 5, 7, 8, and 9 had a frequency response flat to 20 kHz. Impedance matching electronics were incorporated in each microphone case.

Data Analysis. — Microphone signals were reduced to 1/3-octave band spectra in the frequency range from 160 to 80,000 Hz via a General Radio analyzer used with an X-Y plotter. For correlation measurements, tape recordings were made with an Ampex 1300 tape recorder operating in a direct record mode on a maximum of five channels and with a frequency response to 500 kHz.

Vibration Data. — An accelerometer was mounted in the cone mid-section, its sensitive axis in a horizontal plane and normal to the cone axis. This was the expected direction of maximum cone vibration, due to pylon bending. The accelerometer output was monitored with the same instrumentation used for the microphone signals.

RESULTS

Tunnel Blockage

No problems were experienced in starting the tunnel at either supersonic Mach number — 4 or 2.5. Static pressure data on the model surface at subsonic speeds indicated that critical Mach numbers were not approached.

Boundary-Layer Tripping

Figures 5 — 7, Schlieren photographs taken at Mach number $M = 4$, at angle of attack $\alpha = 0°$, and at stagnation pressures near 20 psi, indicate the effects of boundary-layer tripping. Figure 5, taken with no trip, shows an essentially laminar boundary layer,

with evidence perhaps of a burst of turbulent flow near the upper trailing edge of the model. Figure 6, taken with the grit trip, shows transition occurring about two thirds of the way back from the tip. Figure 7, taken with the ring trip, shows transition less than half-way back from the tip.

It was also found that at the subsonic Mach number 0.67, transition occurred immediately behind the ring.

Note, however, that assessing transition locations from Schlieren photographs is a very qualitative process. The estimated transition Reynolds numbers are 2×10^6 with no trip, 1.45×10^6 with the grit trip, and 1.15×10^6 with the ring trip. The ring trip being the more effective, was used in all subsequent tests.

Boundary-Layer Profiles

A *turbulent* boundary layer profile differs distinctly in shape from a *laminar* profile. Therefore, comparing spectra obtained at the same conditions for both kinds of boundary layers helps one to extract surface-flow-related pressure signals from acoustic background noise. Under a laminar boundary layer, microphone signals are generated by tunnel background noise, while signals generated under a turbulent boundary layer contain both fluctuating surface-pressure information and tunnel background noise. In order to interpret the fluctuating pressure data correctly, a boundary-layer profile was obtained in each test run.

A typical profile of turbulent-boundary-layer Pitot pressure is shown in Fig. 8 for a freestream Mach number of 4. (The millivolt scale is directly proportional to Pitot pressure.) The edge of the boundary layer is seen to be quite sharply defined, in this case 0.190 in. from the wall. Allowing another 0.010 in. for the finite thickness of the probe tip, the boundary-layer thickness is seen to be $\delta = 0.200$ in.

Displacement thickness δ^* and momentum thickness Θ are determined in the following way: First, the transducer output is converted to values of the ratio of Pitot pressure to static pressure, either by using the Pitot calibration and the measured static pressure (assumed constant through the boundary layer), or by using the estimated Mach number outside the boundary layer. Then, the Rayleigh Pitot formula is applied to produce a profile of local Mach number. On the assumption of constant total temperature through the layer, the local Mach number profile is converted to a boundary-layer profile.

Applying this procedure to the data in Fig. 8 produces the boundary-layer profile in Fig. 9. The boundary-layer profile follows a nondimensional curve

$$\frac{u}{U_\infty} = \left(\frac{y}{\delta}\right)^{1/N}$$

where the exponent N has been chosen as 10.0 to give the best fit (based on a logarithmic plot of the data).

Then, δ^* and θ are computed using the information given in Ref. 2. For the data of Fig. 9, one finds $\delta/\delta^* = 0.326$, and $\theta/\delta = 0.046$, so that $\delta = 0.200$ in., $\delta^* = 0.065$ in., and $\theta = 0.009$ in.

Table I summarizes the values of δ, δ^*, and θ, together with free-stream Mach number M_∞, cone-surface Mach number M_c, (computed either for supersonic flow past a cone or in subsonic flow from the measured static pressure at the probe), and the stagnation pressure P_0.

TABLE I

BOUNDARY-LAYER PARAMETERS

M_∞	M_c	P_0 (psi)	Trip	δ in.	δ^* in.	θ in.
0.67	0.77	12	none	0.110		
0.67	0.78	5	ring	0.16	0.027	0.016
2.5	2.35	15	ring	0.19	0.047	0.013
2.5	2.35	15	none	0.11	0.036	0.009
4.0	3.7	25	none	0.15	0.049	0.007
4.0	3.7	28	grit	0.21	0.068	0.010
4.0	3.7	30	ring	0.20	0.065	0.009

To base general conclusions on spectra measured for tripped boundary layers, one must establish how these relate to spectra for untripped boundary layers. At $M = 4$ and high stagnation pressures, turbulent boundary layers were obtained at the Pitot probe, with and without a trip. The profiles are compared in Fig. 9,

along with a transitional profile obtained at lower stagnation pressure. The collapse of the profiles is seen to be excellent. The good agreement of the mean profiles of tripped and untripped boundary layers is no guarantee that the fluctuating pressure characteristics of the boundary layers will similarly agree. However, Ref. 3 suggests that, in practice, agreement of the mean profiles is sufficient to secure agreement of the pressure fluctuation characteristics of boundary layers.

Fluctuating Pressure Data

Tunnel Background-Noise Interference. — A major difficulty in measuring surface pressure fluctuations on high-speed wind-tunnel models is that of distinguishing surface pressure fluctuations on the model from the high acoustic background levels in the tunnel. Only in special cases, such as test of a resonant cavity, for example, will the desired signal be much more intense than the background. In other cases, differentiation is made possible by situations where the characteristic frequencies of the desired signal differ greatly from the characteristic frequencies of the background noise. A third possibility is that the characteristic length scales of the signal and the background noise may be quite different so that cross-correlation of signals from several microphones could be used to distinguish between them.

In determining surface pressure fluctuations under a turbulent boundary layer on a small wind-tunnel model, one relies on the fact that model boundary-layer thicknesses will be thin (in this case, near 0.15 in.) whereas the tunnel wall boundary-layer thickness is relatively thick ("over" 1.0 in.). Thus, characteristic frequencies of the fluctuations in the model boundary

layer are much higher than in the wall boundary layer. Figure 10 shows 1/3-octave band spectra of the pressure fluctuations at cone microphone #4, at M = 4, and at two different stagnation pressures. In each case, the signals come partly from pressure fluctuations in the model boundary layer and partly from radiation from the tunnel wall boundary layers. It is a reasonable assumption that as long as the tunnel wall boundary layer is turbulent, the tunnel background noise scales with the dynamic pressure.

In Fig. 11, the two spectra are scaled with the dynamic pressure with the free-stream dynamic pressure on the left ordinate and with the cone-surface dynamic pressure on the right ordinate. Below 20 kHz the two spectra are similar; above 20 kHz the divergence is marked. At P_0 = 10 psi the model boundary layer is laminar; at P_0 = 25 psi the model boundary layer is turbulent. Thus, the additional energy above 20 kHz at 25 psi must represent model boundary-layer pressure fluctuations. We see two characteristic "haystack" spectra — one from the tunnel wall peaking near 5 kHz, and one from the model boundary layer, peaking near 80 kHz.

Data Analysis. — Boundary-layer dimensions compared to microphone sensitive areas suggest that finite-size corrections according to Corcos [*4*] should be applied to the high-frequency data. The dashed line superimposed on the high-frequency data represent corrected turbulent-boundary-layer spectra.

Extrapolation of the corrected spectra towards higher frequencies was based on a nondimensional curve suggested in Ref. 5 and shown in Fig. 12. Under the assumption that the spectra

observed in the present study are represented by this nondimensional curve, one can obtain the overall level of a spectrum by adding 11 dB to the peak 1/3-octave band level. The overall level of the spectrum is then -43.5 dB *re* the dynamic pressure on the cone surface q_c — i.e., p_{rms}/q equals 6.66×10^{-3}, a value that is close to that suggested by Houbolt [*6*] but much higher than that suggested by Lowson [*7*], who correlated data obtained on flat plates or tunnel walls.

One might suspect that in many investigations the spectral peak has been missed because of instrumentation limitations and, thus, that lower levels were obtained. It is also possible, however, that the flow on the cone surface in the present investigation was not fully turbulent yet, but that it was still in a transitional stage. Pressure fluctuations under a transitional boundary layer are known to be higher than under a fully developed turbulent boundary layer.

Boundary Layer Tripping. — In Fig. 13 — 17, levels are again normalized with free-stream and cone-surface dynamic pressures, this time with regard to various boundary-layer trip conditions. One-third octave band spectra obtained at microphones #3 and #4 (close to the base, but on the cone forebody) are presented for free-stream Mach numbers M_∞ of 4, 2.5, and 0.67. Cone-surface Mach numbers M_c were 3.7 for $M_\infty = 4$, 2.35 for $M_\infty = 2.5$, and 0.8 for $M_c = 0.67$. In these figures one sees — in addition to the two haystacks shown in Fig. 11 and described above — some discrete low-frequency components, probably due to compressor and valve noise propagating through the test section. Note that the data at $P_0 = 2$ psi in Fig. 13 for $M_\infty = 4$ are likely to represent background-noise data with a laminar tunnel wall boundary layer.

Figure 14 shows spectra obtained at $M_\infty = 4$ with the ring trip located at the forward tip of the cone. The normalized turbulent-boundary-layer spectra at the high-frequency end are virtually identical to those shown in Fig. 13 where no tripping device was used.

Figure 15, which shows data obtained at $M_\infty = 2.5$ with the ring trip, is to be interpreted in a similar fashion. The 5-psi data, which show higher levels than the 15 psi data, are probably still affected by transitional flow. For further interpretation, however, data at $P_0 = 15$ psi were used, and Corcos' correction was applied.

Figures 16 and 17 present data at $M_\infty = 0.67$ for both the untripped (Fig. 16) and the tripped (Fig. 17) configurations. The trip caused the boundary layer to become turbulent at $P_0 = 5$ psi, in contrast to the obviously still laminar boundary layer for the untripped configuration at the same stagnation pressure.

Nondimensional Overall Levels. — Normalizing the overall levels obtained at the 3 Mach numbers, with the dynamic pressure on the cone yields the following results.

TABLE II

NONDIMENSIONAL OVERALL LEVELS

M_c	0.8	2.35	3.7
Overall (p_{rms}/q)	6.3 to 6.7 $\times 10^{-3}$	5.6×10^{-3}	4.2 to 6.66 $\times 10^{-3}$

These levels are about halfway between those predicted by Houbolt [6] and those predicted by Lowson [7]. Figure 18 shows the present test results in the context of Houbolt's and Lowson's predictions.

Nondimensional Peak Frequencies. — A nondimensional pressure fluctuation spectrum can be obtained by scaling the pressure fluctuation frequencies with the local velocity outside the boundary layer, U_c, and some boundary layer length scale. Various authors have suggested using δ, δ^*, and θ. Table III shows estimated spectral peak frequencies scaled with each of these three parameters.

TABLE III

NONDIMENSIONAL PEAK FREQUENCIES

M_∞	P_o (psi)	Trip	f_{peak} (Hz)	U_c ft/sec	(f_p/U_c) times		
					δ	δ^*	θ
0.67	12	None	100,000	820	1.0		
	5	ring	80,000	825	1.3	0.22	0.13
2.5	15	None	90,000	1820	0.78	0.193	0.053
		ring	160,000	1820	0.8	0.165	0.066
4.0	25	None	200,000	2220	1.13	0.367	0.052
	28	grit	90,000	2220	0.7	0.23	0.034
	30	ring	120,000	2220	0.92	0.3	0.0415

Figure 19 shows a plot of normalized peak frequencies vs Mach number. With increasing Mach number, use of the momentum thickness θ results in a relatively strong decrease of the

normalized peak frequency and use of displacement thickness δ^* results in a slight increase; using the boundary-layer thickness δ, however, seems to give normalized peak frequencies that might be independent of Mach number. On this basis it seems that normalization with boundary-layer thickness probably results in a constant normalized peak frequency, which could be represented by $f_{peak} \cdot \delta/U \approx 1$ for $0.8 < M < 3.7$.

Lowson also suggested the use of δ rather than δ^*, since he found a somewhat better collapse of the data obtained earlier by Speaker and Ailman [*8*]. The boundary layer is appealing as relevant parameter since it might relate to a physical characteristic of the flow — i.e., the largest eddy size — and since it is easy to calculate.

Base Pressure Fluctuation Spectra. — Figure 20 presents fluctuating pressure spectra, obtained at the base of the cone with microphone #9, for all three test Mach numbers and for various stagnation pressures. All spectra exhibit a relatively smooth haystack shape in the frequency regime below 2000 Hz and a peak due to microphone resonance at 50,000 Hz. No explanation is available for the sharp peak at 3150 Hz in the M = 4 spectra. In the following discussion, only the frequencies below 2000 Hz will be considered. This restriction is justified since base pressure spectra are known to exhibit most of their energy at relatively low frequencies.

Normalizing the levels with the dynamic pressure q and the frequencies with the ratio of base diameter and free-stream flow speed causes the spectra to collapse in one nondimensional spectrum for each Mach number. Figure 21 presents normalized 1/3-octave band spectra for three Mach numbers. Normalized pressure

levels p_{rms}/q_∞ are shown as function of Strouhal number. All spectra exhibit a haystack shape with a peak near a Strouhal number of 0.2. The dramatic increase in level with decreasing Mach number is obvious.

The overall levels of the base pressure spectra are given below:

TABLE IV

OVERALL BASE PRESSURE LEVELS

M_∞	0.67	2.5	4
$(p_{rms}/q_\infty)_{overall}$	2.5×10^{-2}	3.5 to 5.6×10^{-3}	0.7×10^{-3}

Figure 22 shows these points together with base pressure data from Eldred [*9*], Robinson [*10*], and earlier BBN work [*11*]. One might assume that base pressure levels reach their highest values at subsonic and transonic speeds and that these values are probably in excess of 5% of the dynamic pressure.

Effects of Angle of Attack. — Figures 23 — 25 show the cone model at a 10° angle of attack at M = 4, 2.5, and 0.67. For each photograph the model was dotted with a mixture of oil and carbon black; the resulting streaks show the circumferential motion in the boundary layer from the windward side of the model towards a pair of separation lines on the leeward side. Figures 26 — 28 indicate how the change to positive angle of attack from zero angle of attack modifies the spectra of the pressure fluctuations at microphone #4 on the leeward side of the cone surface.

Figure 26 shows the spectra at M = 4 normalized with respect to the free-stream dynamic pressure. Laminar and turbulent spectra are shown for $\alpha = 0°$, where tunnel wall and zero pressure gradient model surface effects dominate. The third curve shows the turbulent spectrum obtained at $\alpha = 10°$ where, in contrast to the turbulent spectrum obtained for $\alpha = 0°$, the levels are higher and the peak clearly occurs at a lower frequency. (Note that on the leeward side of the model transition occurs very readily.) Figure 23 indicates that the leeward-side boundary layer is very thick at M = 4, a situation which may account for the lower peak frequency. It is difficult to make any general statement about the higher overall level, in view of the complex three-dimensional nature of the flow on the leeward side of the cone.

Figures 27 and 28 again show the spectra for laminar and turbulent layers at $\alpha = 0°$ and for a turbulent layer at $\alpha = 10°$; however, these data were obtained for M = 2.5 and M = 0.67; at these Mach numbers, the turbulent spectra at $\alpha = 0°$ and $\alpha = 10°$ are indistinguishable. The photographs in Figs. 24 and 25 indicate the same three-dimensional boundary-layer flow and boundary-layer thickening on the leeward side as at M = 4; the reason for the qualitative difference in the spectra at M = 4 and at M = 2.5 and 0.67 is not known.

At supersonic Mach numbers, the effect of angle of attack on the base pressure is largely masked by the pylon-interference effects discussed below. However, at M = 0.67, where pylon interference appears negligible, angle-of-attack effects can be examined.

Figure 29 shows spectra from microphones #5 and #7 on the base, taken at M = 0.67 and P_0 = 12 psi, for $\alpha = 0°$ and $\alpha = 10°$. There is no notable dependence on angle of attack for the relatively narrow angle-of-attack range in this experiment.

Pylon and Sting Interference. — Figure 29 indicates that pylon interference is largely absent at M = 0.67, while Figs. 30 and 31 show the effect of the pylon on the base pressure spectra at M = 4 and M = 2.5 and at zero angle of attack. Levels at the microphones on the base may differ by as much as 10 dB or more, indicating that the pylon interference is quite strong.

The pylon can influence the base flow in two ways — via its turbulent wake or via disturbances to the gross flow about the model. The absence of this strong pylon interference at subsonic speeds supports the idea that the latter effect predominates — i.e., that the shock-expansion system of the pylon impinges on the base.

Tests were run at M = 4 to assess the effect of a dummy sting on the fluctuating base pressures. Figure 32 shows base pressure spectra with and without the sting at a stagnation pressure of 15 psi. At microphone #8, the sting has almost no effect on the spectrum, but at microphone #5, it causes a large increase in the low-frequency spectrum. Clearly, the sting is capable of perturbing the unsteady base flow as much as the pylon does; in fact, any form of model support appears to cause strong interference effects on some parts of the model.

PART II: FLUCTUATING PRESSURE CHARACTERISTICS ON LOW CROSS-RANGE ORBIT CONFIGURATION

EXPERIMENTAL SET-UP

Wind Tunnel

The test set-up was the same as was used for the supplementary slender-cone experiments discussed in Part I.

Models

Two different scale models of the Low Cross-Range Orbiter (LCRO) were tested. Model A was on the scale of 1/250 and was 7 in. long; Model B was of 1/125 scale and was 14 in. long. The plane, elevation, and front views of the LCRO were shown in Fig. 1a; Fig. 33 shows both models mounted in the tunnel test section at attitudes of 60° with respect to the free-stream flow direction to simulate typical reentry flight attitudes. A wedge-shaped pylon supporting the models minimizes interference with the flow field on their leeward side. Model A was a nearly exact geometric replica of the full-scale vehicle. However, on Model B the horizontal tail fins were omitted and the wings were reduced to small-span stubs to decrease the blocking area of the model. This measure was necessary for tunnel start-up, but it also allowed an assessment of the effect of the wings on fluctuating pressure characteristics measured at the wing location.

Instrumentation and Data Acquisition

Each model was instrumented with five 1/10-in. diameter piezoelectric microphones with a frequency response flat up to 100 kHz on the leeward side, and one 1/4-in. diameter piezoelectric microphone with a frequency response flat up to above 20 kHz on the windward side; locations of the microphones, identified by numbers 1 to 6, are shown in Fig. 34. An accelerometer was used to assess

possible interference of vibration with microphone signals. Selection of the following microphone locations was based on the flow-field visualization: Microphone #1 at a separation line (for Model A at M = 2.5); #2 under separated flow and under a turbulent wake; #3 on top of the vehicle under fully separated flow but within the influence region of the wing-associated shocks; #4 and #5 above the wings in an area of highly turbulent flow; #6 on the windward lower surface.

RESULTS

Flow Visualization

Schlierenoptical visualization provided information on shock patterns. Oil flow visualization was used to define surface flow patterns.

Schlierenoptical Visualization. — Figures 35 and 36 show flow past Model A for M = 2.5 and for P_0 = 15 psi (Re/ft = 2.92×10^6) and for M = 4 and for P_0 = 30 psi (Re/ft = 3.18×10^6). In both figures, the bow shock and the wing shock are clearly visible. Flow at the two Mach numbers is phenomenologically similar, although at M = 4, the shock stand-off distance is smaller and the bow shock is inclined more sharply than at M = 2.5. Due to the wing taper, the wing-shock front appears as a light band. The increase of shock stand-off distance towards the model tail shows the effect of the wings and of the horizontal fins. It is probably a fair assumption that flow along the forward portions of the model is correctly modeled, whereas flow near the rear fins might be affected by support interference (although the pylon support itself seems to cause minimal disturbance). All the microphones were located on the forward vehicle portions where good modeling may be expected.

Schlierenoptical visualization revealed a highly unsteady wake being shed from the model's nose tip; this wake, which is visible in Fig. 35, might affect the unsteady-pressure characteristics in the "cockpit" area (microphone #2). Flow past Model B (Fig. 37) is not affected by the stub wings, indicating that they were essentially submerged in the subsonic flow behind the bow shock. Figure 38 shows the shock patterns at M = 4 on both models redrawn to the same scale. The shock stand-off distance for the two models scales perfectly along their forward portions.

Oil Flow Visualization. — Surface flow patterns on both models are shown in Figs. 39, 40, and 41. Attached flow is evident on the windward surface of Model A at M = 2.5 (Fig. 39), and a stagnation point exists near the nose tip. On the leeward side of this model at M = 2.5 (Fig. 40), attached flow is seen along some lower portions near the model nose and separated flow is seen everywhere else. Flow was probably attached along most of the forward leeward portions of Model B at M = 4 (Fig. 41).

The visualization of surface flow and shock patterns identified critical flow areas, such as separation lines or locations where shocks might interfere with attached or separated surface flow. The flow patterns also seem to indicate that no periodic wake shedding took place at these relatively high Reynolds numbers.

Fluctuating Pressure Data

One-third octave band pressure spectra were obtained at all microphone locations for the following experimental conditions:

TABLE V

EXPERIMENTAL CONDITIONS FOR FLUCTUATING PRESSURE MEASUREMENTS

	Model #A and #B			Model #A	
M_∞	4			2.5	
P_0 (psi)	6	15	30	6	15
Re/ft $\times 10^{-6}$	0.54	1.35	2.70	117	2.93
q_∞ (psf)	63.5	159	318	222	555

The spectra obtained for both models were phenomenologically similar. The similarity of surface flow on both models was shown in the Schlieren photographs of Figs. 35 – 37. We therefore use Figs. 42a – f, which show data for Model A at M = 4, to illustrate the general characteristics of the pressure spectra at each microphone location. Data are presented in a seminormalized form: 20 log p_{rms}/q is plotted versus 1/3-octave band center frequencies.

Spectra at microphone locations #1 and #2 (not affected by wings) are almost identical exhibiting a haystack shape. This result indicates that (separated) flow on the afterbody of a blunt body causes essentially identical unsteady-pressure loads, independent of the particular location, unless gross geometric changes affect the flow-shedding characteristics. This data agrees with the findings of Robinson [*10*] on blunt axisymmetric bodies, which are further discussed in Part III.

The spectrum at microphone location #3 clearly indicates the effects of nearby wings — unsteady wake, shedding, and wing-shock oscillations. Comparison of the data obtained for Model A (with wings) and Model B (without wings) indicates that the lower peak in the spectrum in Fig. 42c must be attributed to wing interference.

Full normalization of the data from both models at microphone location #3 (Fig. 43) shows two individual haystack spectra, the lower level of which is very similar to those obtained at locations #1 and #2 (not affected by wing) and the higher of which displays the results of wing interference.

Spectra obtained at microphone locations #4 and #5 (Figs. 42d, e) show a strongly irregular shape, although one can still see the double haystack that appeared more clearly at microphone location #3. Spectra obtained at location #6 (Fig. 42f) must be attributed to tunnel background noise, because the boundary layer was probably laminar at this windward location for the particular tunnel operating conditions.

Figure 44 summarizes all of the results for both models for M = 4. The dimensional plot of spectra for locations #1 and #2 and for location #3 appears in Part III for assumed realistic flight parameters.

Figure 45 shows normalized spectra on Model A at location #2 for M = 4 and M = 2.5. These spectra are seen to be qualitatively similar — i.e., normalized levels are about equal for both Mach numbers at corresponding locations. This data again agrees with Robinson's results [*10*] on blunt axisymmetric bodies.

Some general conclusions that can be drawn from these test results and applied to full-scale vehicles, valid for a Reynolds number range of $0.5 \times 10^6 < Re/ft < 2.5 \times 10^6$ at $M = 4$, are:

1. Levels are highest at a center location on the leeward side of the vehicle in the area of the wings and peak in the nondimensional frequency range $0.1 < S = fD/U_\infty < 0.2$, 30 dB below the dynamic pressure corresponding to a pressure coefficient, $C_p(f)$, in the peak band of about 0.03. If an orbiter configuration with a 30-ft diameter fuselage were facing dynamic pressures of 400 psf, peak 1/3-octave band levels would be just below 150 dB at 15 to 20 Hz.

2. Levels are somewhat lower in the area in front of the wings, where wing interference is either minimal or not present. Levels peak at $0.5 < S < 1$, 40 dB below q corresponding to $C_p(f) = 0.01$. For the same aerodynamic parameters as above, this would mean peak 1/3-octave band levels of about 140 dB at 125 to 160 Hz.

Figure 46 shows two clusters of data points at low frequencies. These spectra were obtained from Model A at microphone location #1, where flow separation is believed to occur at $M = 2.5$. While data collapse is reasonably good, with a typical spread of about 5 dB, observation of the spectrum on the oscilloscope revealed the time history for $P_0 = 6$ psi to be very unsteady: the low-frequency portion of the spectrum changed rapidly between the two slopes as flow changed between attached (lower levels) and separated (higher levels). Note, however, that model-scale and

full-scale Reynolds numbers differ by at least an order of magnitude; hence, flow may not be similar in both cases. However, a similar effect may occur on the full-scale vehicle at some other location and the phenomenon may exhibit similar characteristics in terms of time unsteadiness and level change.

PART III: DISCUSSION

CHARACTERISTICS OF LEEWARD PRESSURE-FLUCTUATIONS

The data on the leeward vehicle structure obtained in this study can be compared with experimental results reported by Robinson *et al* [10]. Robinson exposed axisymmetric blunt bodies to flow in the Mach number range $0.6 < M < 3.5$ and measured overall fluctuating pressures at several locations on the afterbody. Although the LCRO models used in our study are far from axisymmetric, they can be considered very blunt, since they face the oncoming wind with their essentially flat lower fuselage surface. Data obtained on the leeward vehicle surface should thus correspond to those obtained on the afterbody.

Robinson reports that at constant Mach number the observed rms-pressure coefficient $Cp_{rms} = p_{rms}/q$ is rather insensitive to (a) microphone location on the afterbody, (b) Reynolds number, and (c) angle of attack for ±8°. As was illustrated in Fig. 22, Cp_{rms} is highest at subsonic speeds (about 0.04, corresponding to -28 dB relative to q), decreases rather rapidly between M = 1 and M = 2; then stays constant at a value of about 0.005, corresponding to -46 dB relative to q above M = 2. This behavior of blunt-body base pressure is in contrast to the base-pressure behavior of the pointed cone/flat-base configuration, where levels continue to drop at Mach numbers above 2. The latter behavior agrees with results reported by Cassanto and Rasmussen [12], who observed that on the base of a slender pointed cone, normalized *static* base pressures dropped from M = 2.5 to M = 4 by a factor of 1.8, or 5 dB. Above Mach numbers of 4, however, static pressures (referenced to local pressure) remained constant.

In our tests of the LCRO models, fluctuating pressure levels did not change significantly between M = 2.5 and M = 4, in agreement with Robinson's results. If we neglect those portions of the

spectrum that result from wing interference (microphone location #3, in particular, but also #4 and #5), then our *overall* levels (the overall levels must be compared rather than the level at the peak frequency) are about 10 dB (or a factor of 3) higher than Robinson's. This certainly may be attributed to the difference in the configurations studied by Robinson and by us. The important agreement, however, lies in the fact that the levels and spectral characteristics for M = 2.5 and M = 4 are the same.

The difference between slender-pointed-cone configurations and blunt bodies is that in the first case an attached and rather weak shock generated at the cone tip only slightly reduces flow speed; for the Mach numbers considered here (M = 2.5 and 4), flow speed remains supersonic. In the second case, however, the shock generated at the blunt body front reduces the flow to subsonic speeds; thus the *local* shedding processes on the body are probably quite similar for both supersonic Mach numbers.

Comparison of fluctuating pressure spectra for Robinson's and our configuration again yields similar results, in that spectral shape (apart from the wing affected portions) is nearly independent of microphone location.

In summary, fluctuating base pressures (referenced to free-stream dynamic pressure) *on blunt bodies* are highest and constant at subsonic and transonic speed, decrease between M = 1 and M = 2, and then assume a constant value for higher Mach numbers. Fluctuating base pressures on the afterbody of *pointed slender cones* show a maximum at transonic speeds, decrease both towards lower and higher Mach numbers, and seem to level out for Mach numbers above 4.

On the basis of Robinson's results on axisymmetric bodies and data obtained on the slender-cone/flat-base model of the present study, we expect that overall levels observed on the leeward side of the full-scale LCRO at *transonic speeds* should be about 18 dB above levels at supersonic speeds of M = 2.5 and above. Thus, for dynamic pressures of 400 psf, *overall* levels on the forward fuselage could reach 169 dB, and in the wing-affected area close to 177 dB. For dynamic pressures of, say, only 100 psf, levels are 12 dB lower — i.e., 157 and 165 dB, respectively.

SCALING OF RESULTS

It was quite obvious at the initiation of this study that a number of precautions would have to be taken in the design of the experiment as well as in the acquisition and interpretation of the data. For one, scale factors of the models were relatively large, requiring an equally large extrapolation of data to arrive at full-scale values. Scaling of unsteady aerodynamic data for complex configurations is not very well-understood, and the proper scaling parameters need better definitions. However, even if a test could be performed at the correct Mach number and Reynolds number, one could probably not scale frequencies with a ratio of free-stream flow speed and a "representative" linear body dimension in a simple way, particularly for a scaling range of several hundred. While such an approach might be valid for well-behaved (and reasonably well-understood) axisymmetric or two-dimensional flow, complex configurations with highly three-dimensional flow make scaling over a large range somewhat speculative.

The results of this (and, for that matter, of any other) study must therefore be seen in the light of these considerations. However, with due caution, the data and the conclusions derived within

this study are advanced as the best available information to date on the unsteady load characteristics of straight-wing orbiter configurations during the supersonic reentry phase. Tests with large-scale models over an appropriate range of Reynolds numbers and model sizes are ultimately required to understand the processes that underlie scaling of unsteady aerodynamic data, either in flow facilities with low background noise (of which there are none) or on sled-facilities.

Using the results of the present model study, fluctuating pressure spectra at two representative locations on the Low Cross-Range Orbiter for full-scale conditions are presented in Fig. 47. These are the spectra that can be expected with a free-stream Mach number of 4, a vehicle attitude of 60°, free-stream dynamic pressures of 400 psf, and a vehicle width of 30 ft.

APPENDIX

Pressure-Field Correlation Measurements

Characteristic wavelengths of the pressure field exciting aerospace vehicles are a prime parameter for the response of structural components. In the current study, pressure-field correlation measurements of limited scope were performed to obtain gross figures on typical length scales. Obviously, much more refined measurements are necessary because the extremely complex flow field involves attached and separated portions of very unsteady nature. Data were taken on the LCRO Model B at $M = 4$ and $P_0 = 15$ psi, corresponding to $Re/ft = 1.35 \times 10^6$.

Microphone signals were recorded in pairs on two channels of an Ampex tape recorder (type 1300). The pairs of microphones recorded were #1 and #2, #1 and #3, #3 and #4, and #4 and #5. The outputs of the two recorder channels were fed to a pair of B&K Precision Sound Level Meters (type 2203) and Octave Filter Sets (type 1613). The outputs of these, either linear or in a selected octave band, passed to a Princeton Applied Research Corporation Correlation Function Computer (Model 100).* Cross-correlations for each of the pairs and autocorrelations for microphones #1, #2, #3, #4, and #5, were computed for the unfiltered signals and with octave filters centered on 8,000 Hz and 500 Hz.

---

*This is an analog/digital device which computes the auto- or cross-correlation functions of a pair of input signals for a range of one hundred discrete delay times. The range of maximum delay time is from ten sec to 1/10 msec. The instrument produces an output of correlation function versus time delay suitable for display either on an oscilloscope or an X-Y plotter.

Figures A-1 through A-4 show some typical correlations obtained with and without the two filters: autocorrelations for microphone #4 and cross-correlations for microphones #1 and #2. The autocorrelation vertical scale is arbitrary; the cross-correlations are normalized with respect to the autocorrelations at zero time delay, thus reducing them to cross-correlation coefficients.

Frequently, the frequency spectrum of the pressure fluctuations and the spatial wavenumber spectrum can be related via the concept of a convection velocity; the pressure field is viewed as a frozen array of disturbances being convected over the surface of the body. In practice, this convection velocity is to some degree frequency dependent. However, the convection velocity concept only relates the wavenumber spectrum in the convection direction to the frequency spectrum; the wavenumber spectrum normal to the convection direction is undetermined.

Attempts have been made to estimate convection velocities on the Low Cross-Range Orbiter model. When considering only pairs of microphones, rather than arrays in the convection direction, one cannot unequivocally determine the convection velocity. Suppose an almost purely sinusoidal pressure signal of frequency f is passing over sensors A and B, spaced a direction Δx apart in the convection direction. (In Fig. A-5, for example, for microphones #1 and #3, the appropriate distance Δx is the distance 1a − 3). Let the peak of the cross-correlation between A and B be shifted in the direction of A by an amount Δt. The time taken for the pressure field to travel from A to B is then

$$\Delta t' = \Delta t + n/f \ ,$$

where n is an unknown integer. The convection velocity c is then given by

$$c = \frac{\Delta x}{\Delta t'} = \frac{\Delta x}{\Delta t}\left[\frac{F\Delta t}{F\Delta t+n}\right] .$$

Consider, for example, the microphone pair shown in Fig. A-5. The distance Δx is 0.133 ft. For signals filtered in the 8,000 Hz band the correlation peak is delayed by $\Delta t = 70 \times 10^{-6}$ sec and

$$c = 1{,}900\left(\frac{0.56}{0.56 + n}\right) \text{ ft/sec.}$$

At M = 4 the free-stream velocity is about 2,200 ft/sec; the velocity behind a normal shock is 490 ft/sec. Possible values of n and c are

$$n = 0 \ , \quad c = 1{,}900 \text{ ft/sec},$$
$$n = 1 \ , \quad c = \ 680 \text{ ft/sec},$$
$$n = 2 \ , \quad c = \ 420 \text{ ft/sec}.$$

The convection velocity for the highly shocked flow about the model is unlikely to be as high as the free-stream velocity; a value of c = 680 ft/sec is probably much more reasonable.

Signals filtered in the 500-Hz band show correlation peak delays which are small compared to the characteristic frequency of the signal, regardless of the distance between a pair of microphones. This result suggests that the length-scale of the 500-Hz fluctuations is large compared to the model size. Also, the 500-Hz signals are always very strongly cross-correlated — with the largest peak in the cross-correlation coefficient equal to 0.8. This latter result suggests that fluctuations in the 500-Hz band are due to large-scale disturbances propagating through the tunnel list section.

REFERENCES

1. Space Transportation Systems Technology Symposium. Vol. 1 — Aerothermodynamics and Configurations, NASA TM X-52876, 1970, p. 146.

2. Tucker, Maurice: Approximate Calculation of Turbulent Boundary-Layer Development in Compressible Flow. NACA TN 2337, 1951.

3. Klebanoff, P.S.; and Diehl, C.W.: Some Features of Artificially Thickened Fully Developed Turbulent Boundary Layer with Zero-Pressure Gradient. NACA TR 1110, 1952.

4. Corcos, G.M.: Resolution of Pressure in Turbulence. J. Acoust. Soc. Amer., Vol. 35, 1963, pp. 192-199.

5. Chandiramani, K.; Widnall, S.; Lyon, R.H.; and Franken, P.A.: Structural Response to Inflight Acoustic and Aerodynamic Environments. BBN Report No. 1554 (C).

6. Houbolt, John C.: On the Estimation of Pressure Fluctuations in Boundary Layers and Wakes. General Electric Technical Information Series No. 66SD296, Aug. 1966.

7. Lowson, M.V.: Prediction of Boundary Layer Pressure Fluctuations. Technical Report AFFDL-TR-67-167, Apr. 1968.

8. Speaker, W.V.; and Ailman, C.M.: Spectra and Space-Time Correlations of the Fluctuating Pressures at a Wall Beneath a Supersonic Turbulent Boundary Layer Perturbed by Steps and Shock Waves. Douglas Report SM-49806 (NASA Contract No. NASW-932), Nov. 1965.

9. Eldred, Kenneth McK.: Base Pressure Fluctuations. J. Acoust. Soc. Amer., Vol. 33, no. 1, Jan. 1961, pp. 59-63.

10. Robinson, Robert C.; Gambucci, Bruno J.; and George, Robert E.: Fluctuating Pressures on the Afterbodies of Five Blunt Atmosphere Entry Vehicles. NASA TN D-4591, 1968.

11. Widnall, Sheila; and Heller, Hanno H.: Fluctuating Pressure Measurements on a Slender Cone Model in a Mach 3 Flow. BBN Tech. Memo. No. 1, Job No. 151194, 1968.

12. Cassanto, J.M.; and Rasmussen, N.S.: Correlation of Measured Free Flight Base Pressure Data for M = 4 to M = 19 in Laminar and Turbulent Flow. General Electric Technical Information Series No. 68SD256, Apr. 1968.

a. Low Cross-Range Orbiter

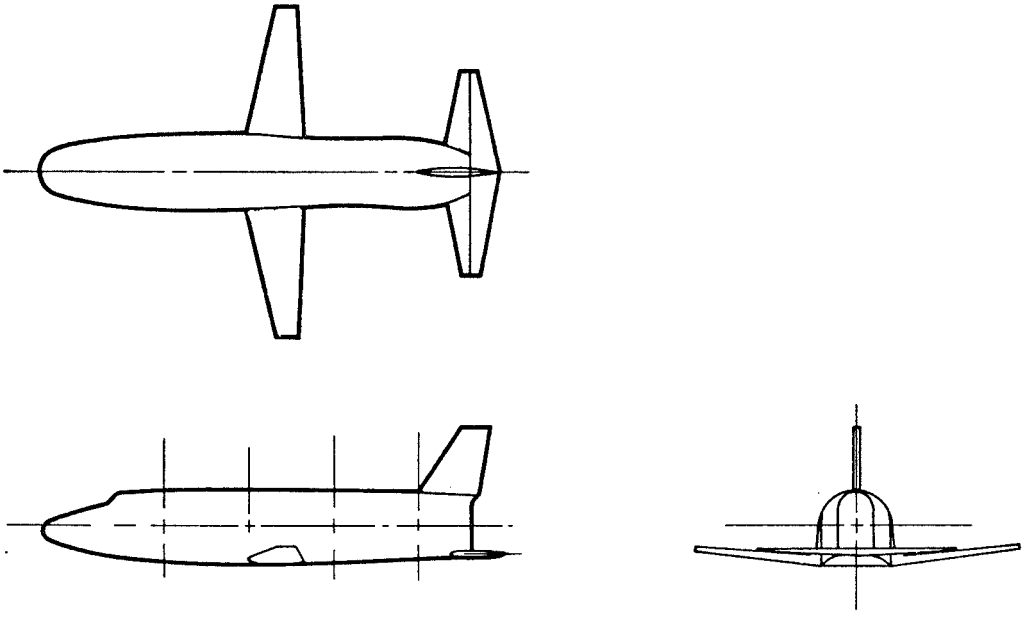

b. High Cross-Range Orbiter

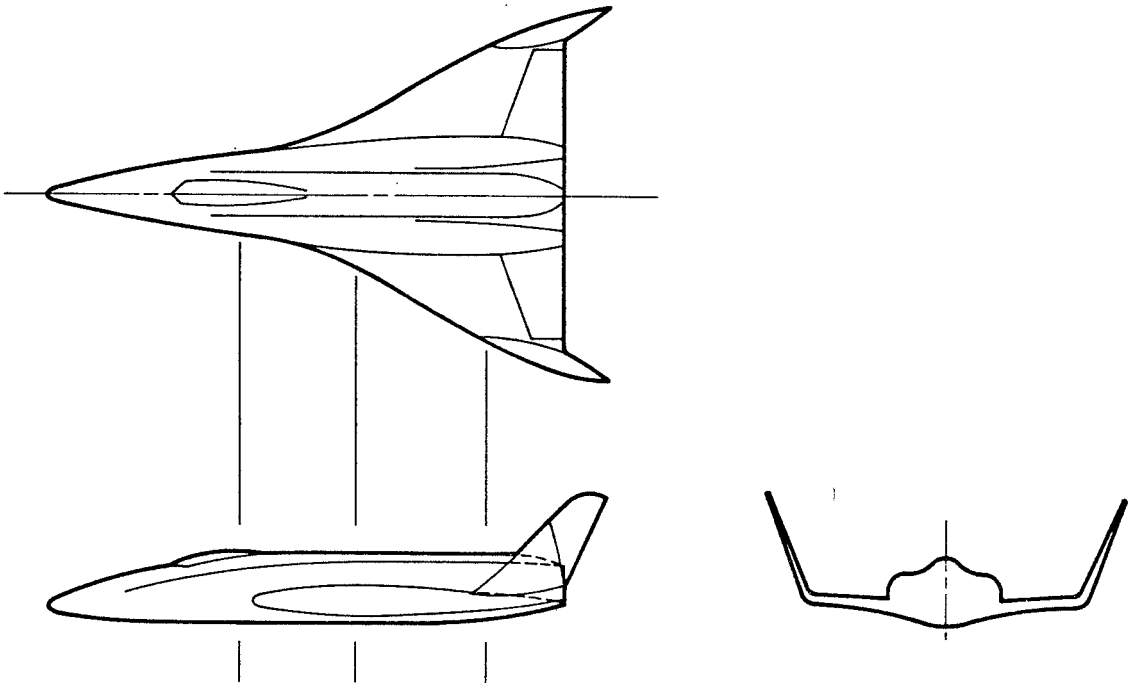

FIG. 1 ORBITER CONFIGURATIONS

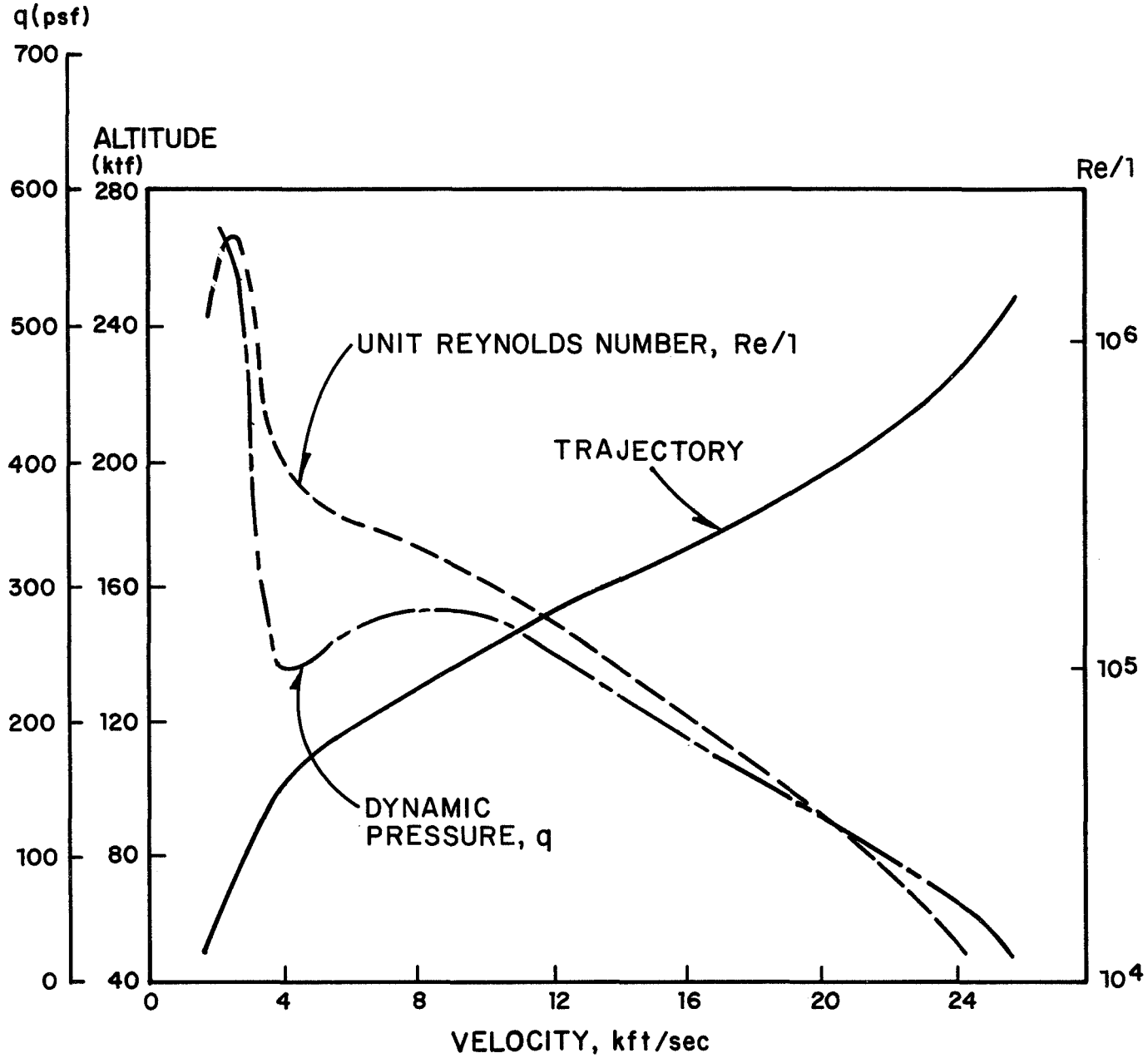

FIG. 2 REENTRY FLIGHT PARAMETERS

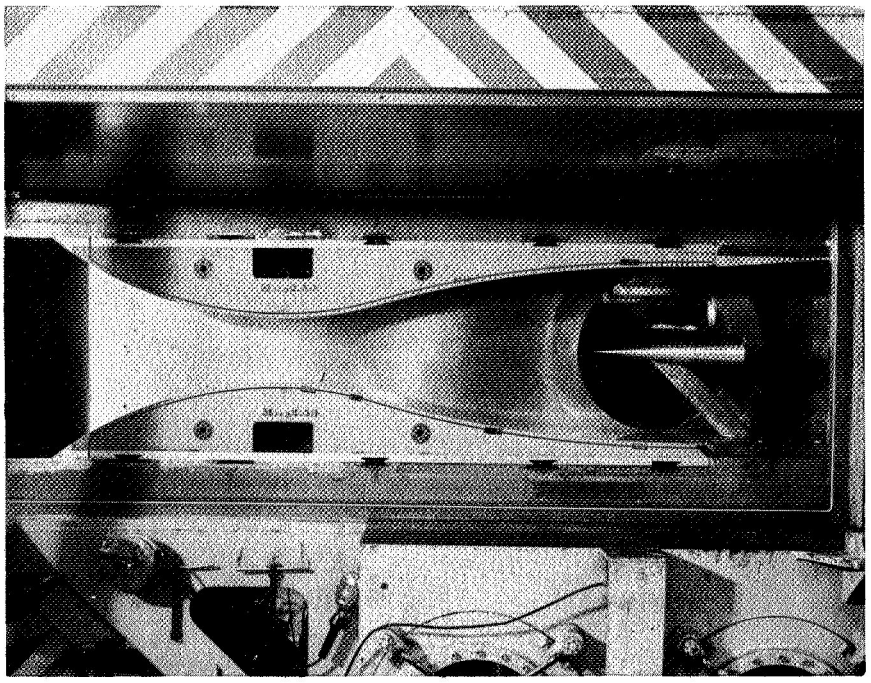

Model Installation in M.I.T. Tunnel
M = 2.5 Nozzle Blocks

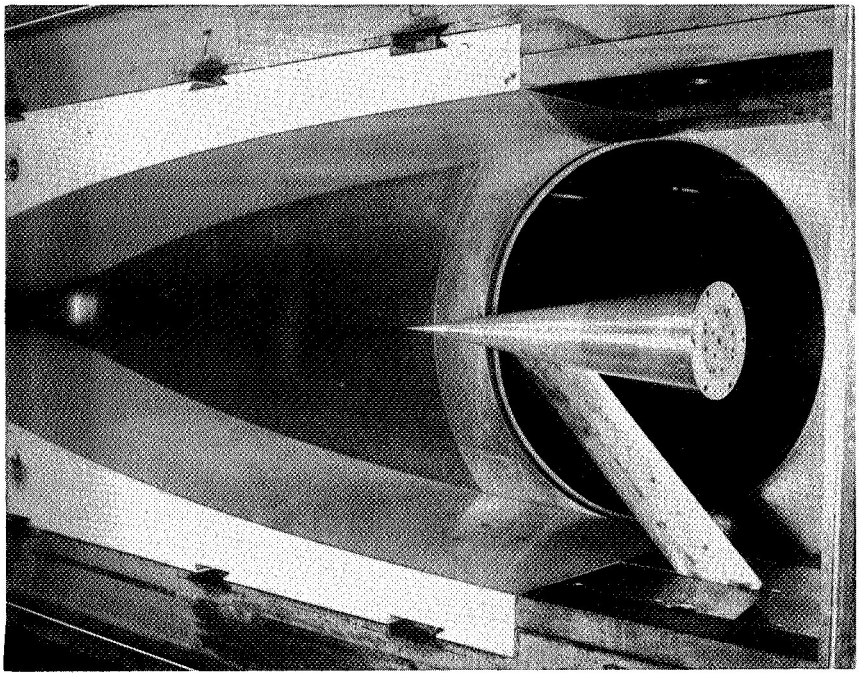

Close-up of Installation

FIG. 3 SLENDER-CONE/FLAT-BASE CONFIGURATION

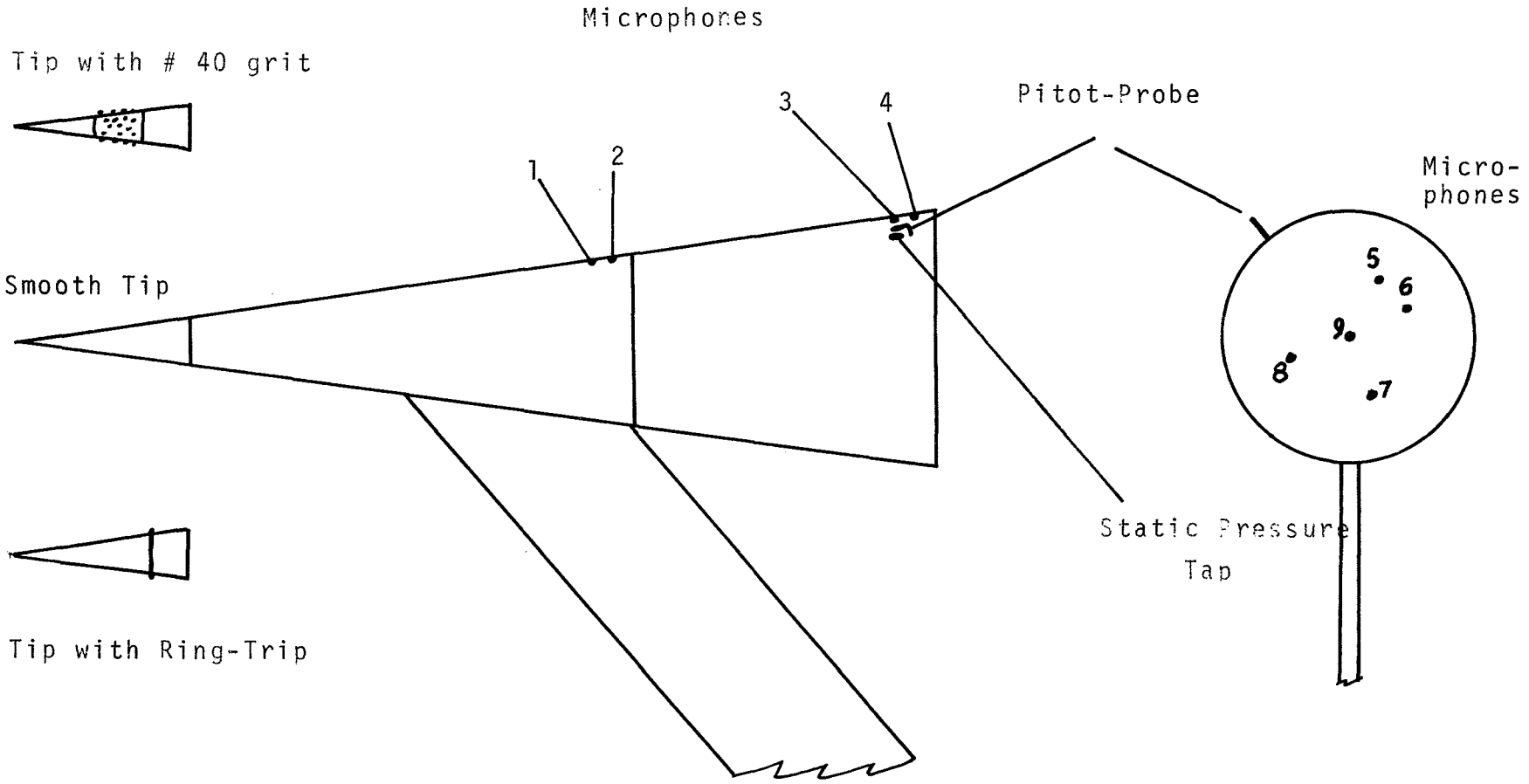

FIG. 4 LOCATION OF MICROPHONES, STATIC PRESSURE TAP, AND PITOT PROBE

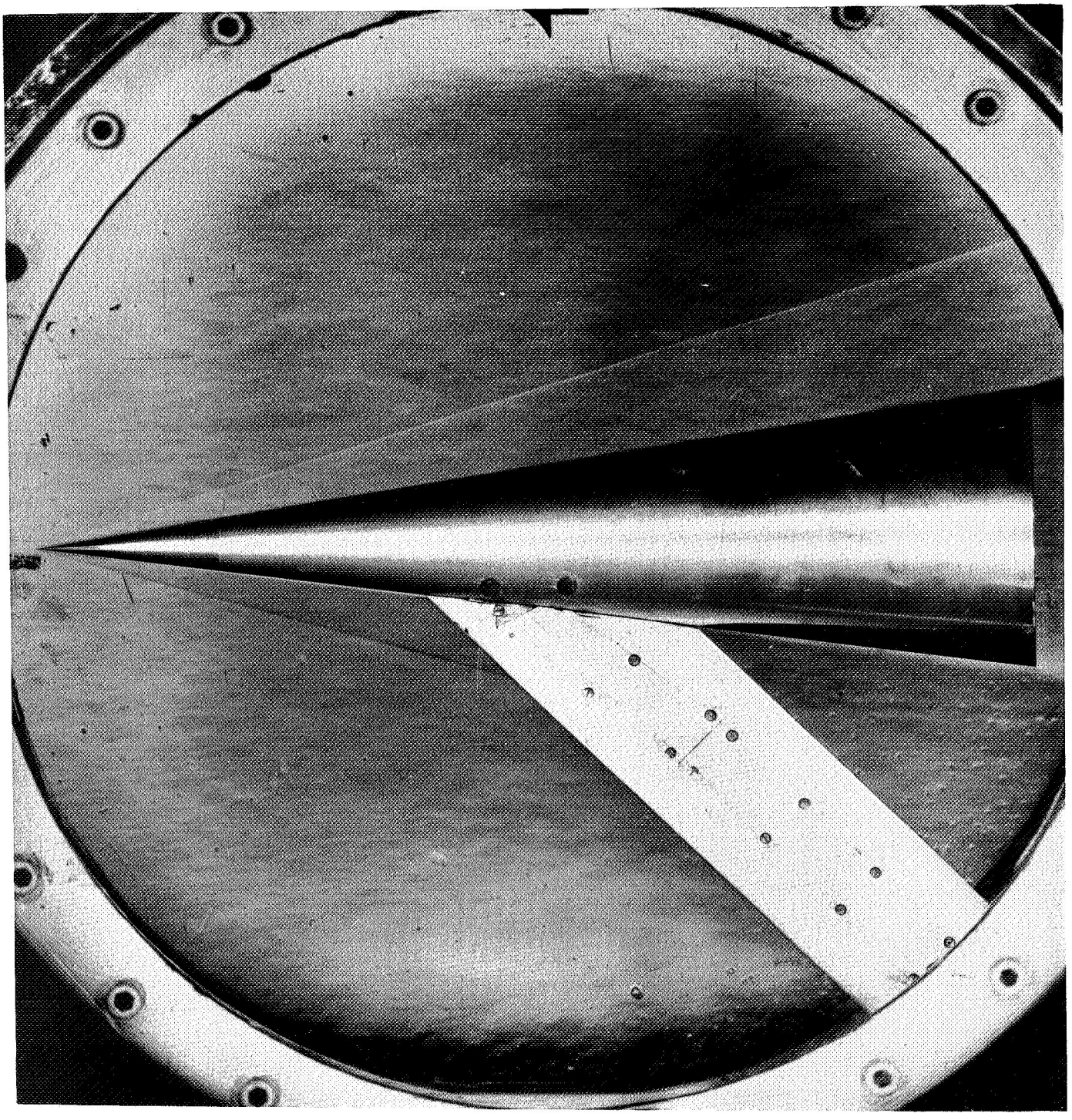

FIG. 5 SCHLIEREN PHOTOGRAPH — α = 0°; M = 4; P_0 = 20 psi; NO TRIP

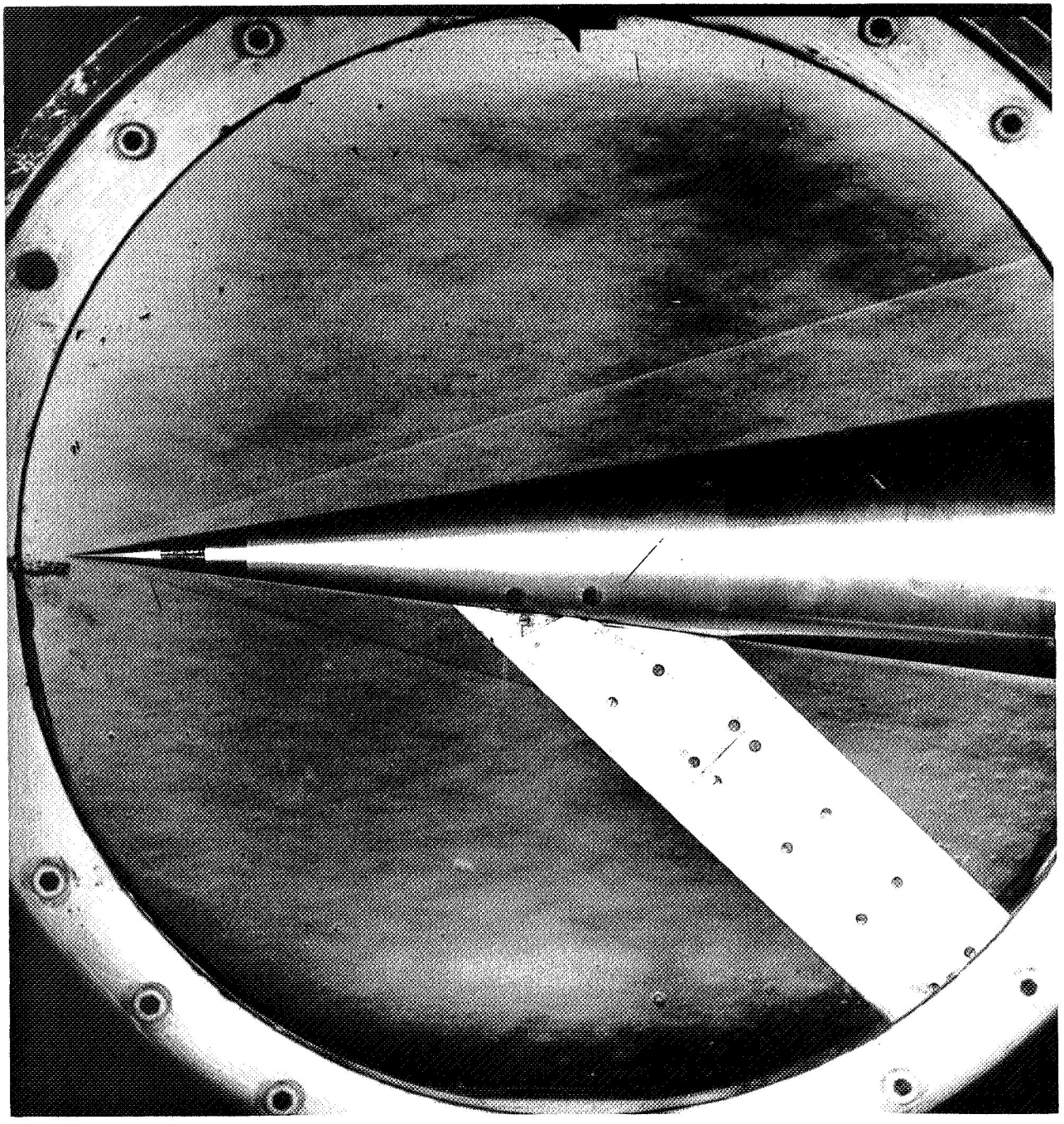

FIG. 6 SCHLIEREN PHOTOGRAPH — α = 0°; M = 4; P_0 = 20 psi; GRIT TRIP

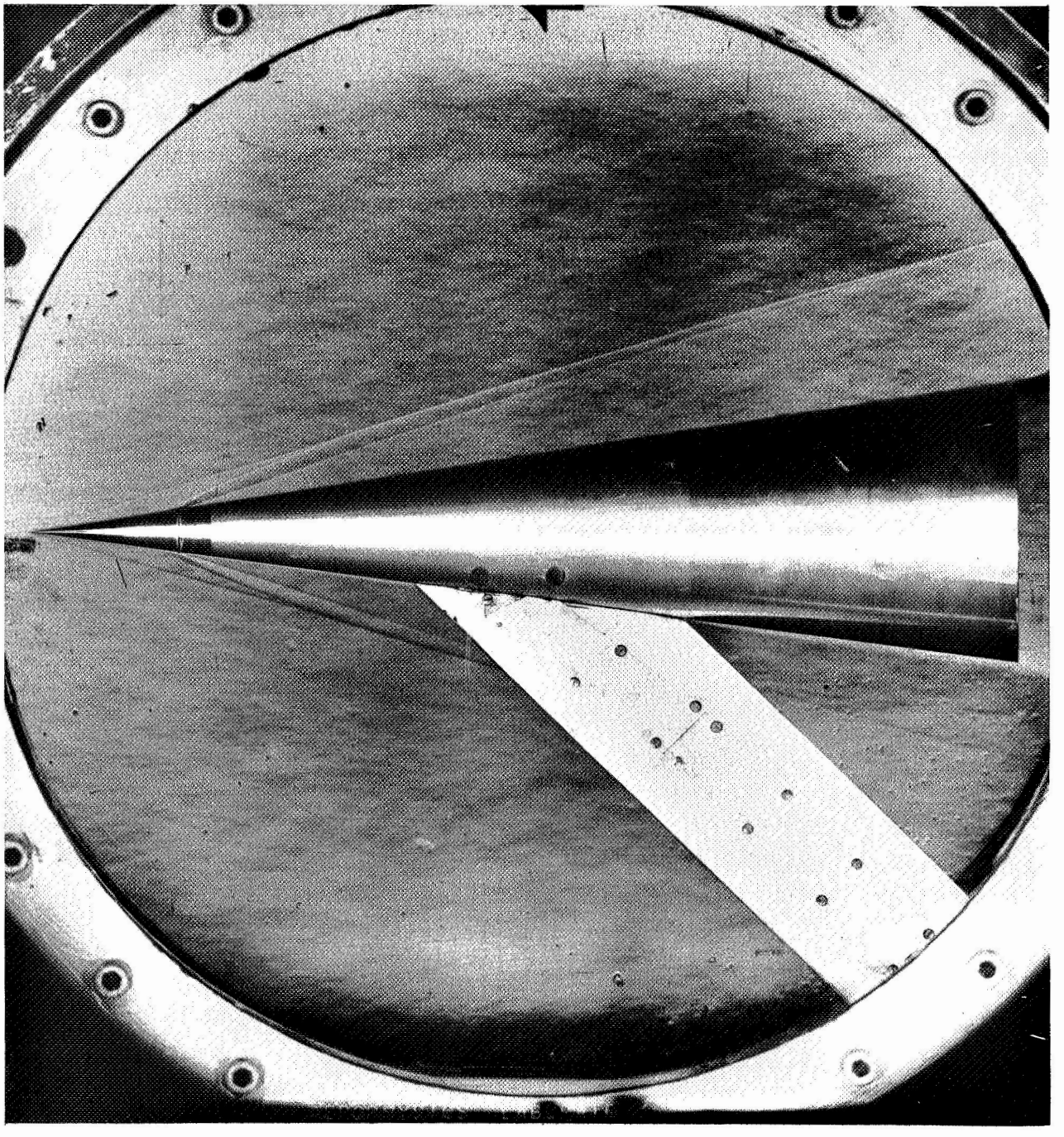

FIG. 7 SCHLIEREN PHOTOGRAPH — α = 0°; M = 4; P_0 = 30 psi; RING TRIP

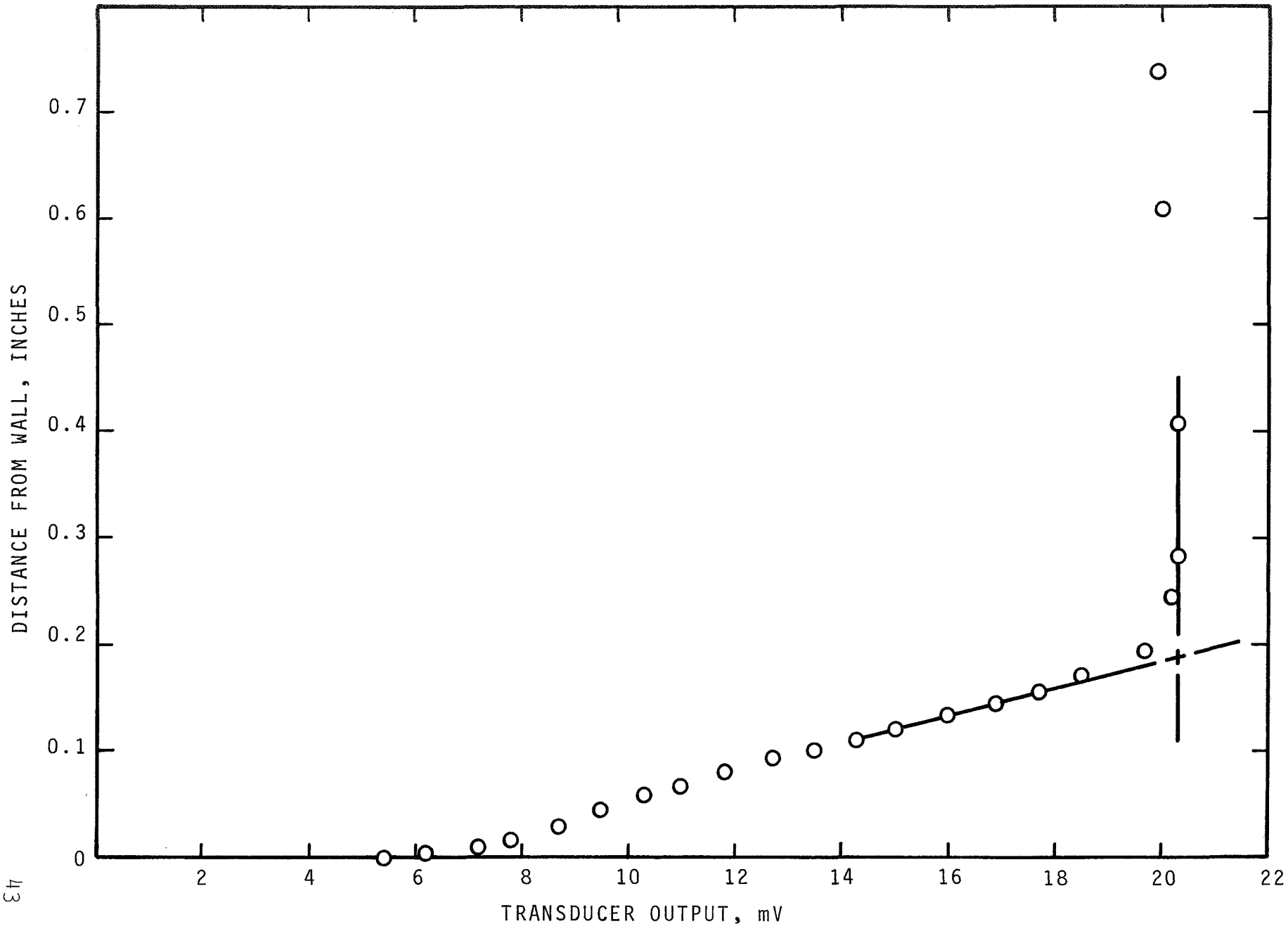

FIG. 8 PITOT PRESSURE PROFILE, M = 4

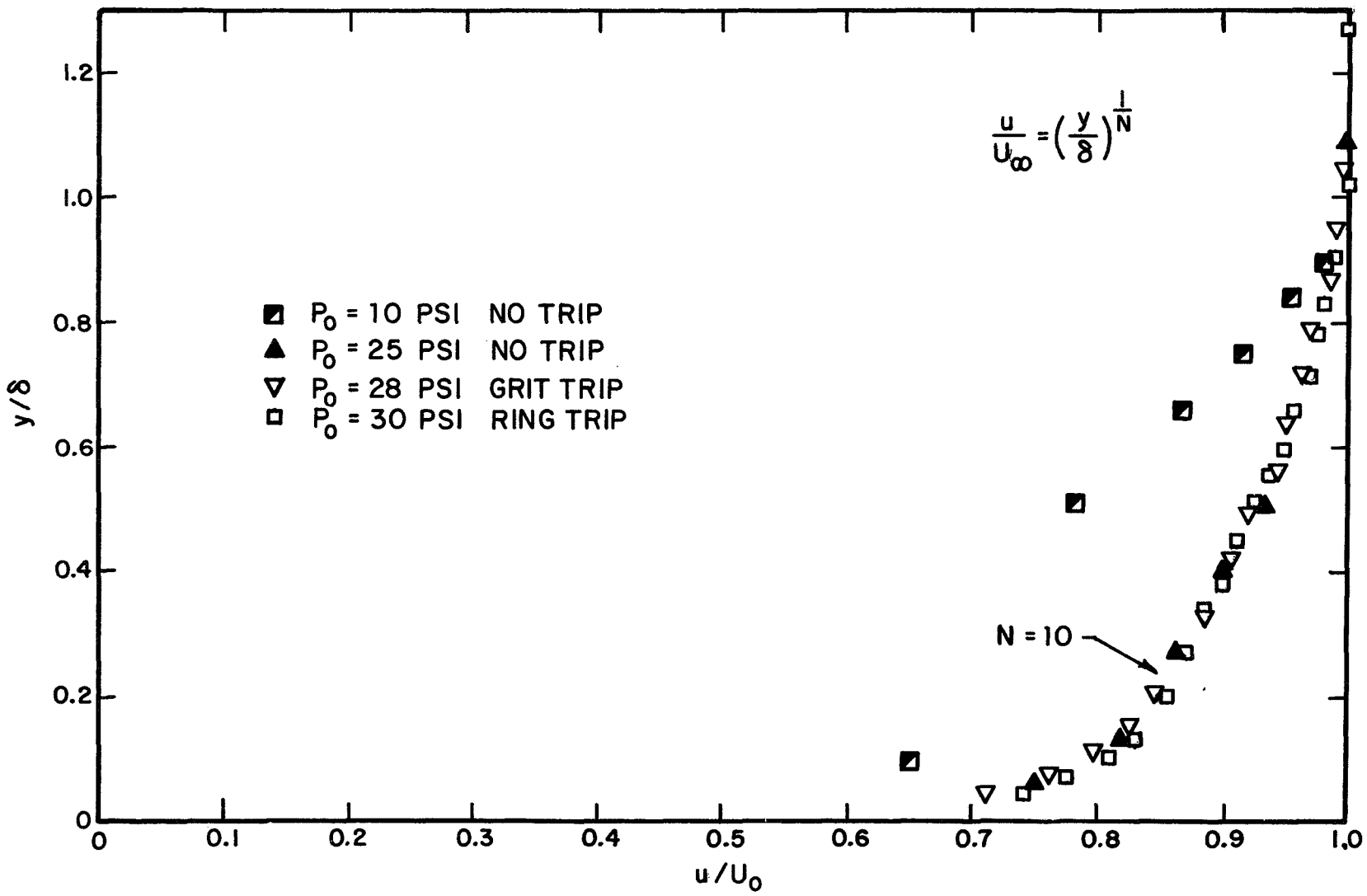

FIG. 9 NORMALIZED BOUNDARY-LAYER PROFILE; M = 4

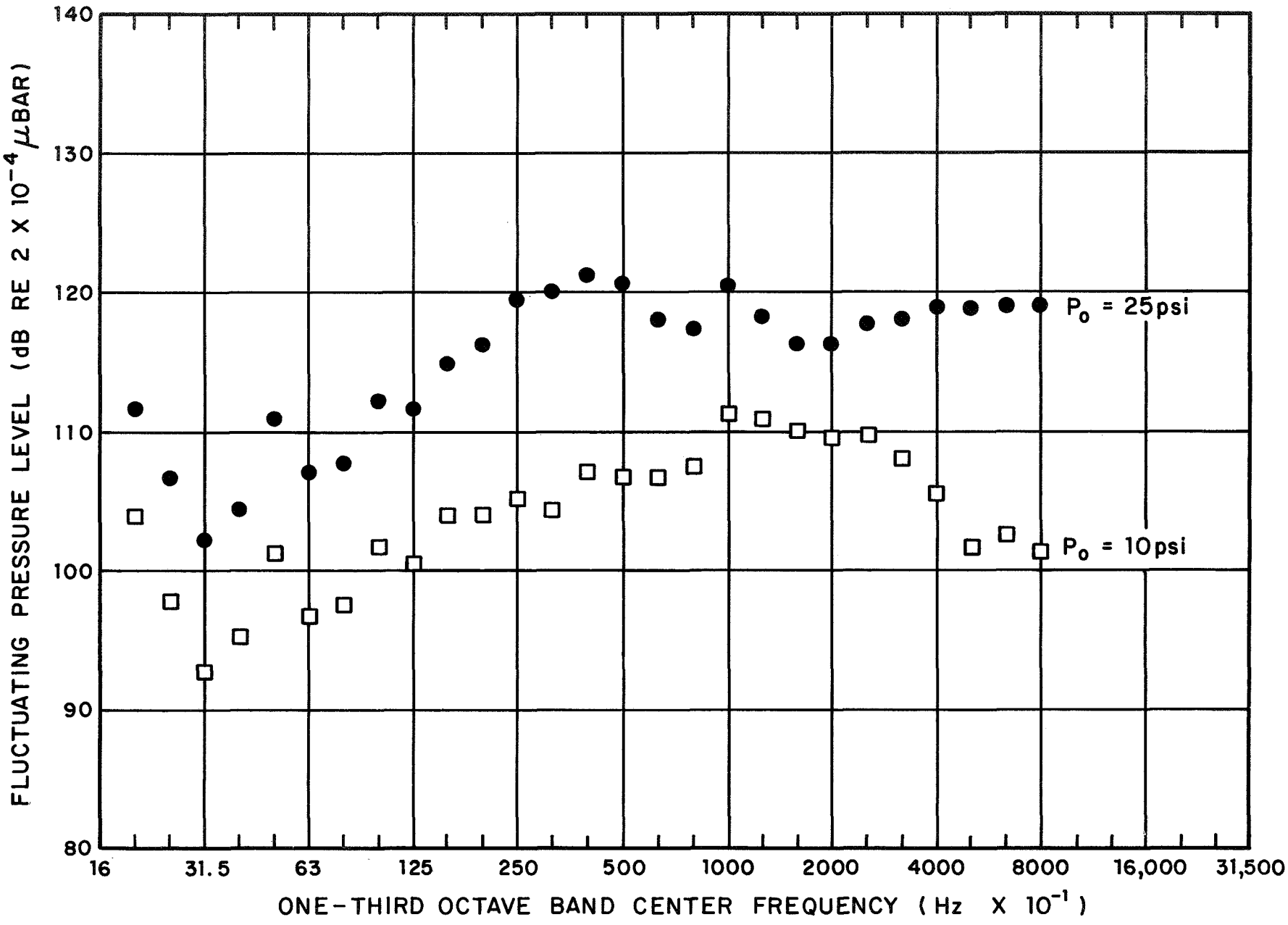

FIG. 10 ONE-THIRD OCTAVE BAND SPECTRA; MICROPHONE #4; $\alpha = 0°$; $M = 4$

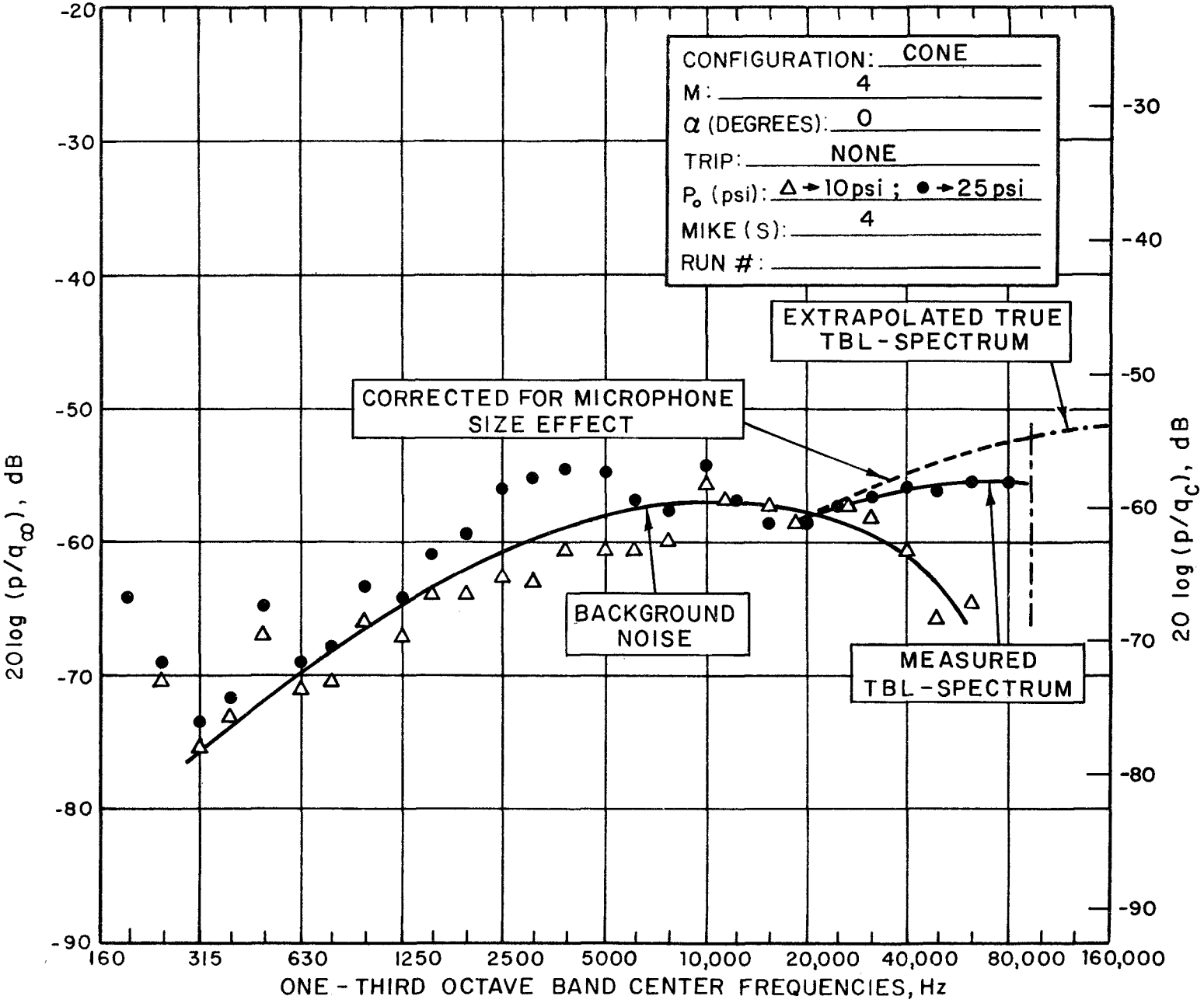

FIG. 11 NORMALIZED ONE-THIRD OCTAVE BAND SPECTRA; MICROPHONE #4, $\alpha = 0°$; $M = 4$

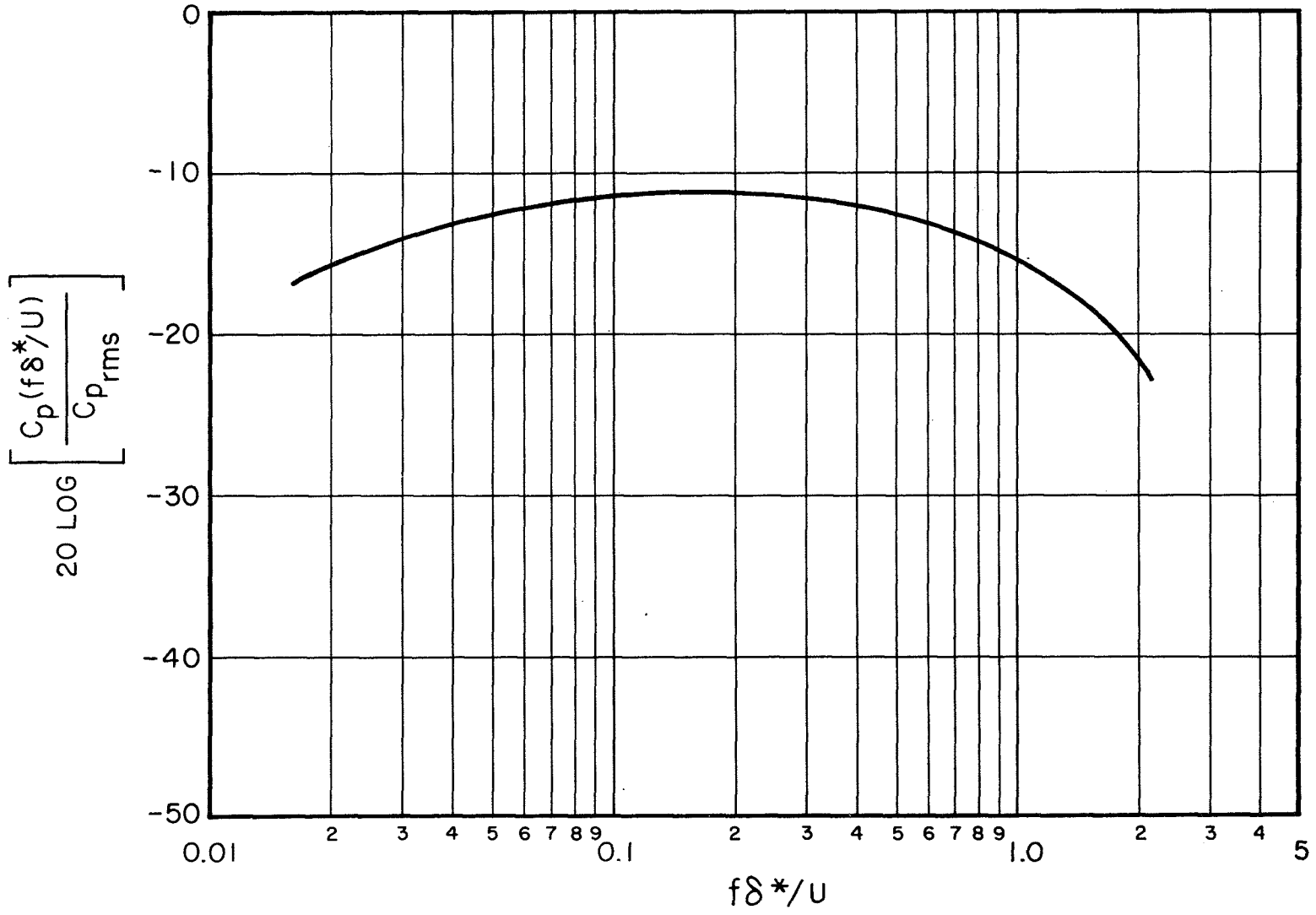

FIG. 12 NONDIMENSIONAL SPECTRUM OF BOUNDARY-LAYER PRESSURE FLUCTUATIONS IN ONE-THIRD OCTAVE BANDS

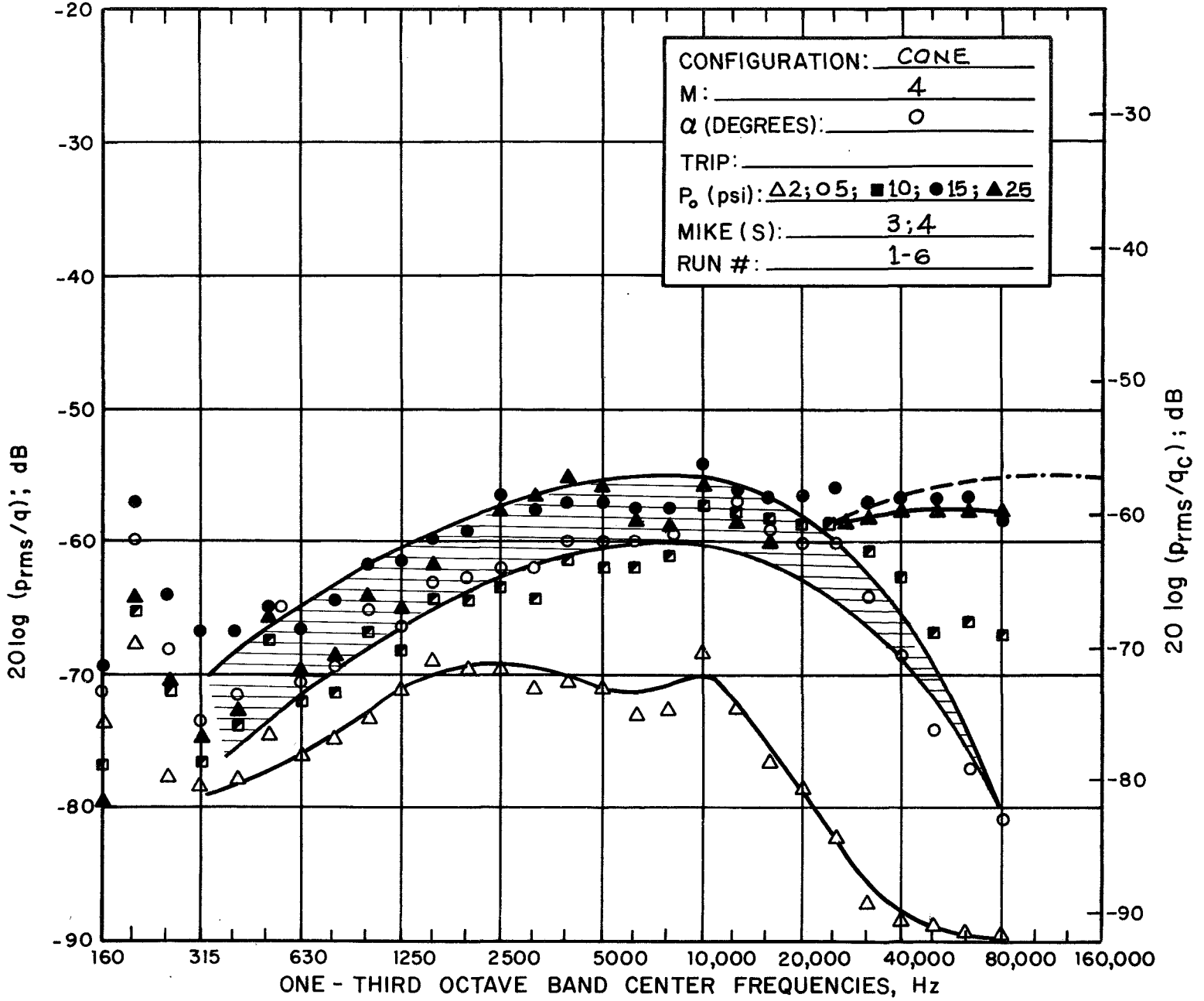

FIG. 13 NORMALIZED ONE-THIRD OCTAVE BAND SPECTRA FOR NATURAL BOUNDARY-LAYER DEVELOPMENT; MICROPHONES #3 AND #4; M = 4

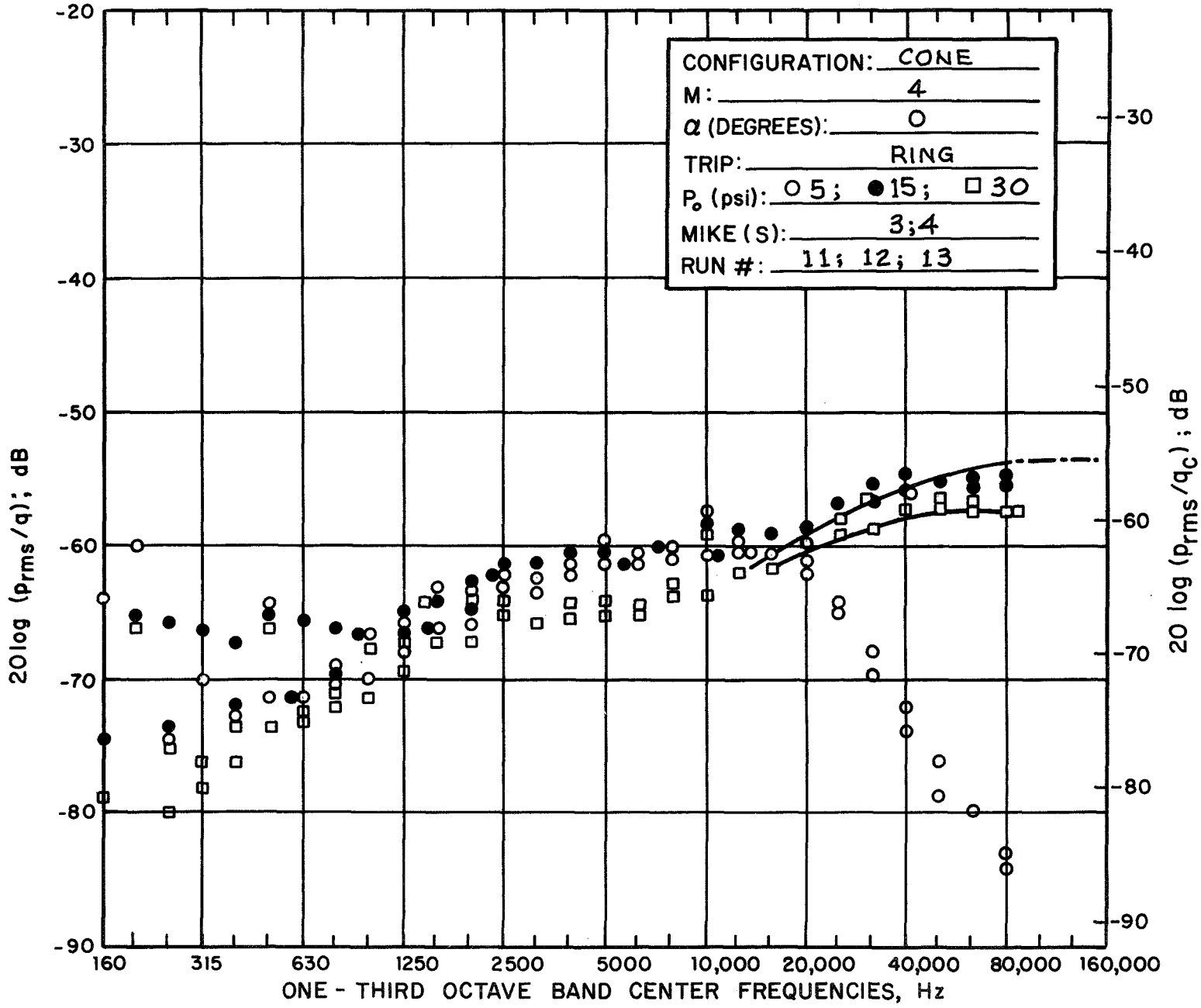

FIG. 14 NORMALIZED ONE-THIRD OCTAVE BAND SPECTRA FOR TRIPPED BOUNDARY LAYER; MICROPHONES #3 AND #4, M = 4

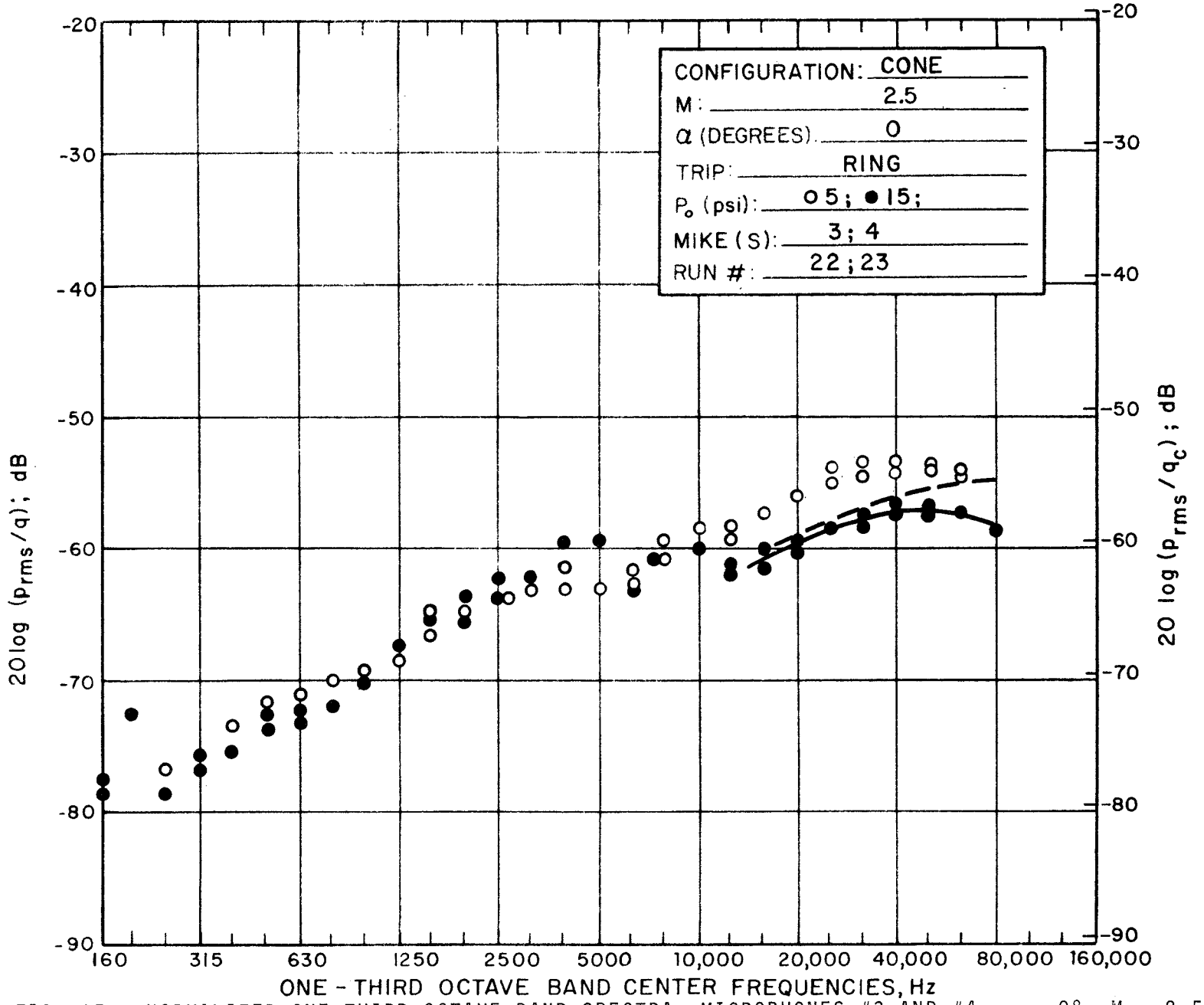

FIG. 15 NORMALIZED ONE-THIRD OCTAVE BAND SPECTRA; MICROPHONES #3 AND #4; $\alpha = 0°$; $M = 2.5$

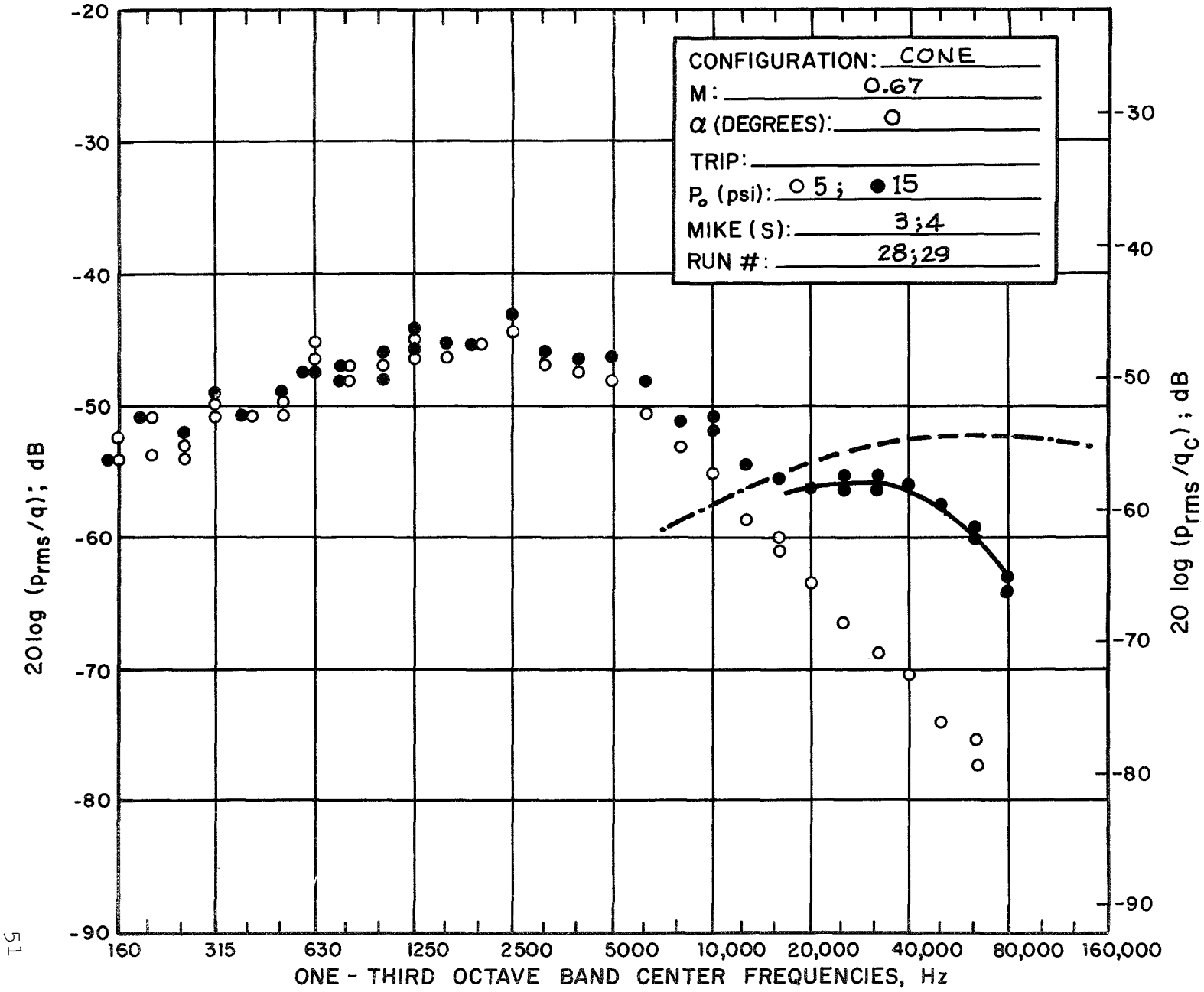

FIG. 16 NORMALIZED ONE-THIRD OCTAVE BAND SPECTRA FOR NATURAL BOUNDARY LAYER DEVELOPMENT; MICROPHONES #3 AND #4; M = 0.67

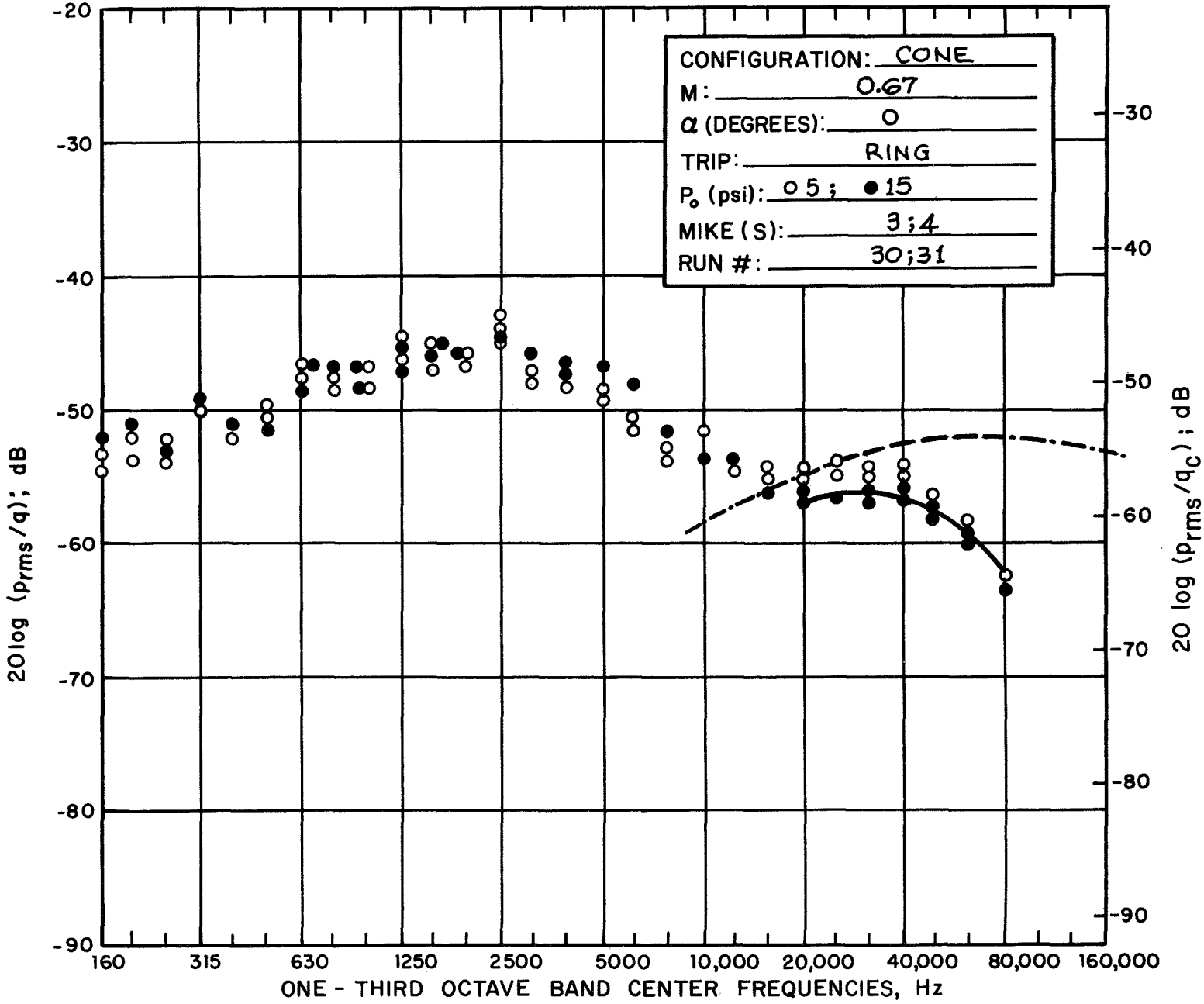

FIG. 17 NORMALIZED ONE-THIRD OCTAVE BAND SPECTRA FOR TRIPPED BOUNDARY LAYER; MICROPHONES #3 AND #4; M = 0.67

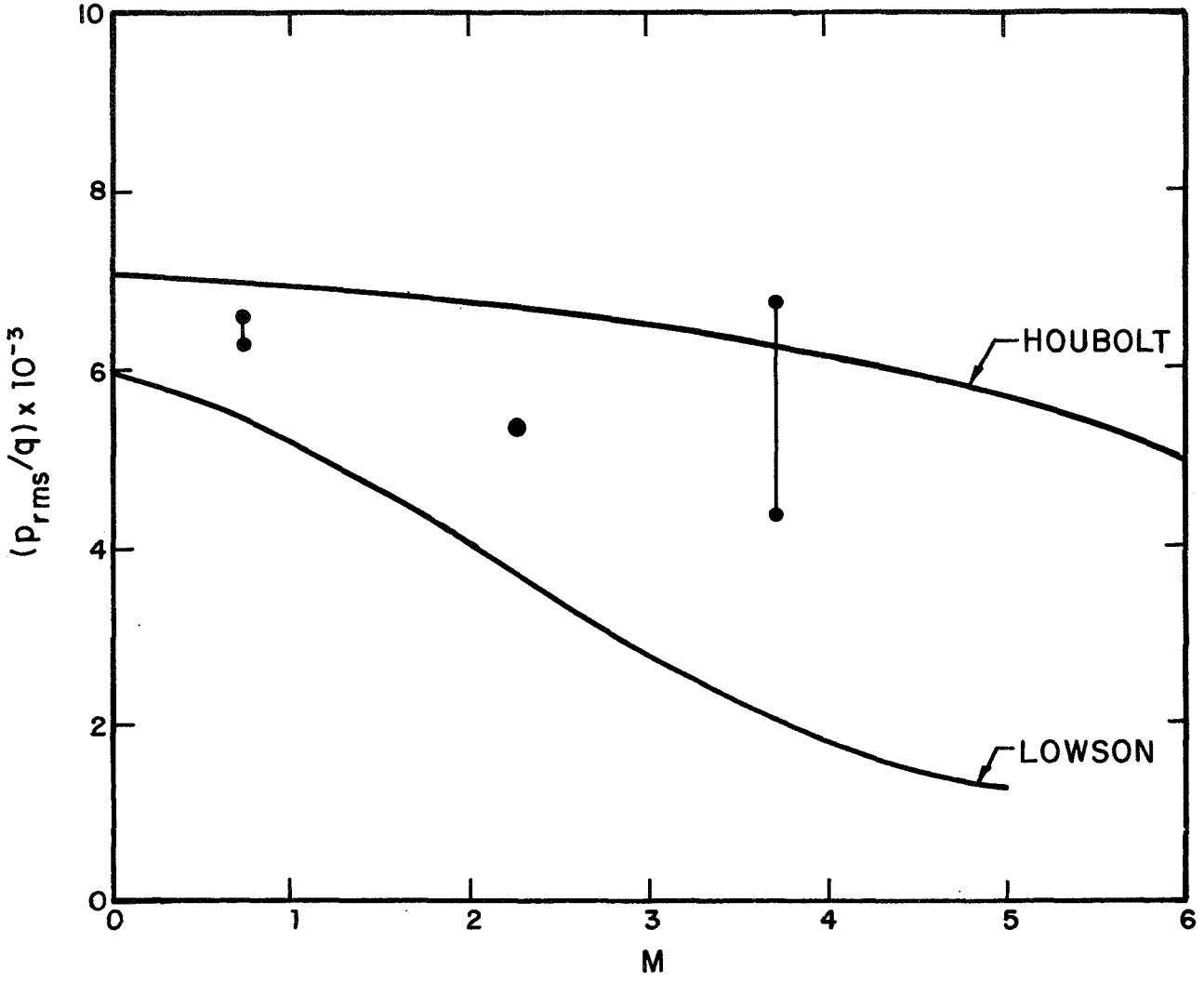

FIG. 18 OVERALL FLUCTUATING PRESSURE LEVEL AS FUNCTION OF MACH NUMBER; ATTACHED TURBULENT BOUNDARY LAYER

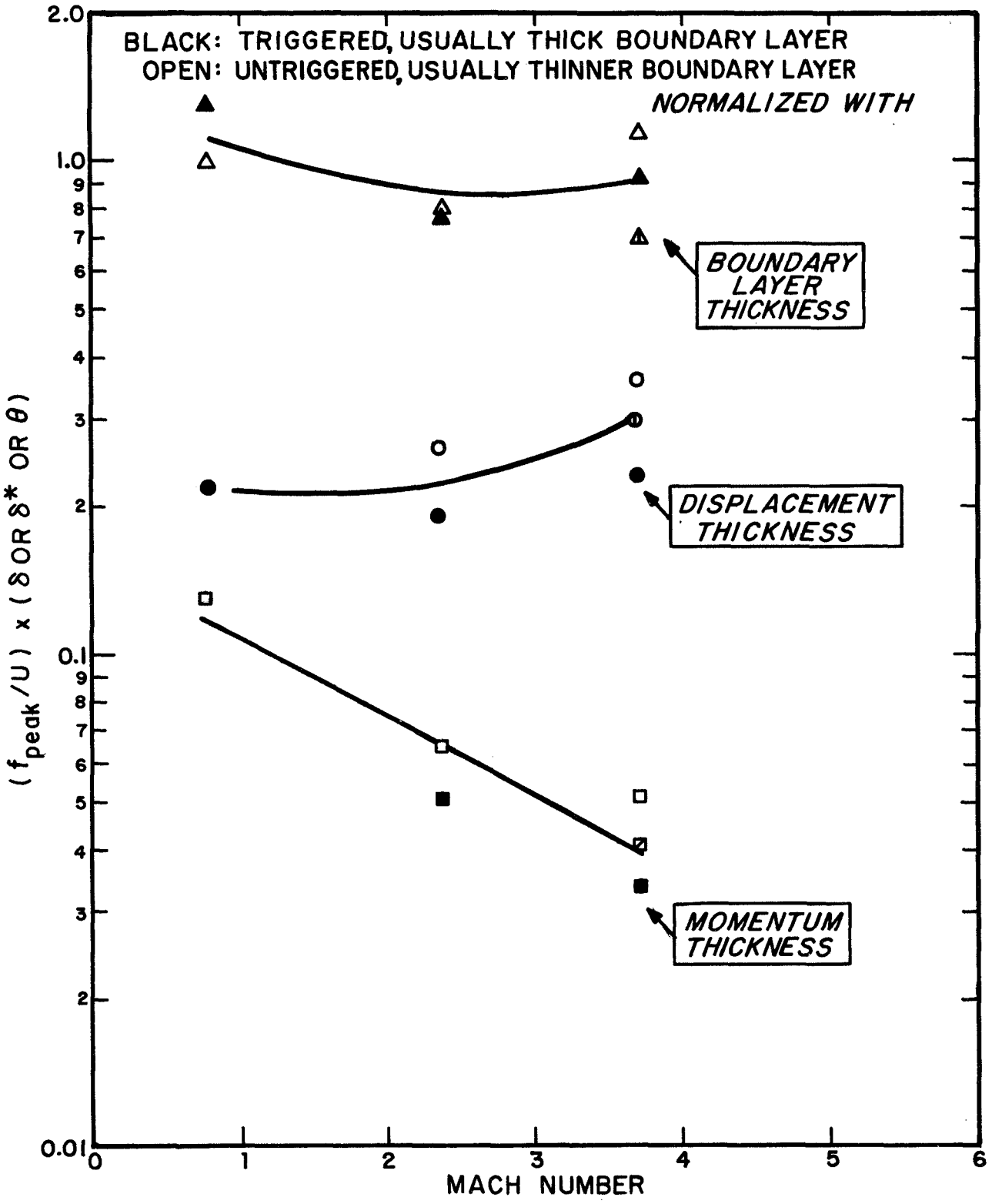

FIG. 19 NORMALIZED PEAK FREQUENCY AS FUNCTION OF MACH NUMBER; ATTACHED TURBULENT BOUNDARY LAYER

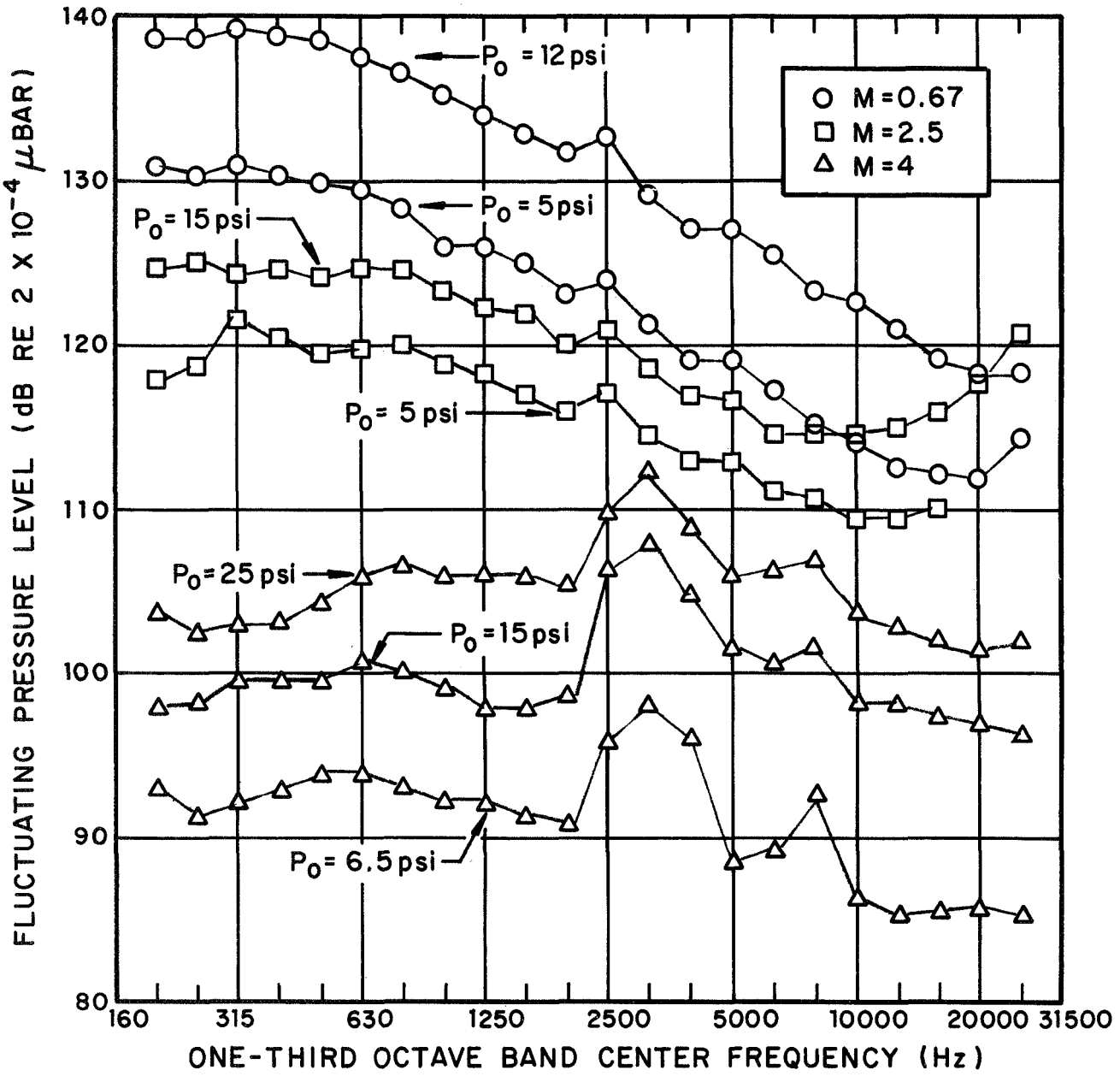

FIG. 20 ONE-THIRD OCTAVE BAND SPECTRA; MICROPHONE #9; α = 0°; M = 4

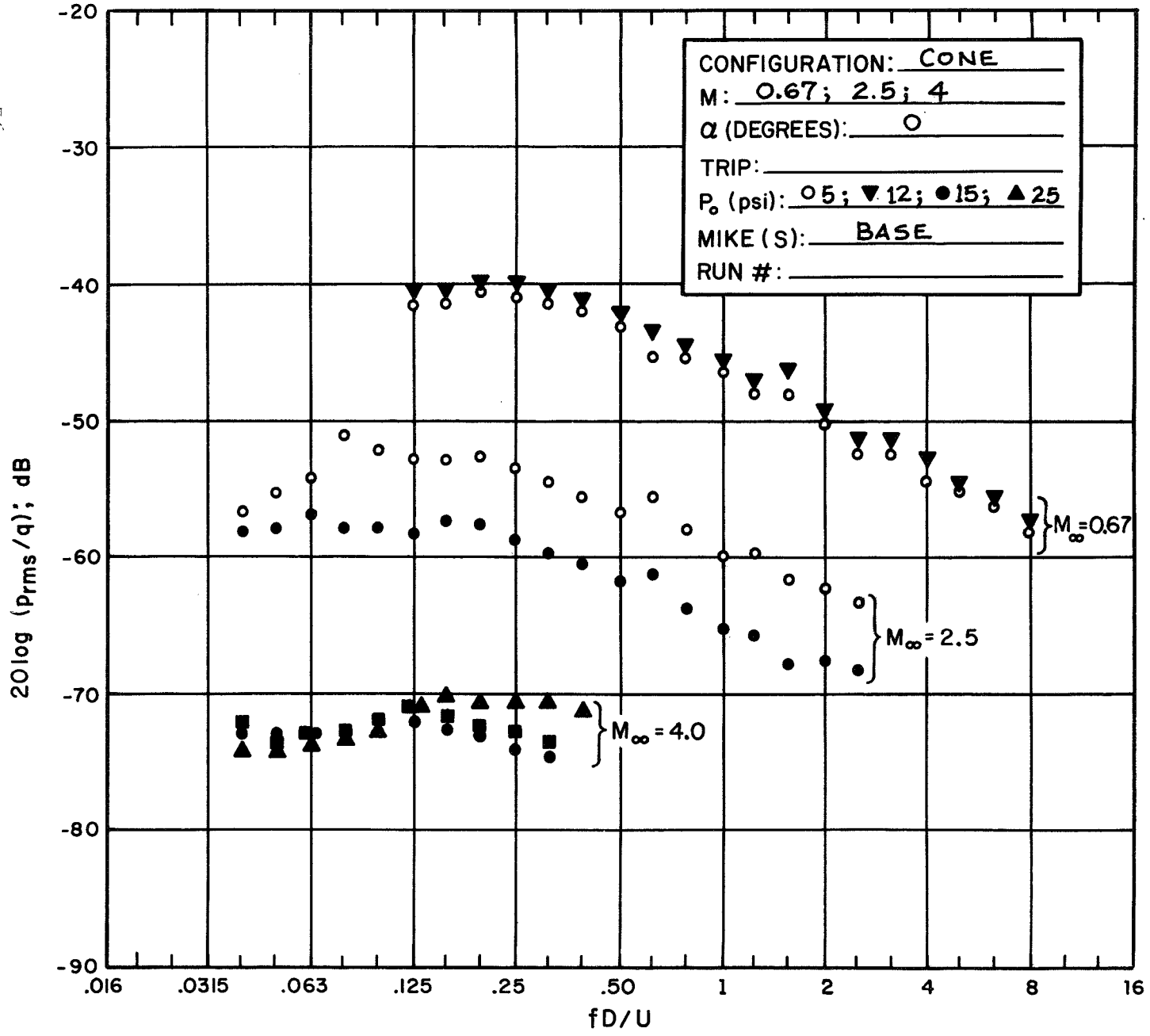

FIG. 21 NORMALIZED BASE PRESSURE SPECTRA FOR VARIOUS MACH NUMBERS

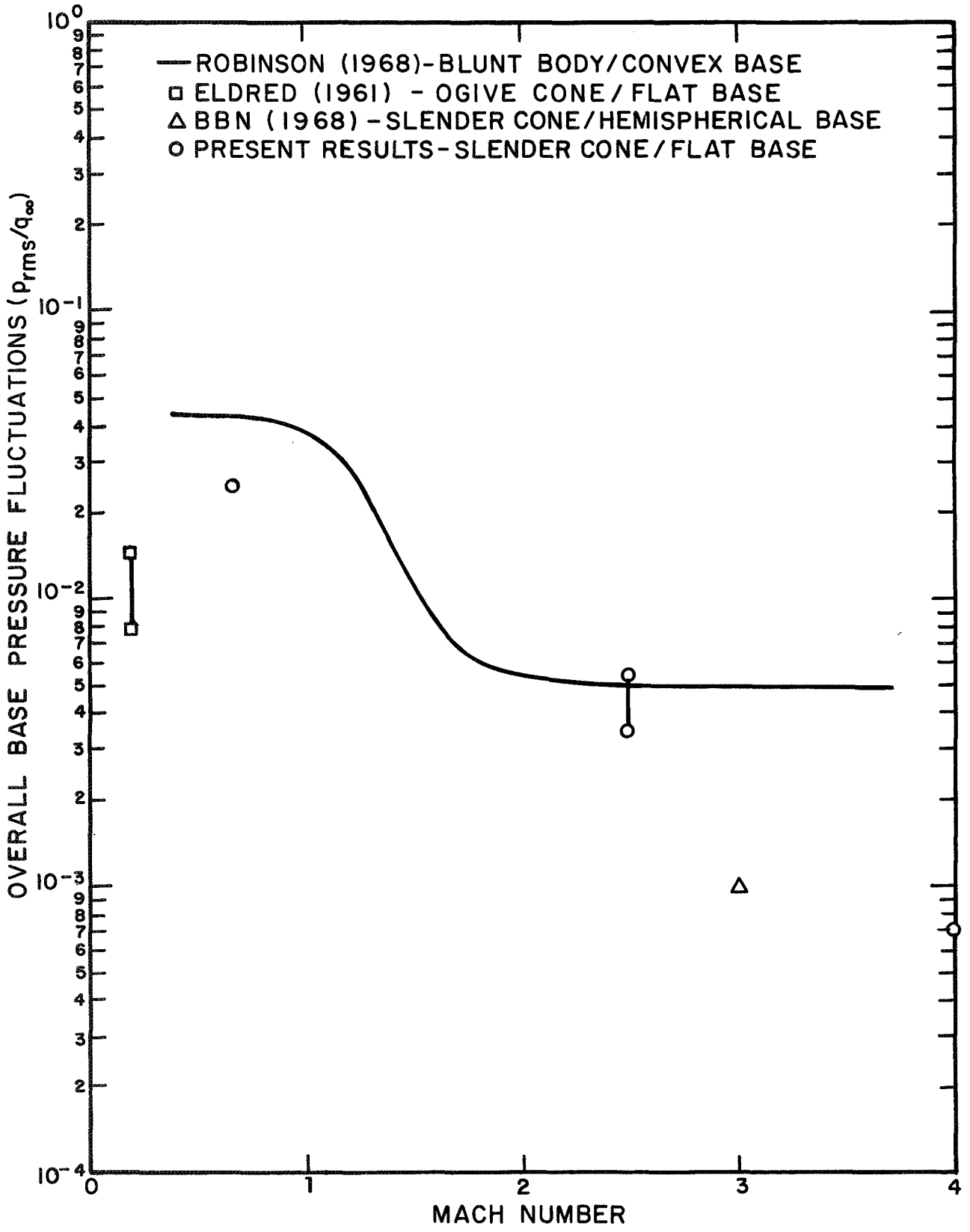

FIG. 22 OVERALL BASE PRESSURE LEVELS AS FUNCTION OF MACH NUMBER

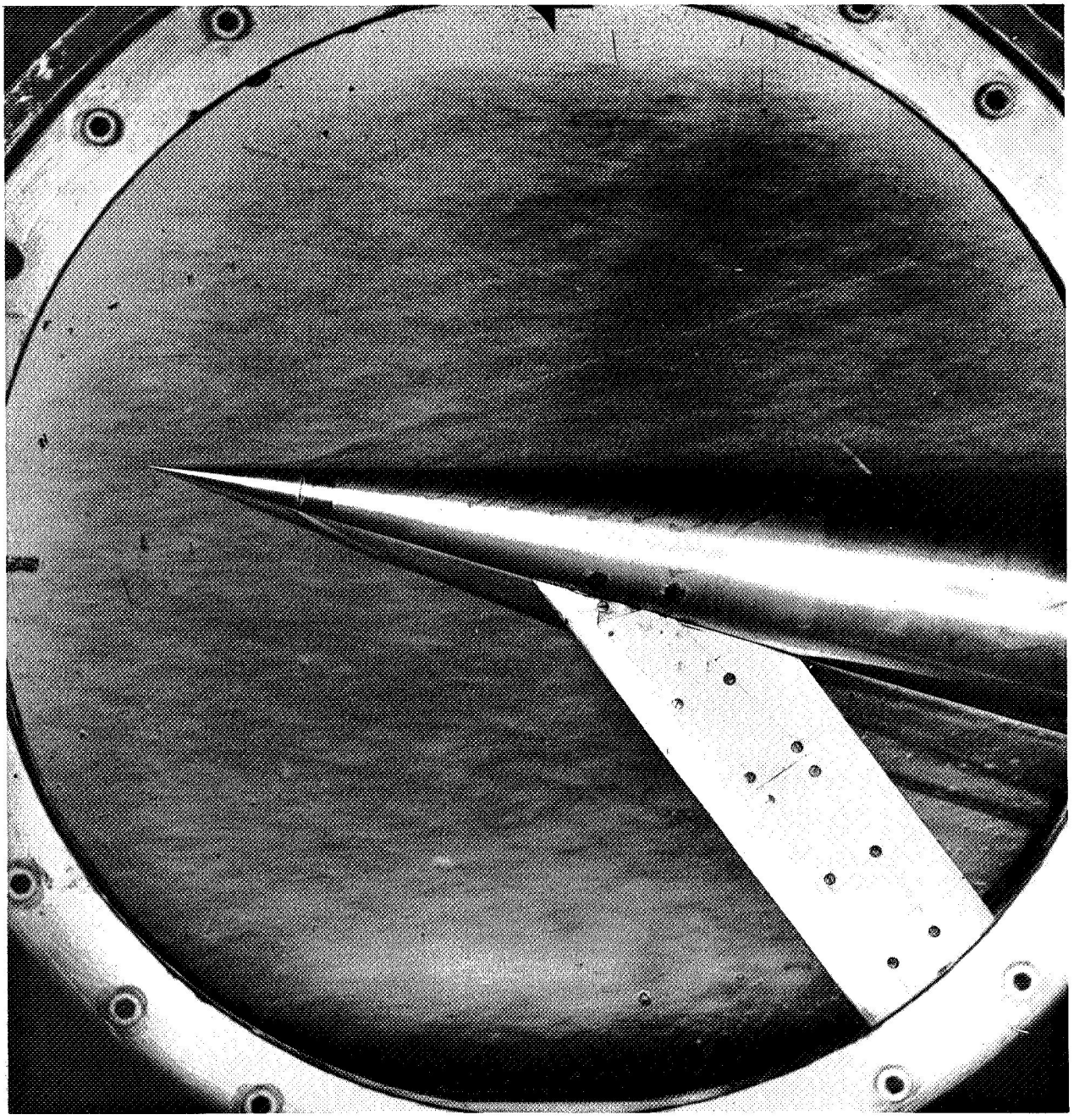

FIG. 23 CONE MODEL AT ANGLE OF ATTACK; α = 10°; M = 4, P_0 = 30 psi; RING TRIP

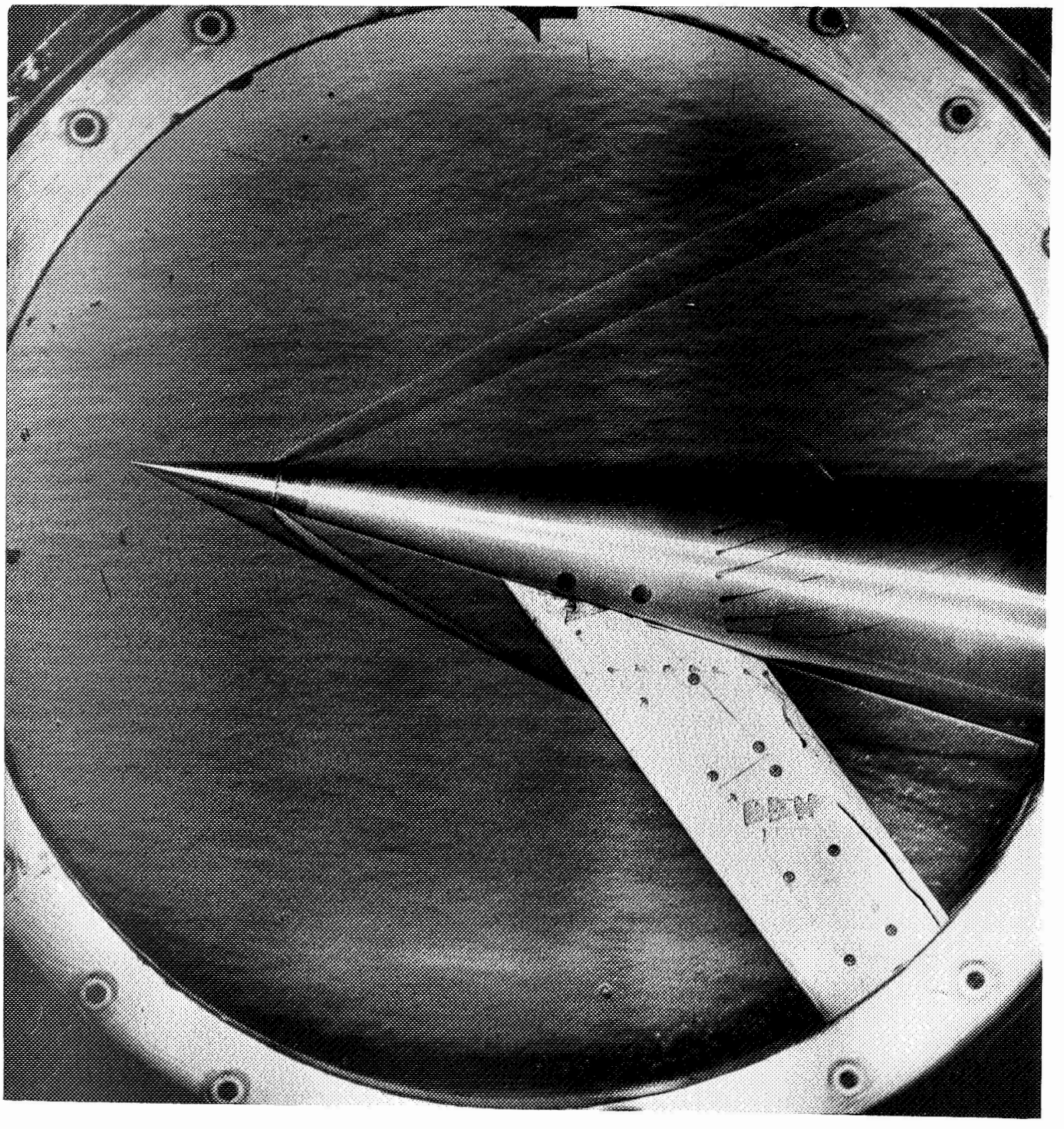

FIG. 24 CONE MODEL AT ANGLE OF ATTACK; α = 10°; M = 2.5; P_0 = 15 psi; RING TRIP

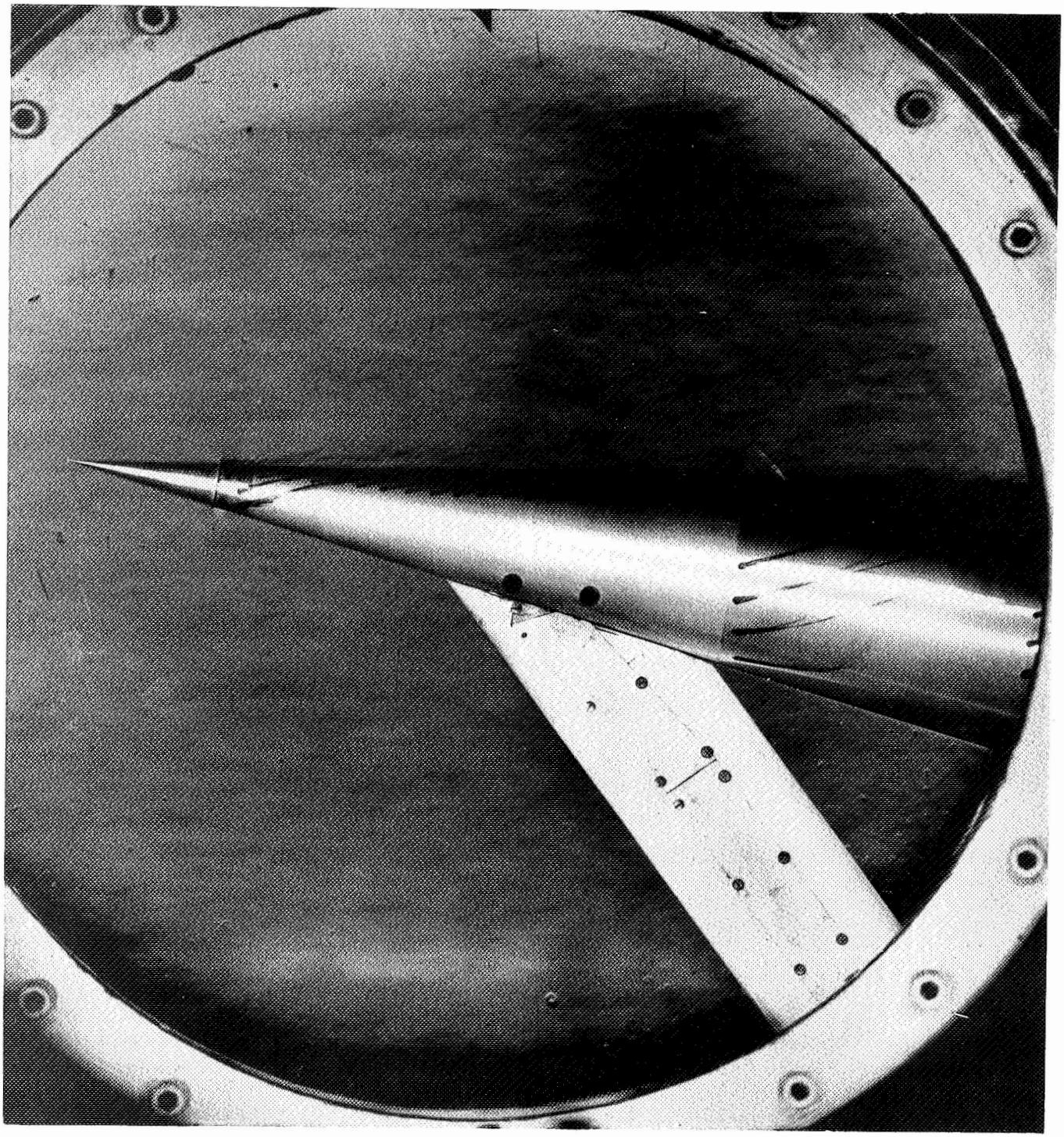

FIG. 25 CONE MODEL AT ANGLE OF ATTACK; α = 10°; M = 0.66; P_0 = 12 psi; RING TRIP

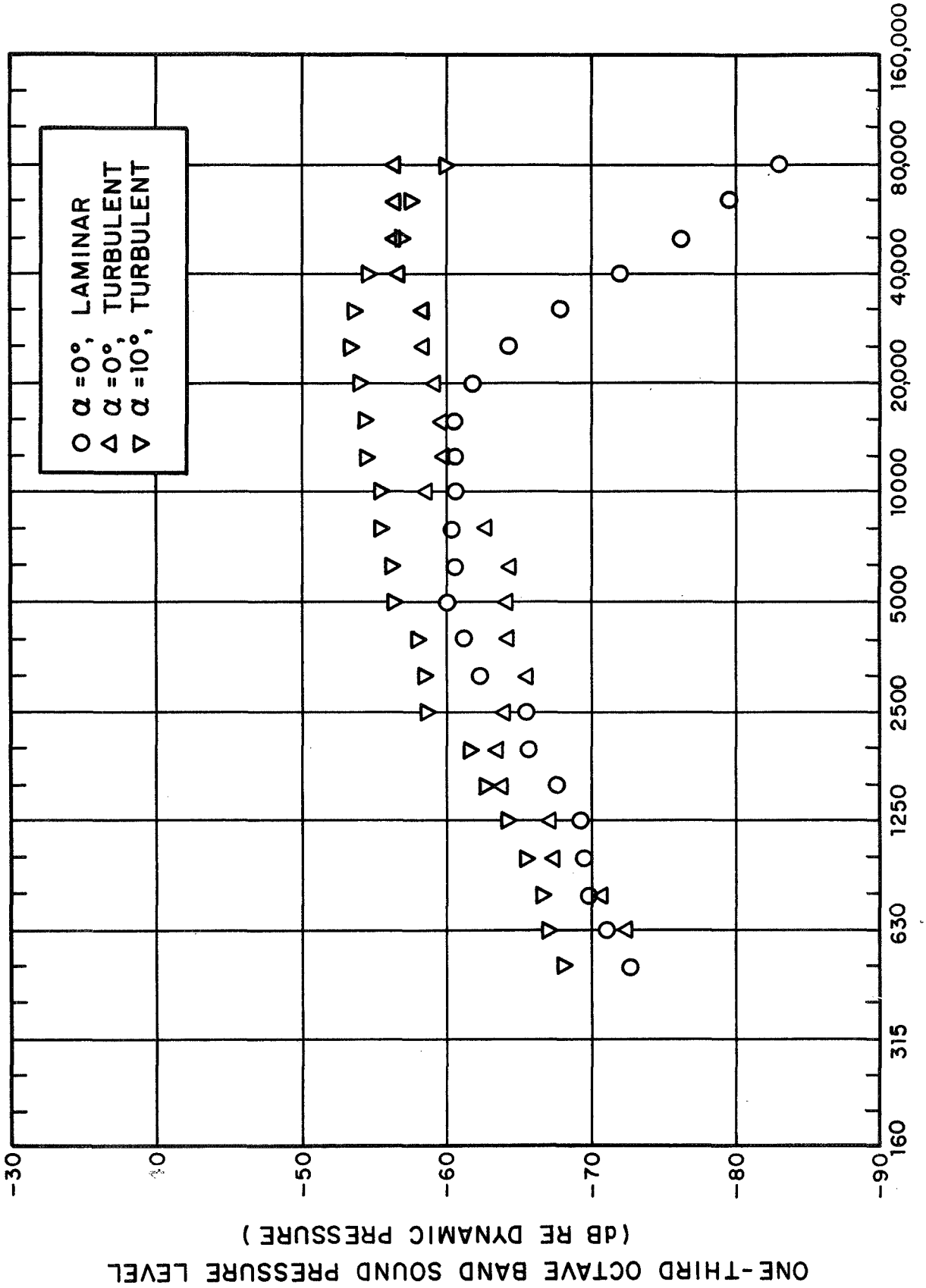

FIG. 26 CONE MODEL AT ANGLE OF ATTACK; SURFACE MICROPHONE; M = 4

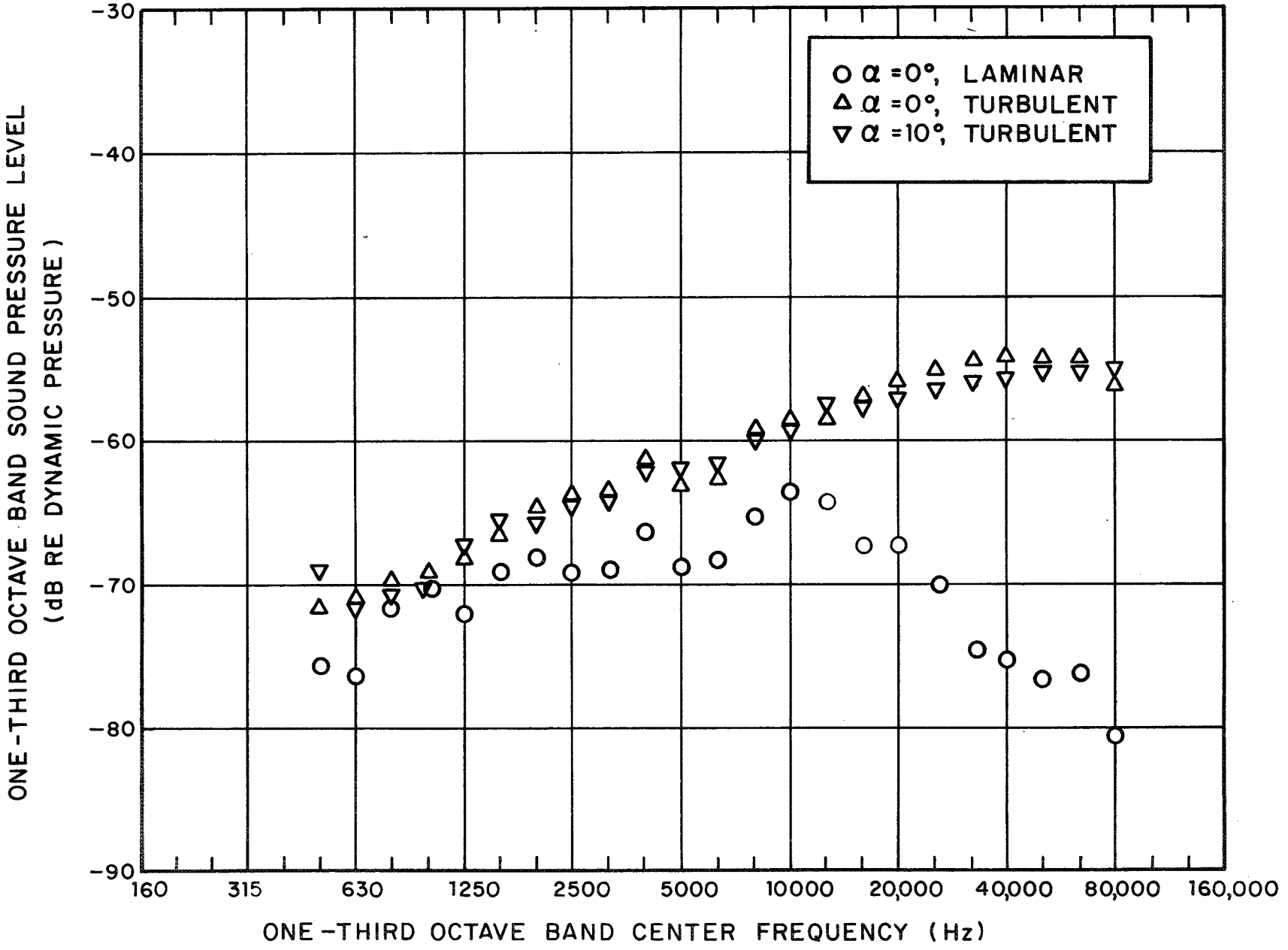

FIG. 27 CONE MODEL AT ANGLE OF ATTACK; SURFACE MICROPHONE; M = 2.5

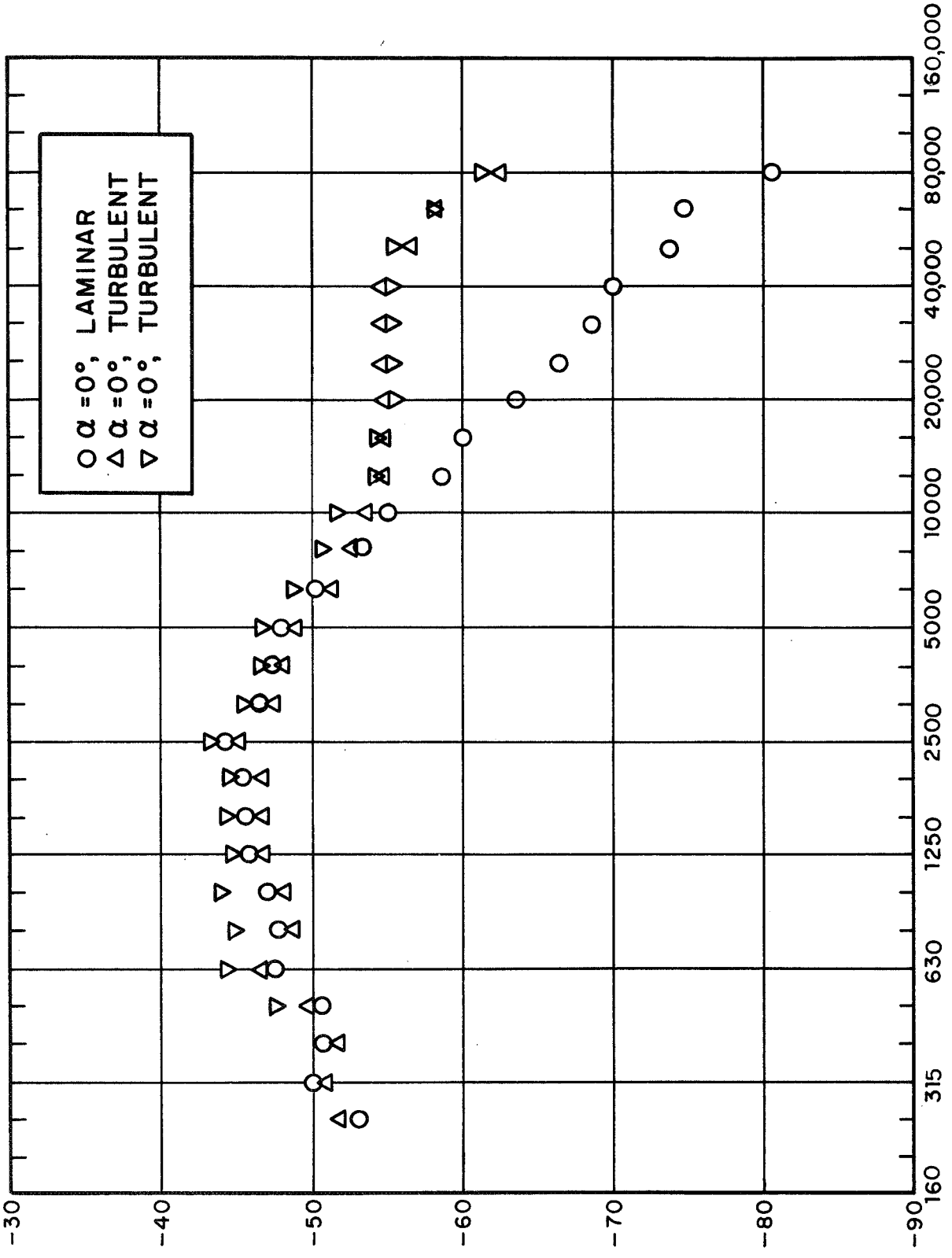

FIG. 28 CONE MODEL AT ANGLE OF ATTACK; SURFACE MICROPHONE; M = 0.67

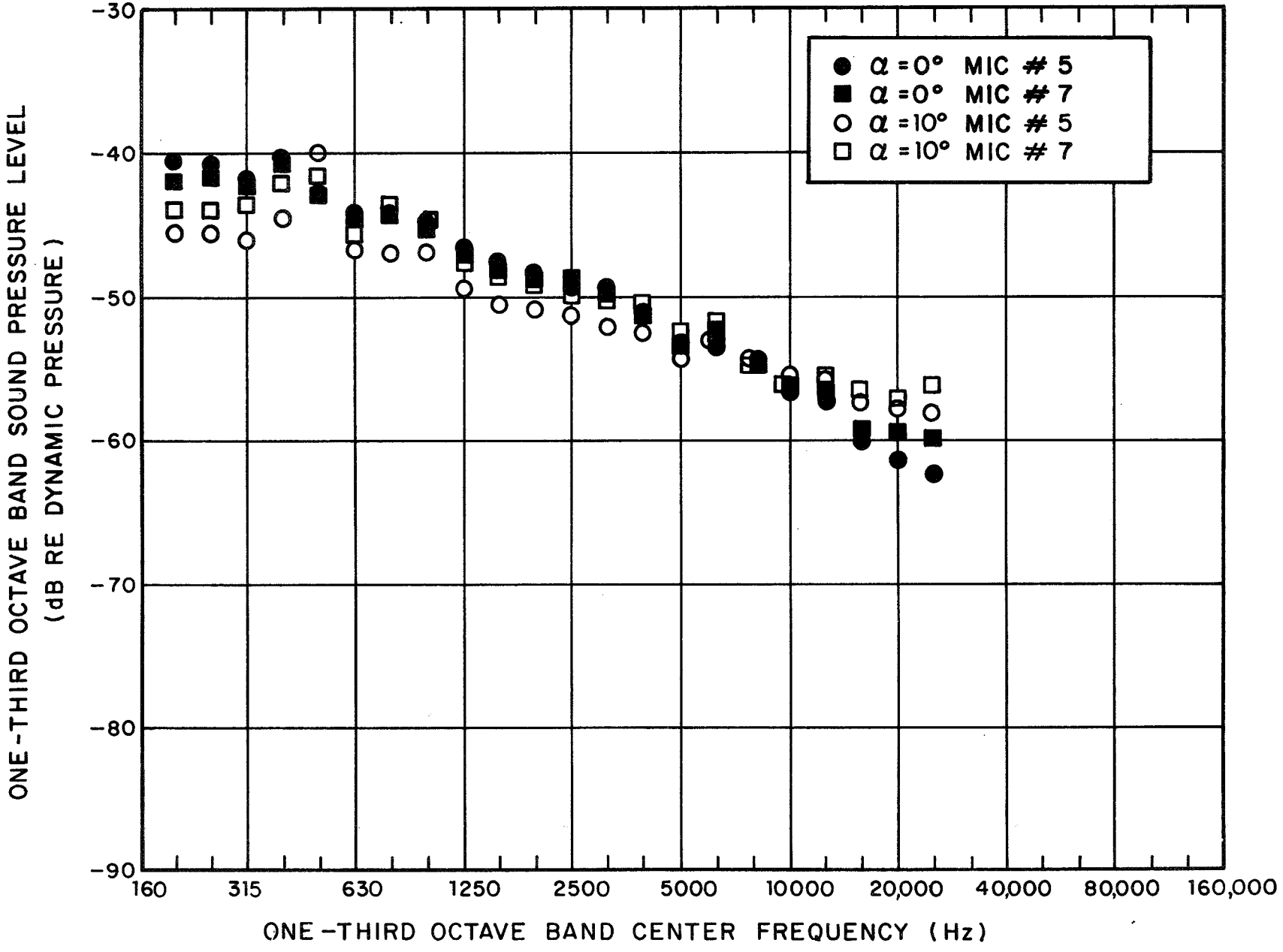

FIG. 29 CONE MODEL; BASE MICROPHONES; α = 0° and 10°; M = 0.67; P_0 = 12 psi

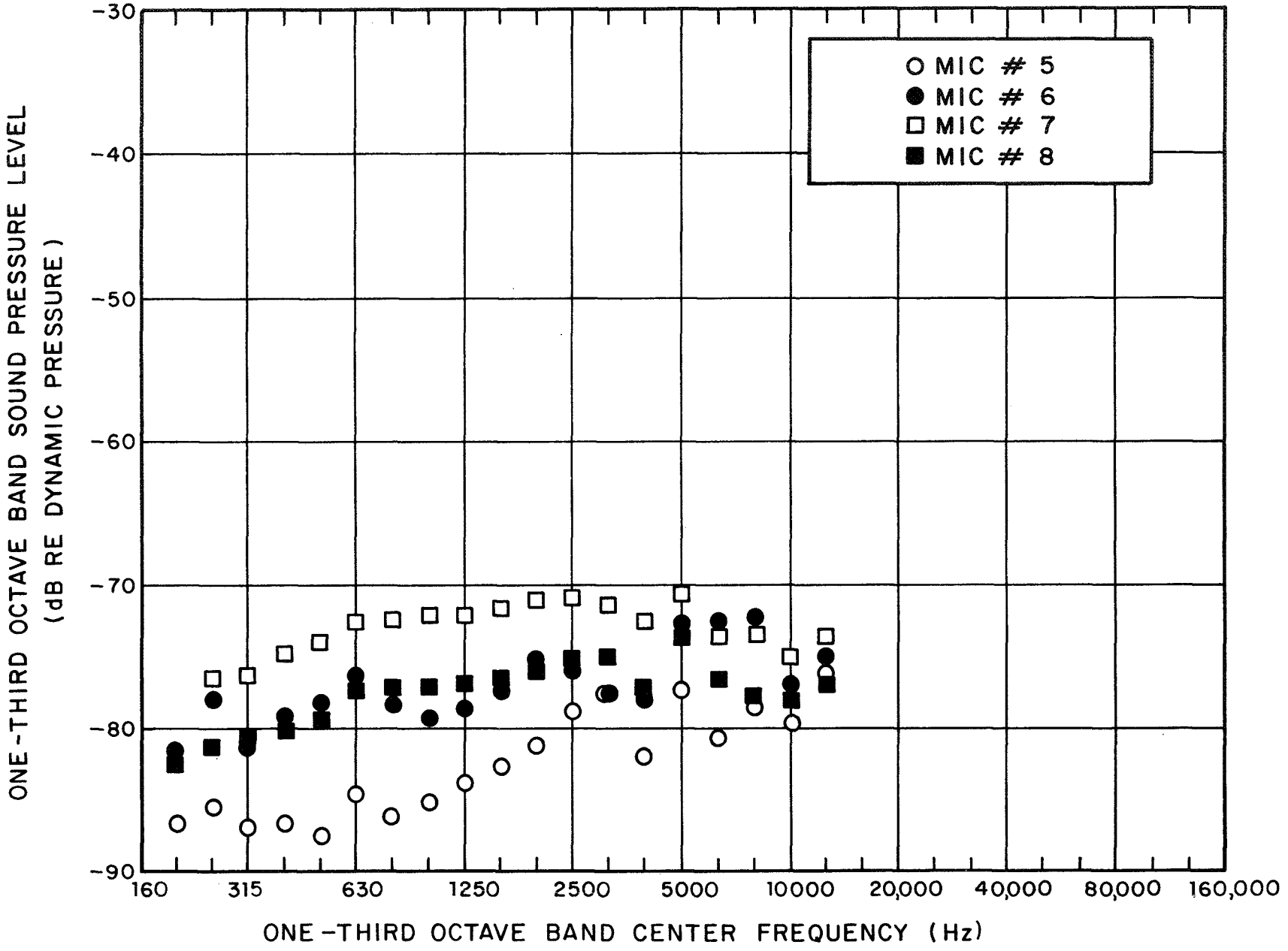

FIG. 30 CONE MODEL; BASE MICROPHONES; α = 0°; M = 4; P_0 = 30 psi

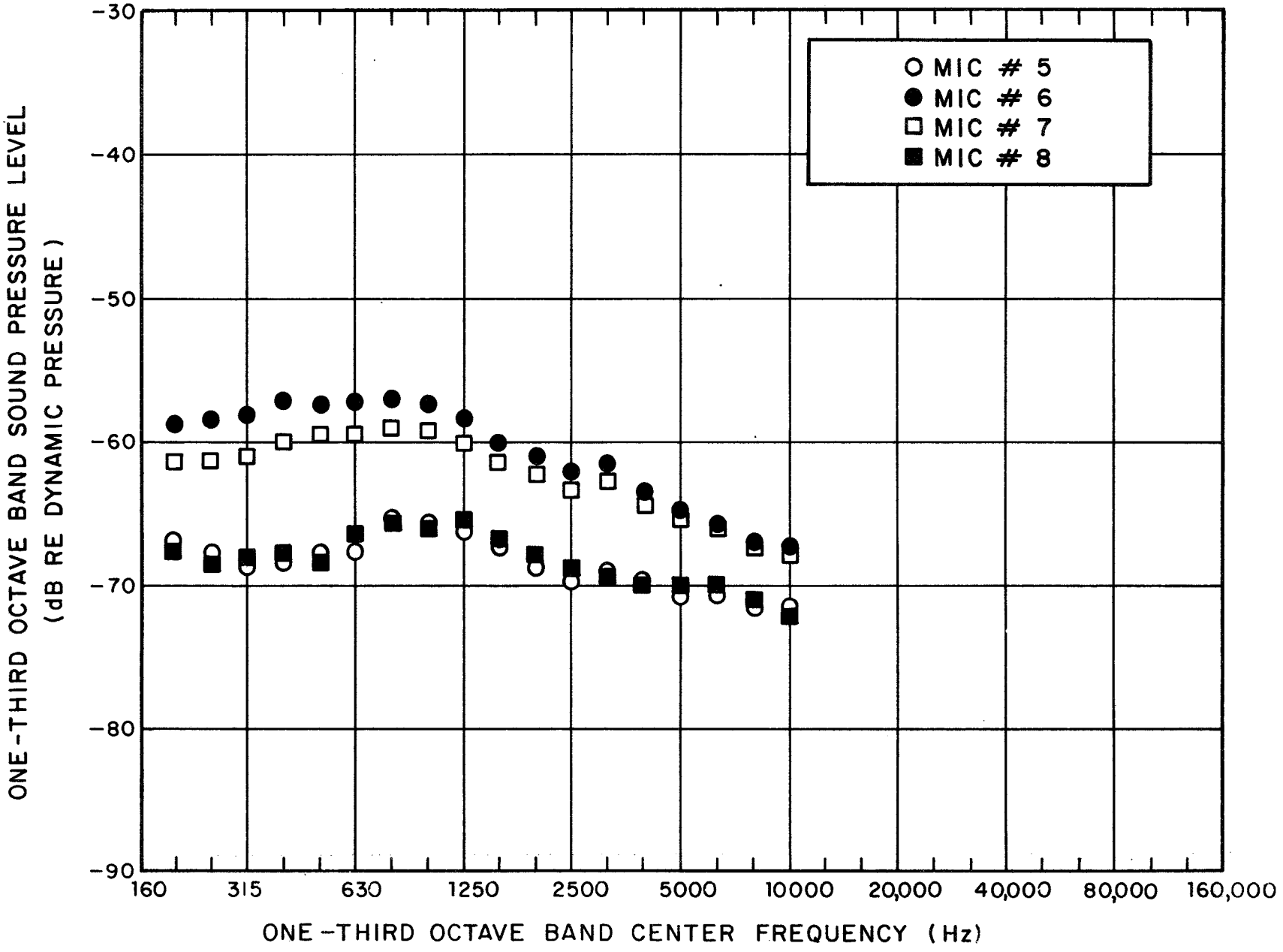

FIG. 31 CONE MODEL; BASE MICROPHONES; $\alpha = 0°$; $M = 2.5$; $P_0 = 15$ psi

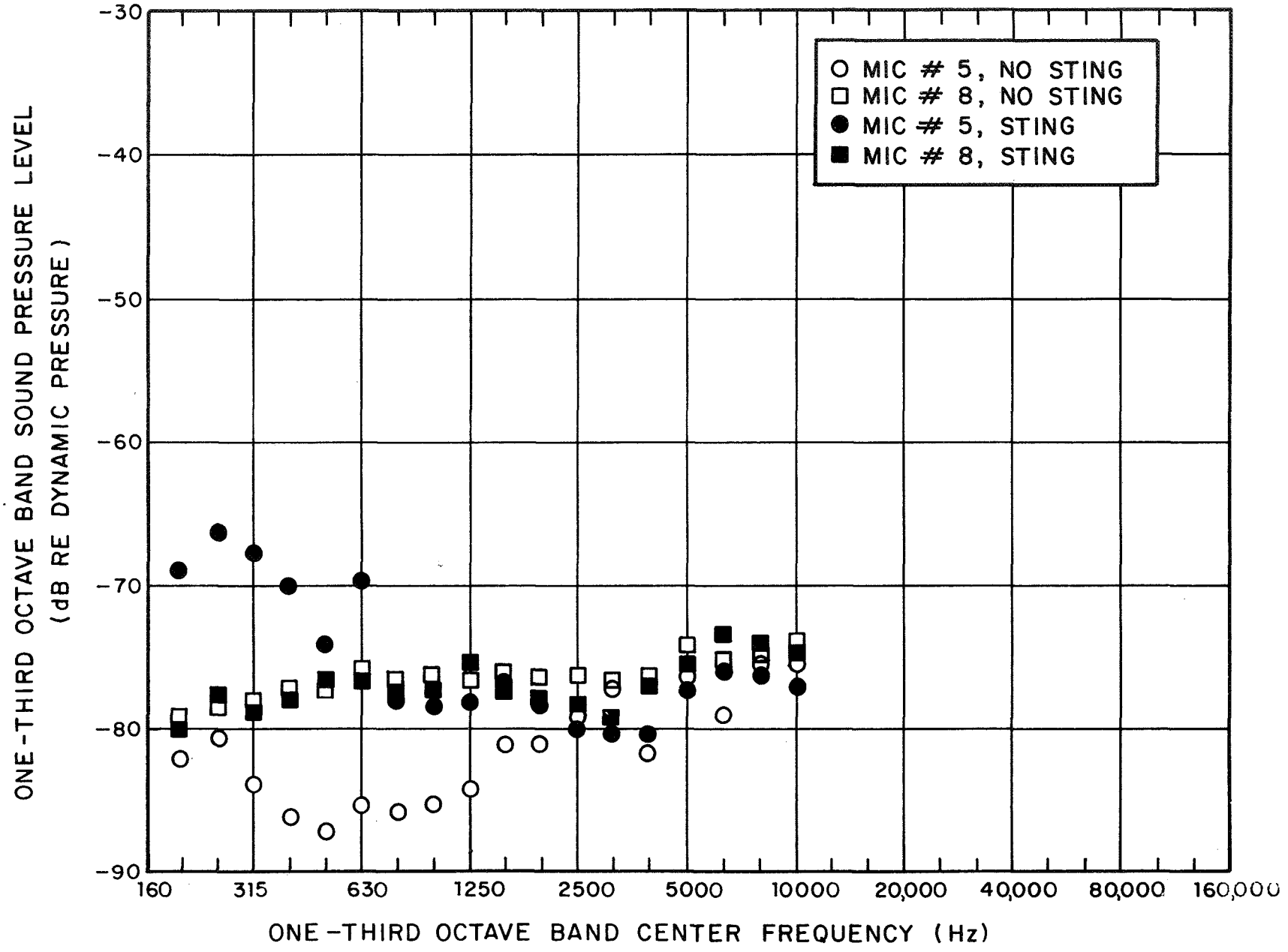

FIG. 32 CONE MODEL; BASE MICROPHONES; α = 0°; M = 4; P_0 = 15 psi. (WITH AND WITHOUT STING)

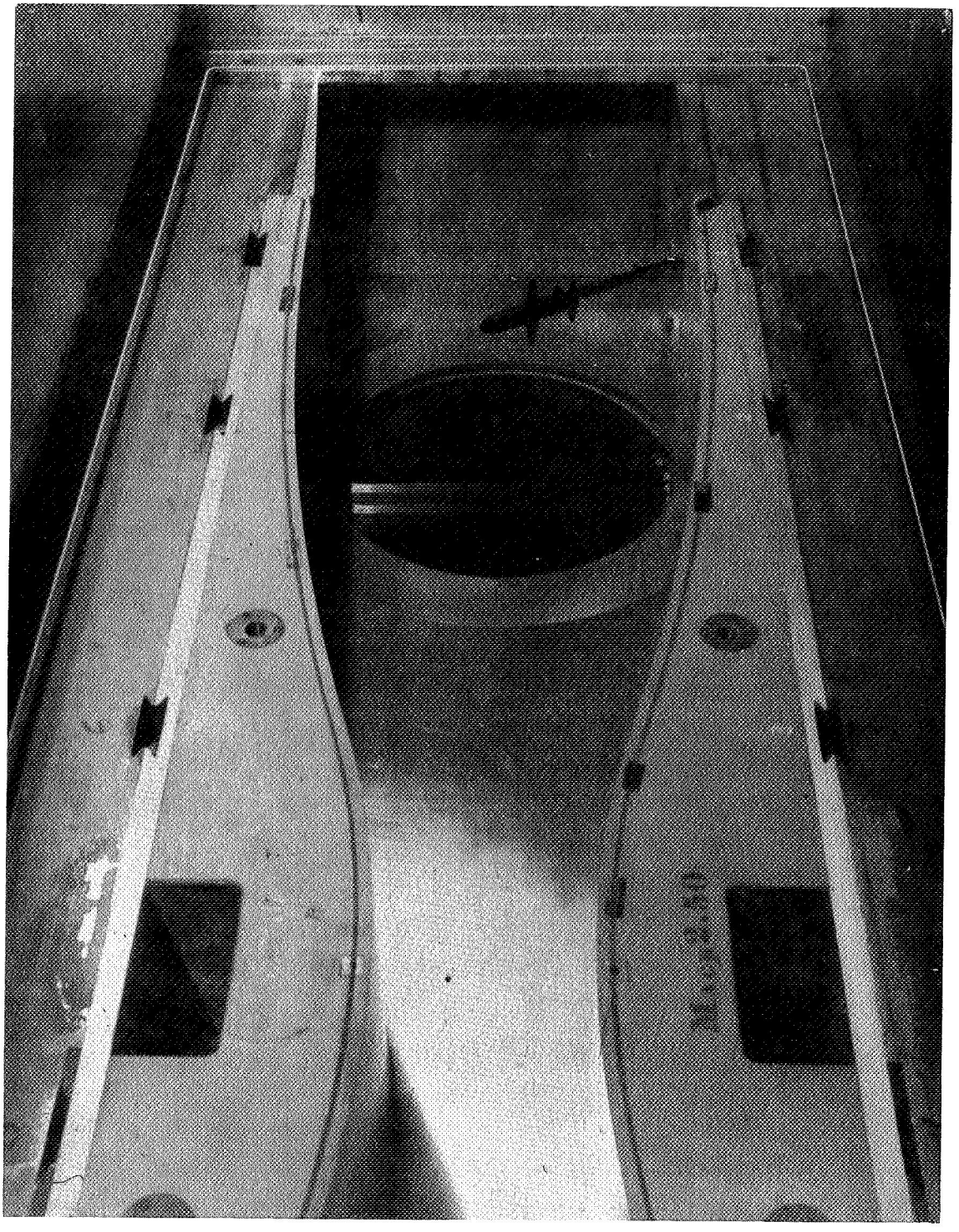

FIG. 33a LCRO MODEL A (1/250 SCALE) IN TUNNEL TEST SECTION

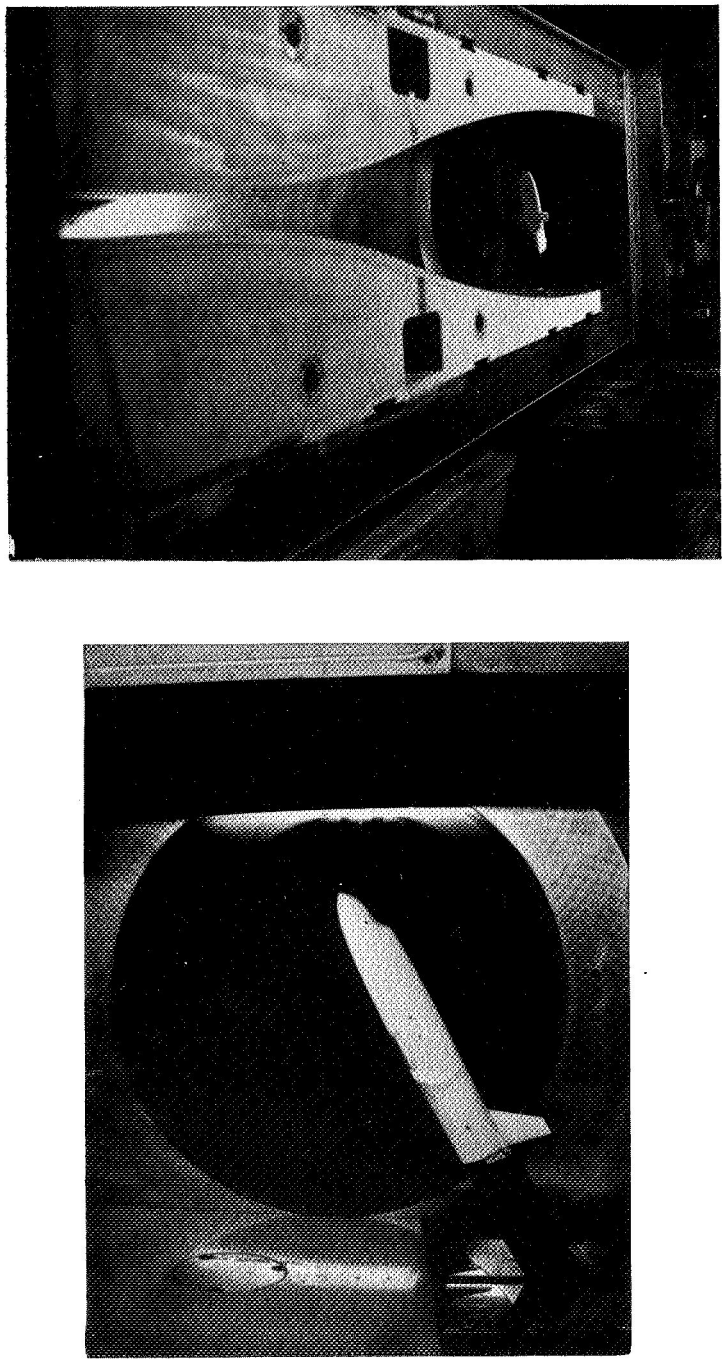

FIG. 33b LCRO MODEL B (1/125 SCALE) IN TUNNEL TEST SECTION

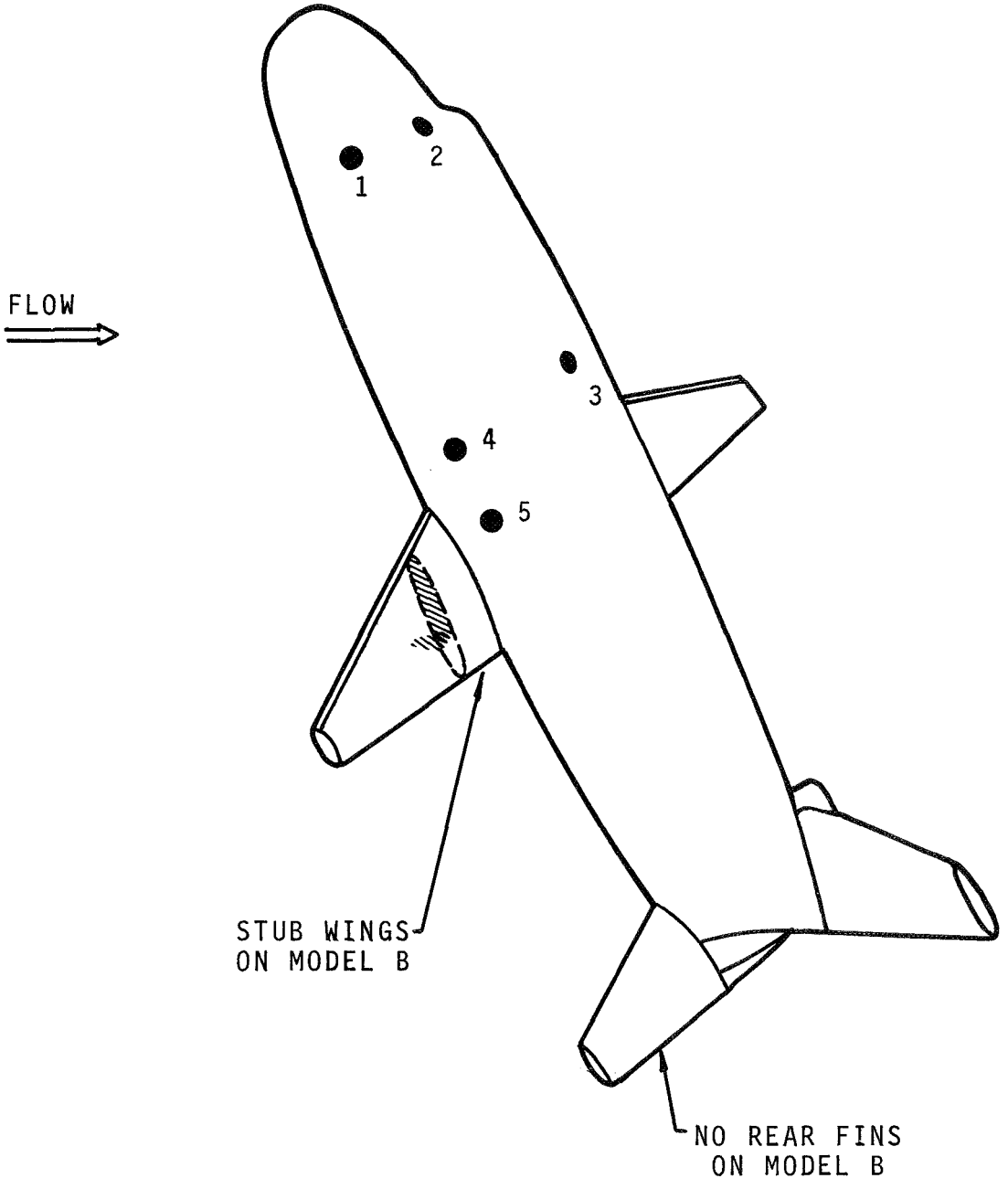

FIG. 34 LOCATION OF MICROPHONE ON MODELS A AND B

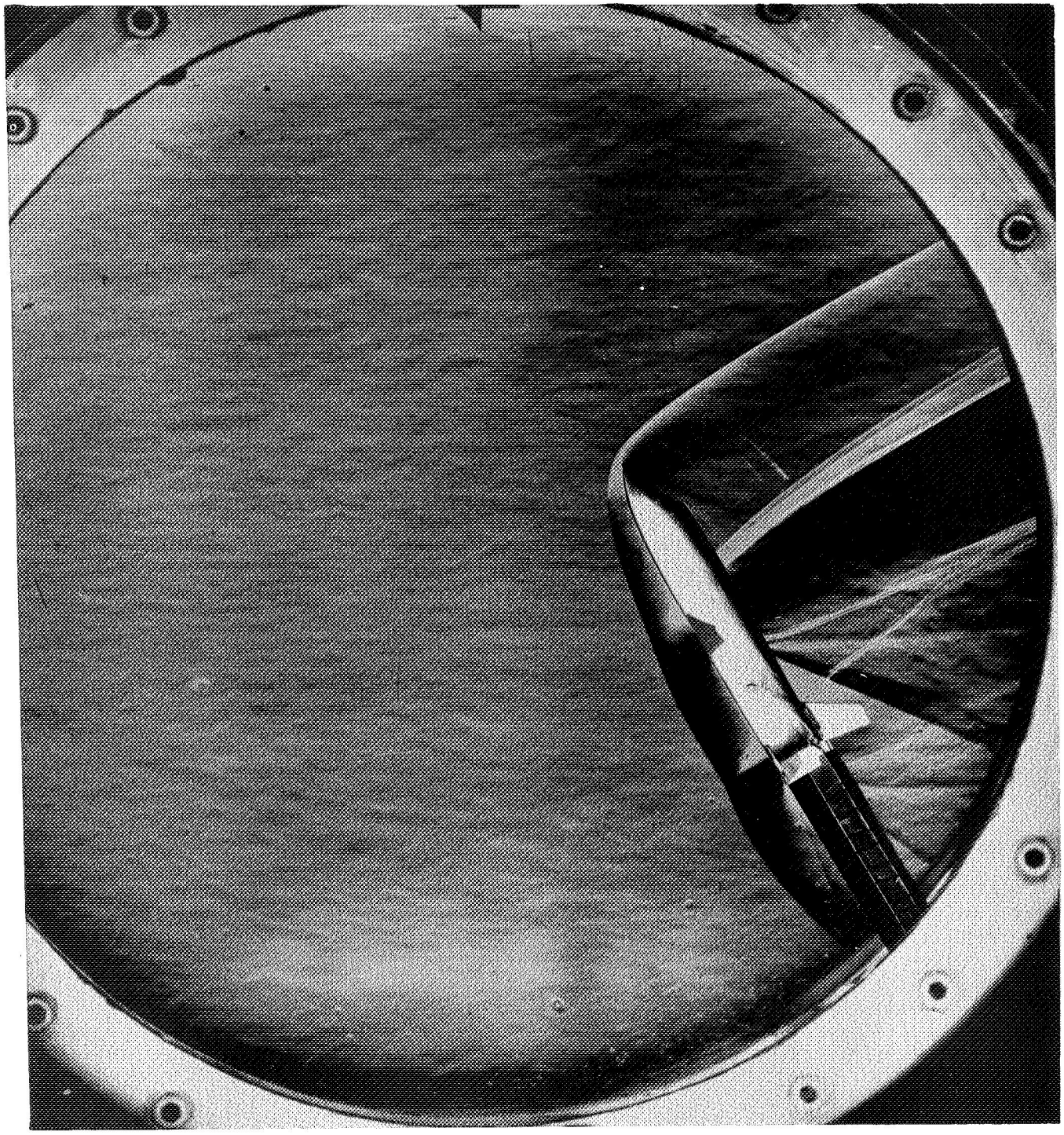

FIG. 35 SCHLIERENOPTICAL FLOW VISUALIZATION; MODEL A; M = 2.5

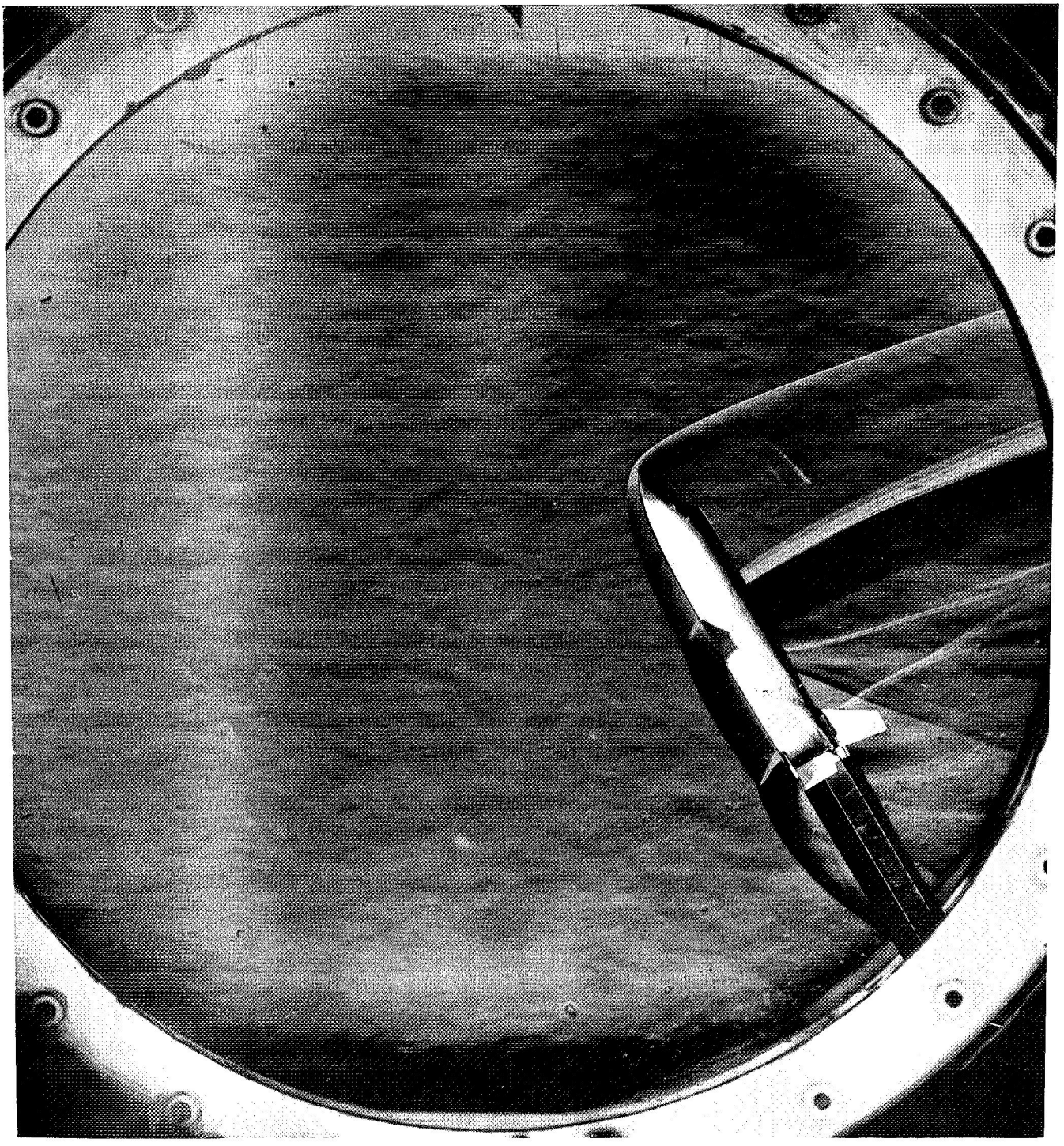

FIG. 36 SCHLIERENOPTICAL FLOW VISUALIZATION; MODEL A; M = 4

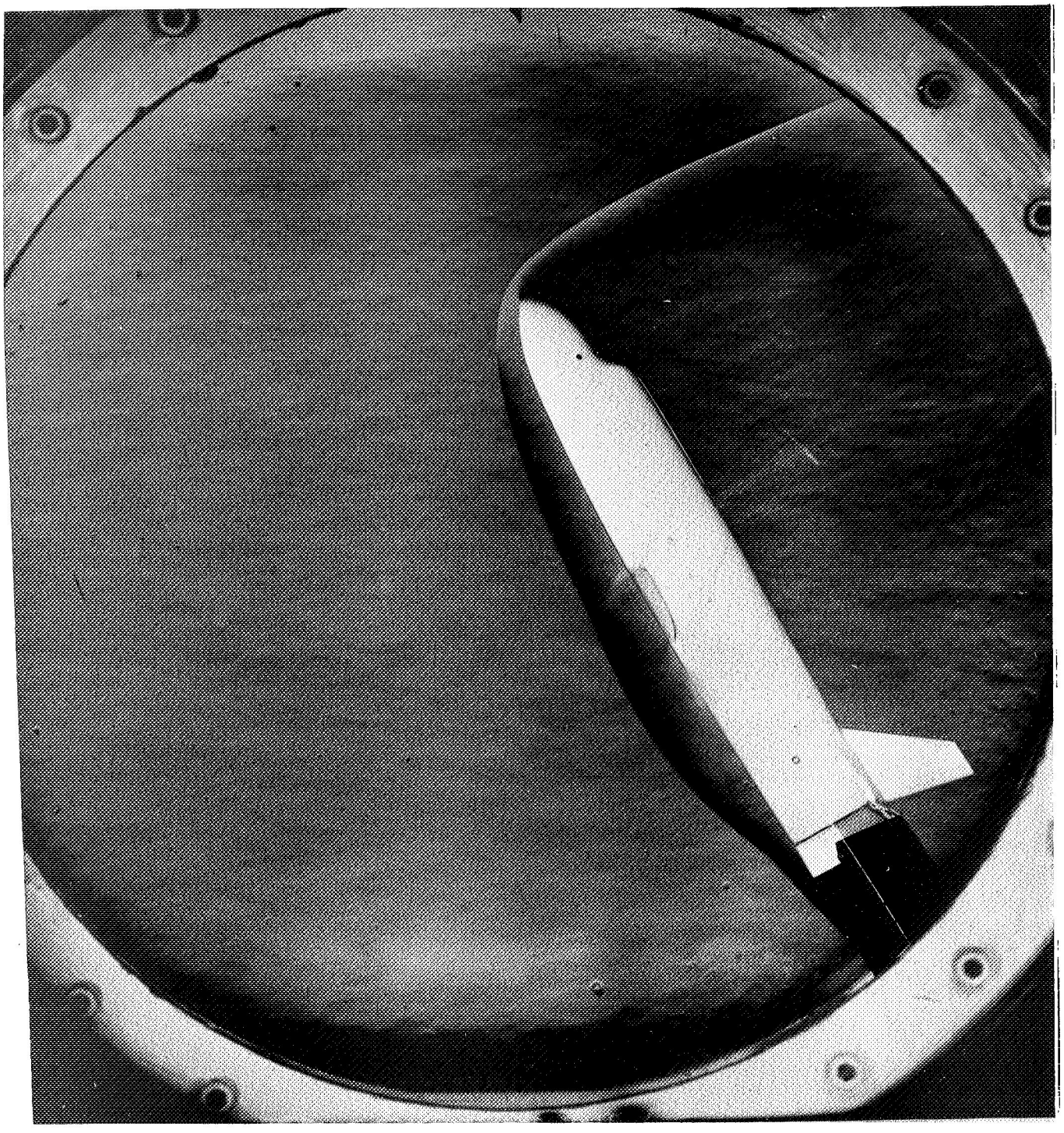

FIG. 37 SCHLIERENOPTICAL FLOW VISUALIZATION; MODEL B; M = 4

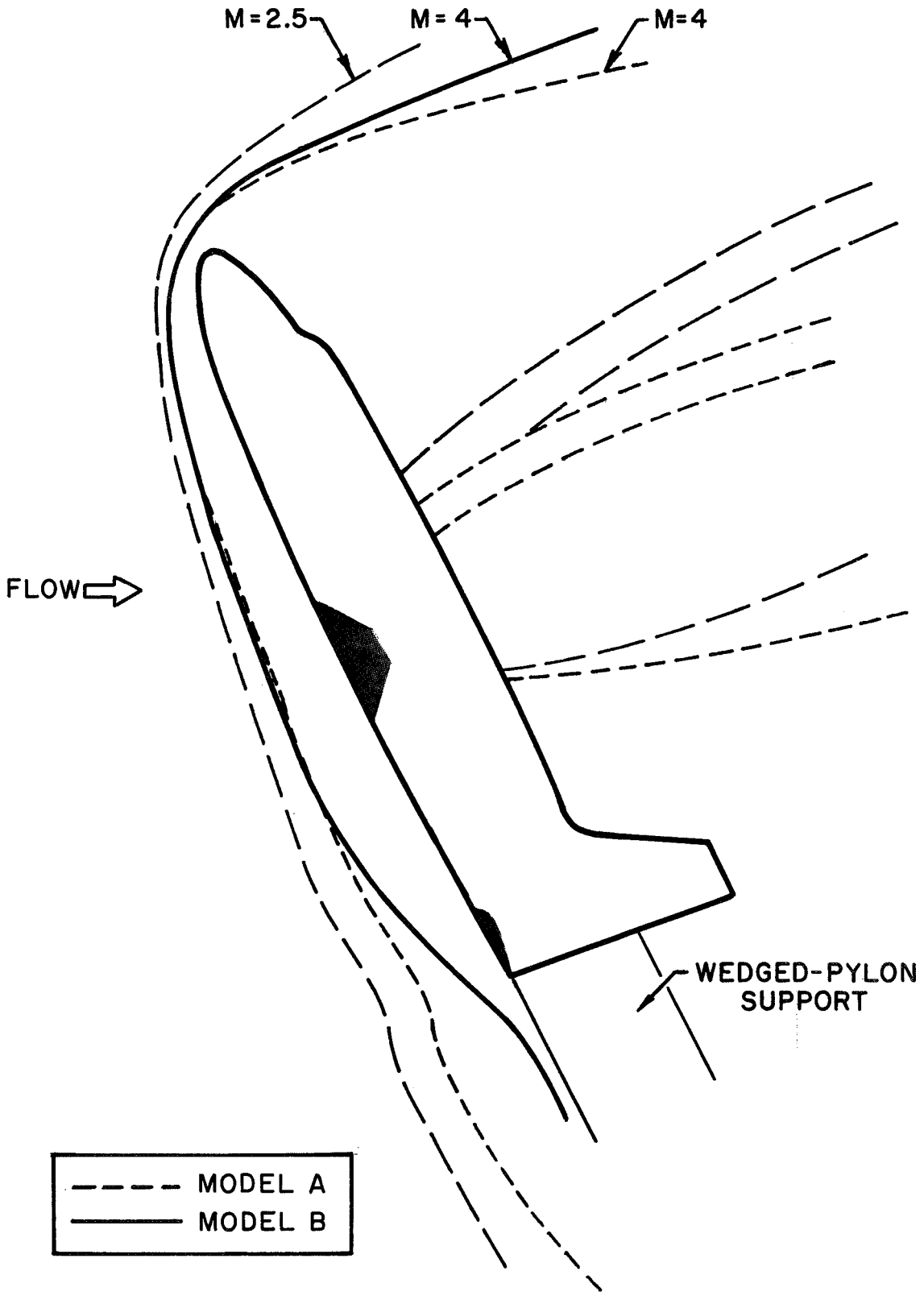

FIG. 38 SHOCK PATTERN ON LCRO AS M_∞=2.5 AND 4
(NOTE THAT MODEL B HAS NO WINGS)

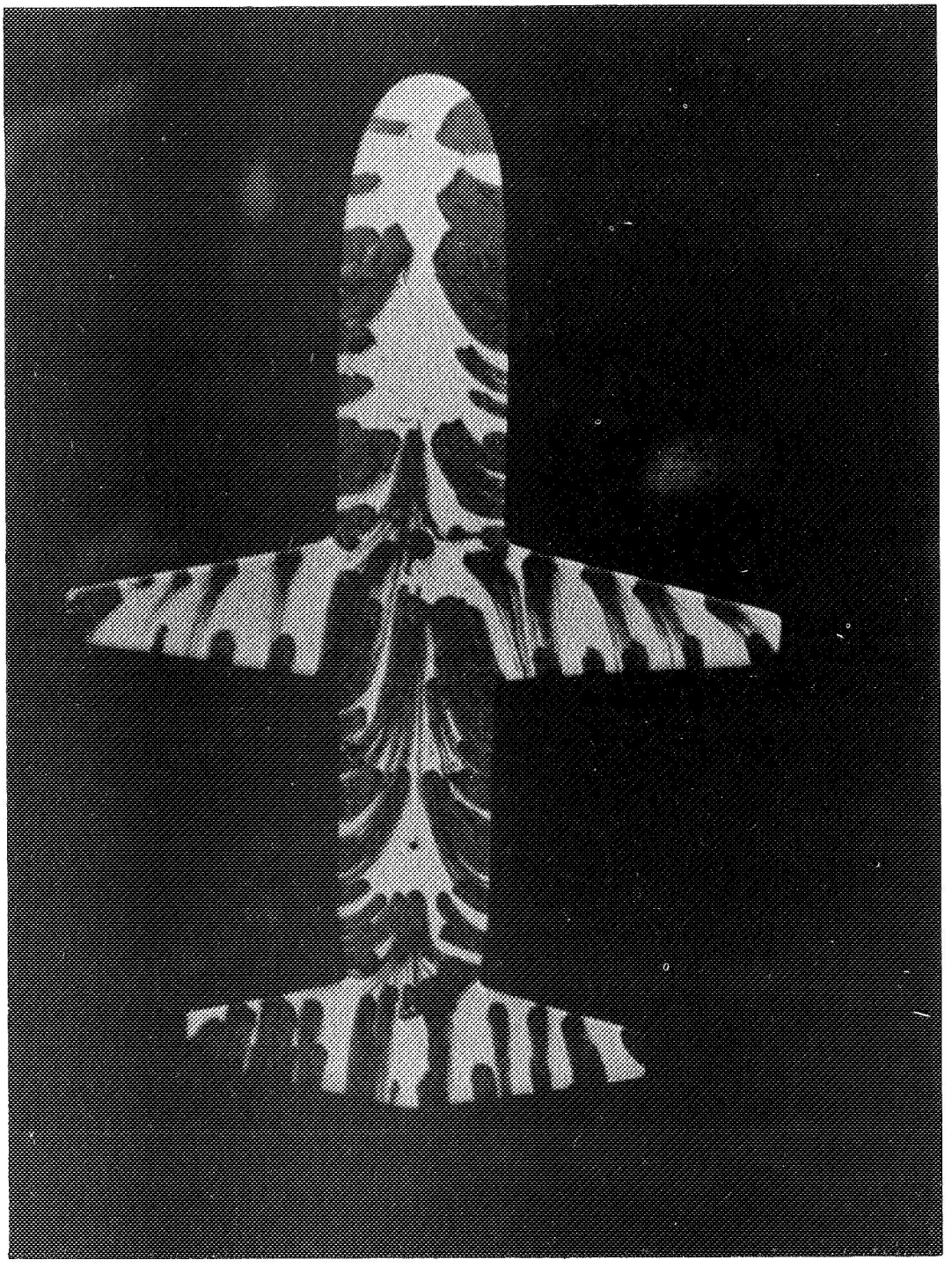

FIG. 39 FLOW PATTERN ON WINDWARD SIDE; MODEL A; α = 60°; M = 2.5

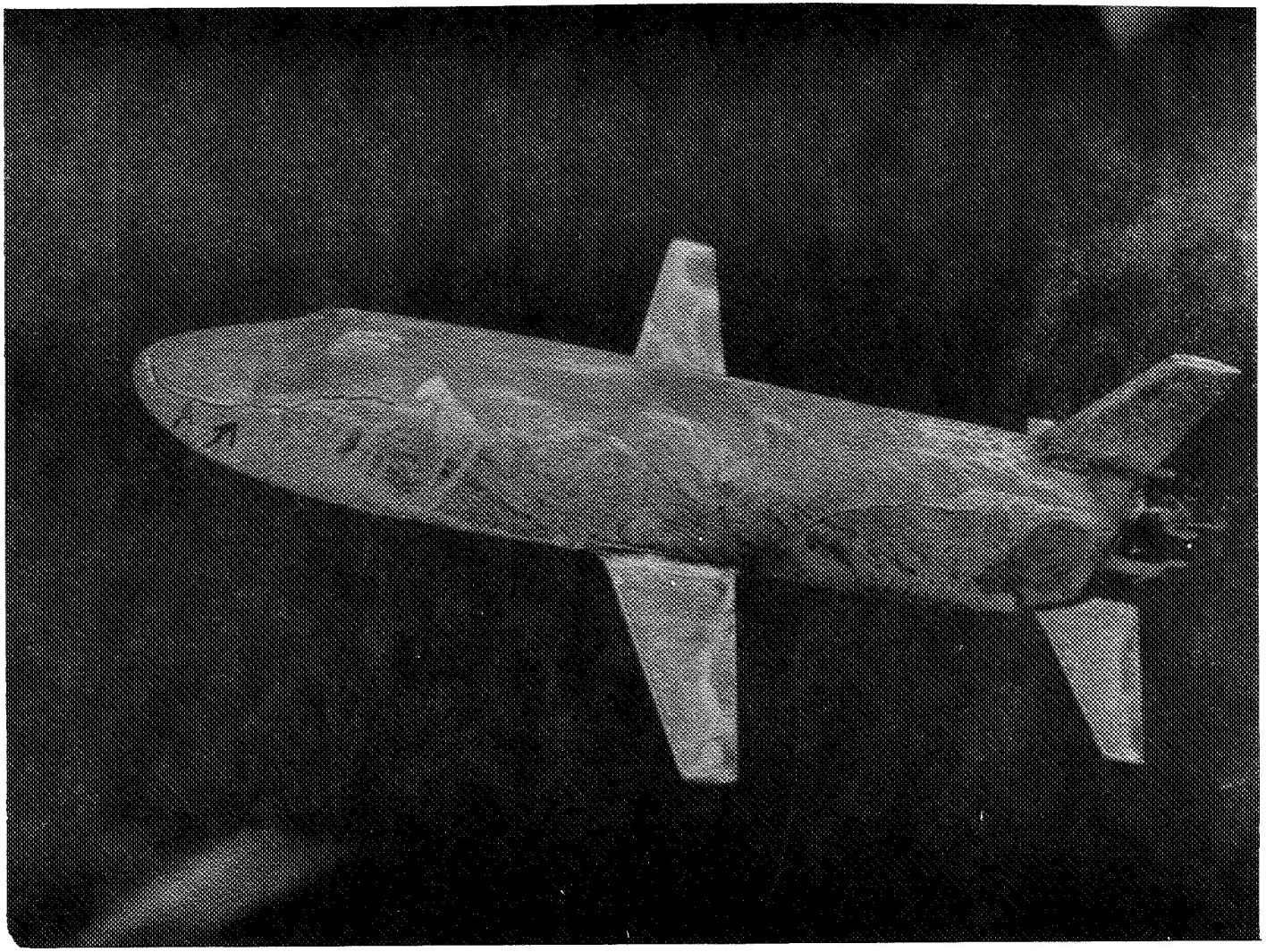

FIG. 40 FLOW PATTERN ON LEEWARD SIDE; MODEL A; α = 60°; M = 2.5

FIG. 41. FLOW PATTERN ON LEEWARD SIDE; MODEL B; $\alpha = 60°$; M = 4

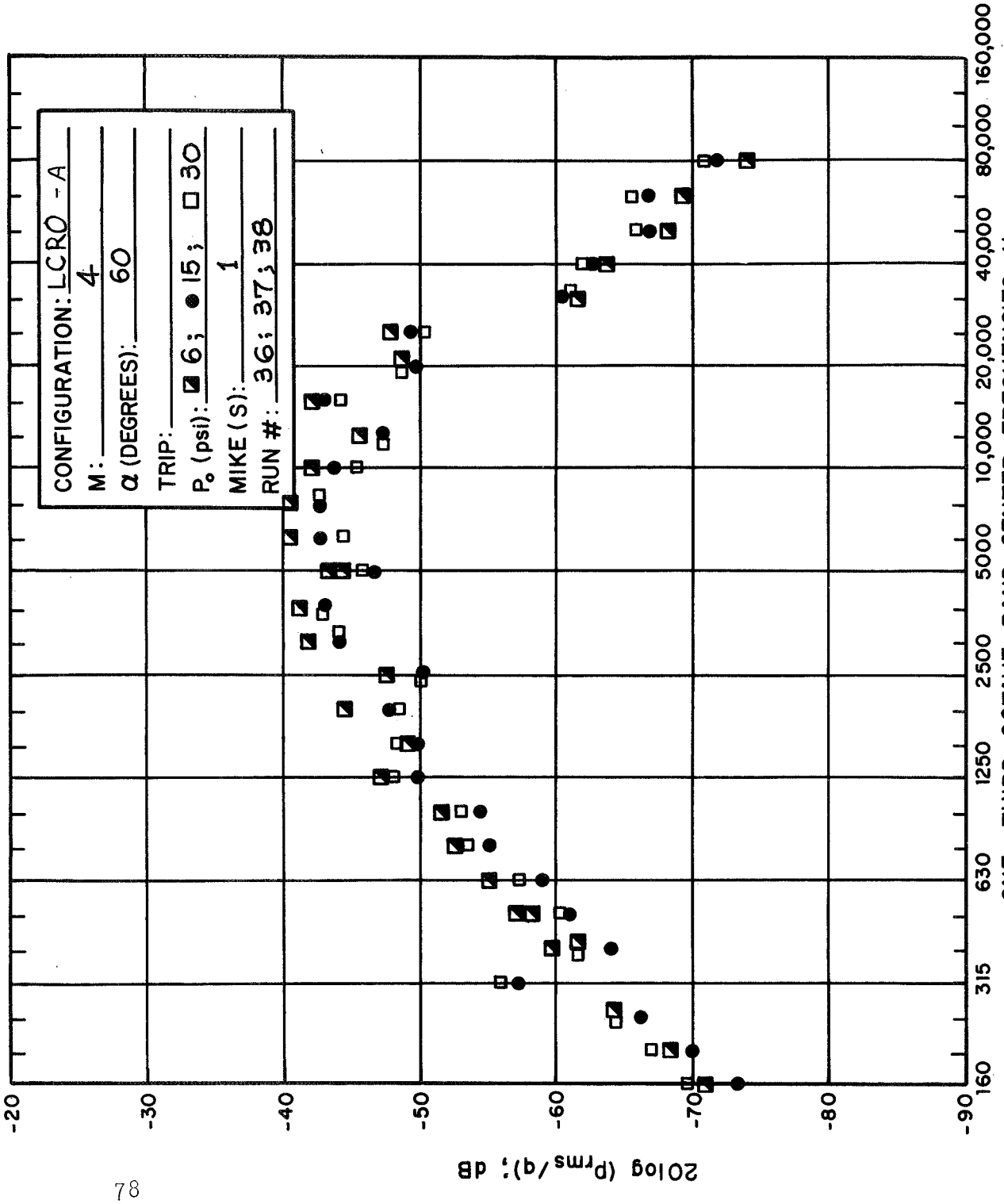

FIG. 42a SEMINORMALIZED PRESSURE SPECTRA; MODEL A; M=4; MICROPHONE #1

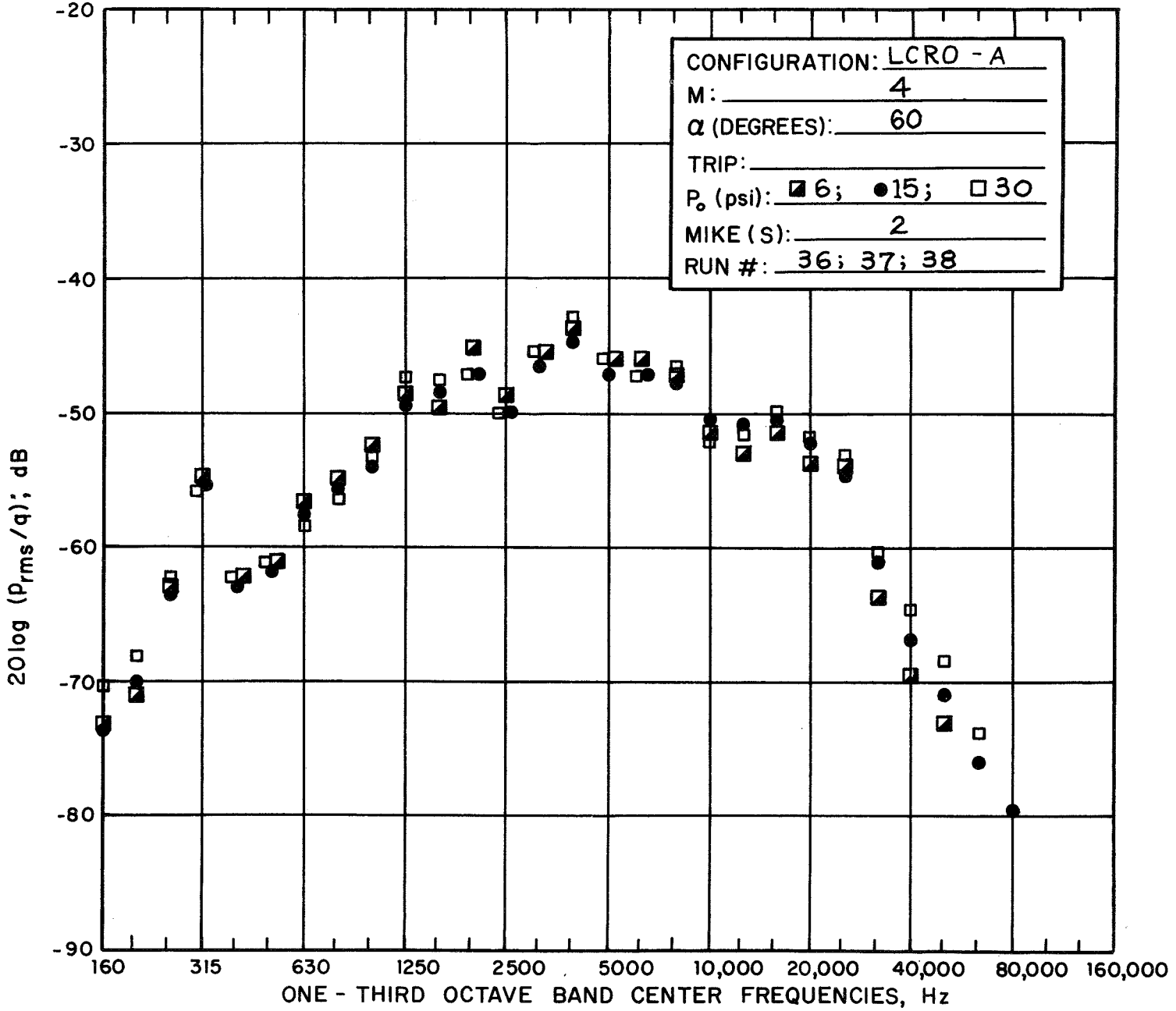

FIG. 42b SEMINORMALIZED PRESSURE SPECTRA; MODEL A; M=4; MICROPHONE #2

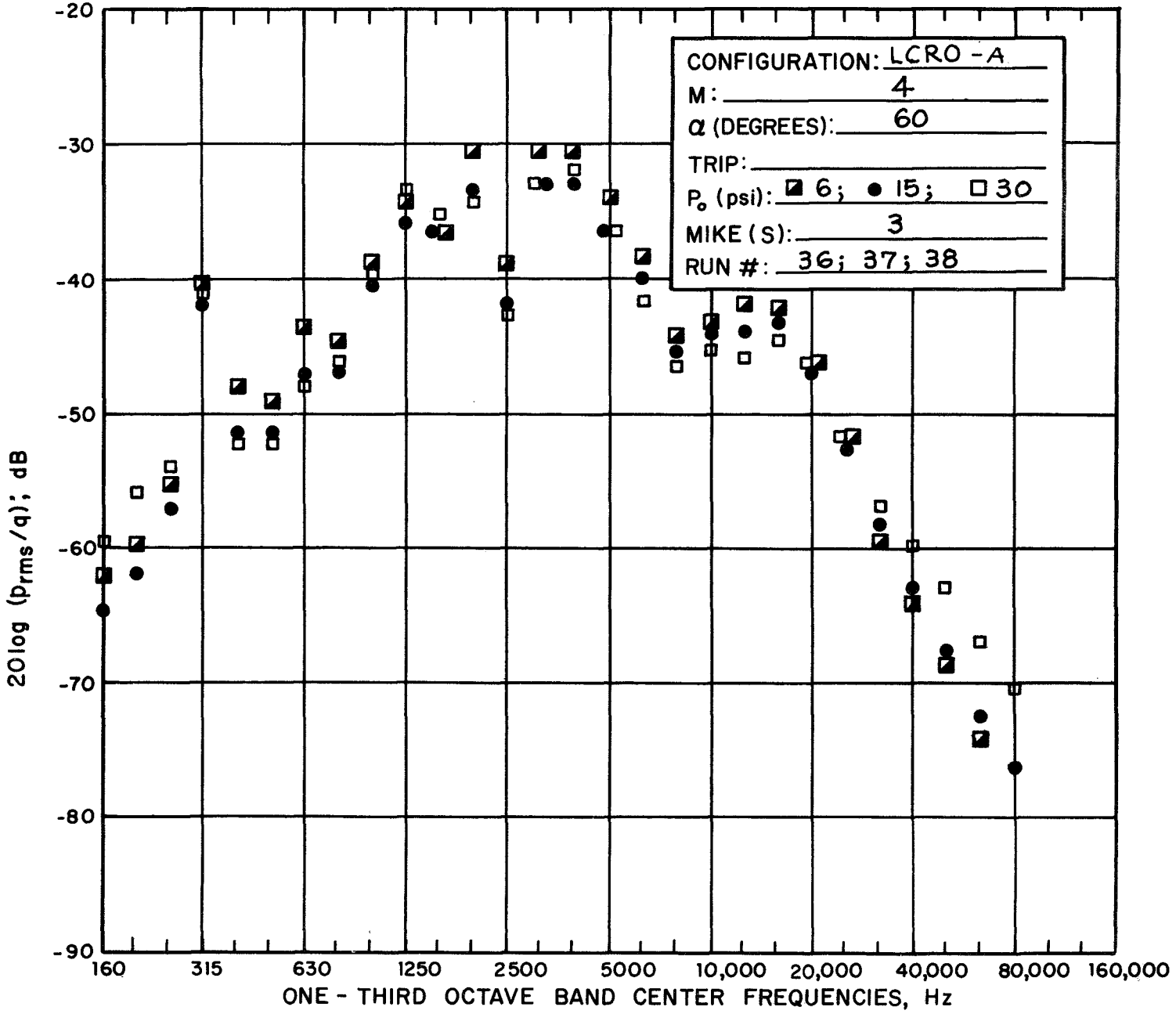

FIG. 42c SEMINORMALIZED PRESSURE SPECTRA; MODEL A; M=4; MICROPHONE #3

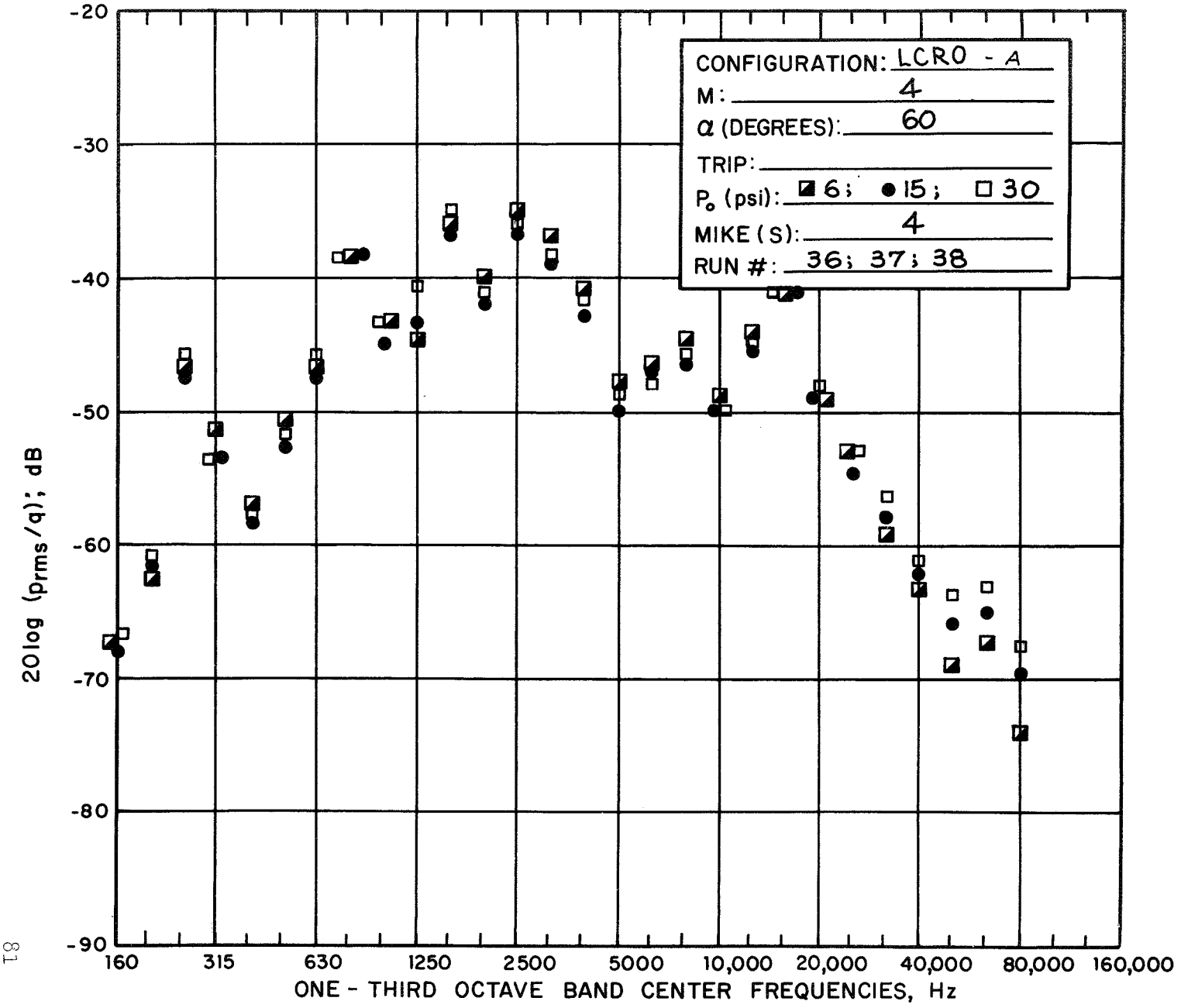

FIG. 42d SEMINORMALIZED PRESSURE SPECTRA; MODEL A; M=4; MICROPHONE #4

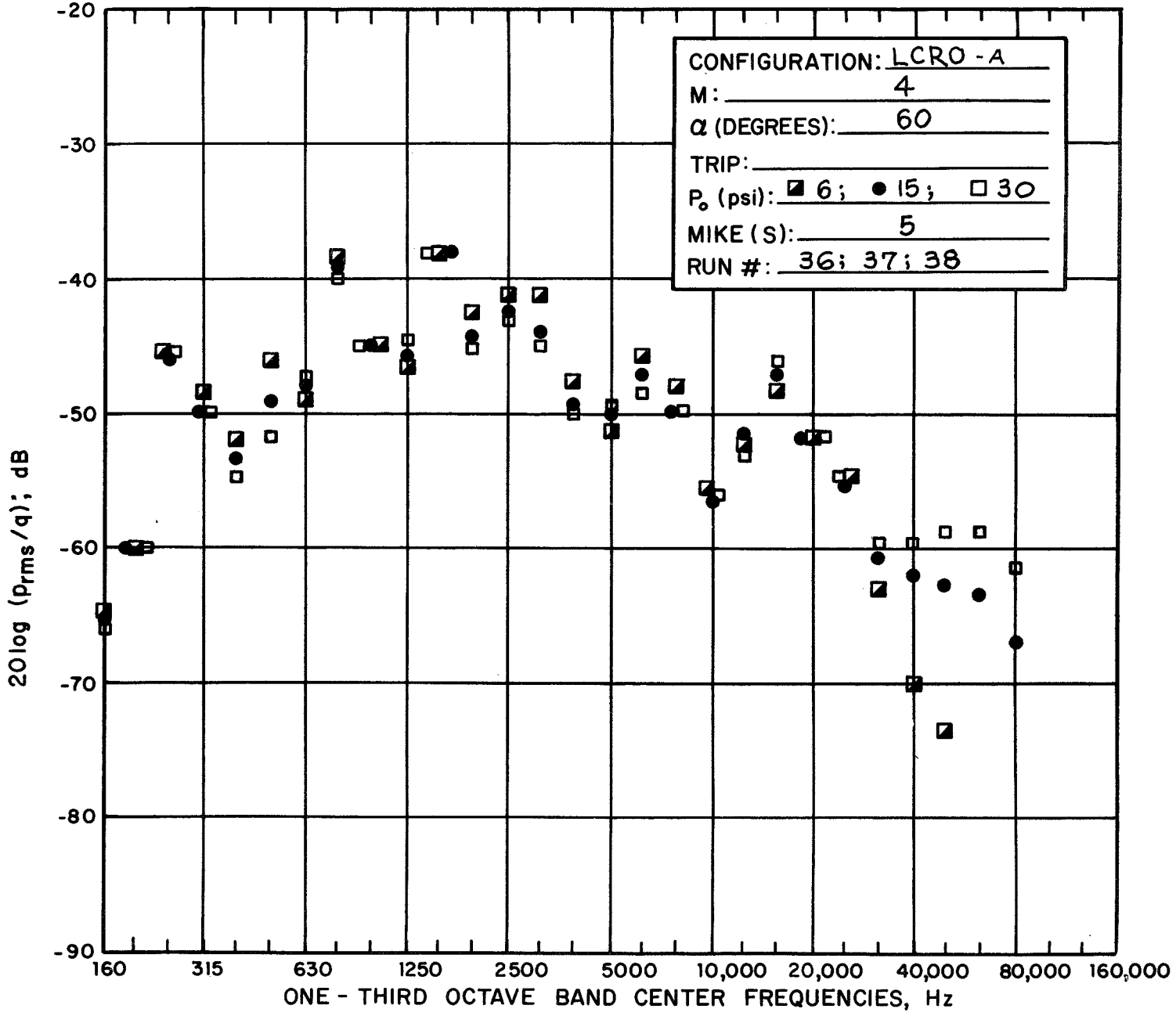

FIG. 42e SEMINORMALIZED PRESSURE SPECTRA; MODEL A; M=4; MICROPHONE #5

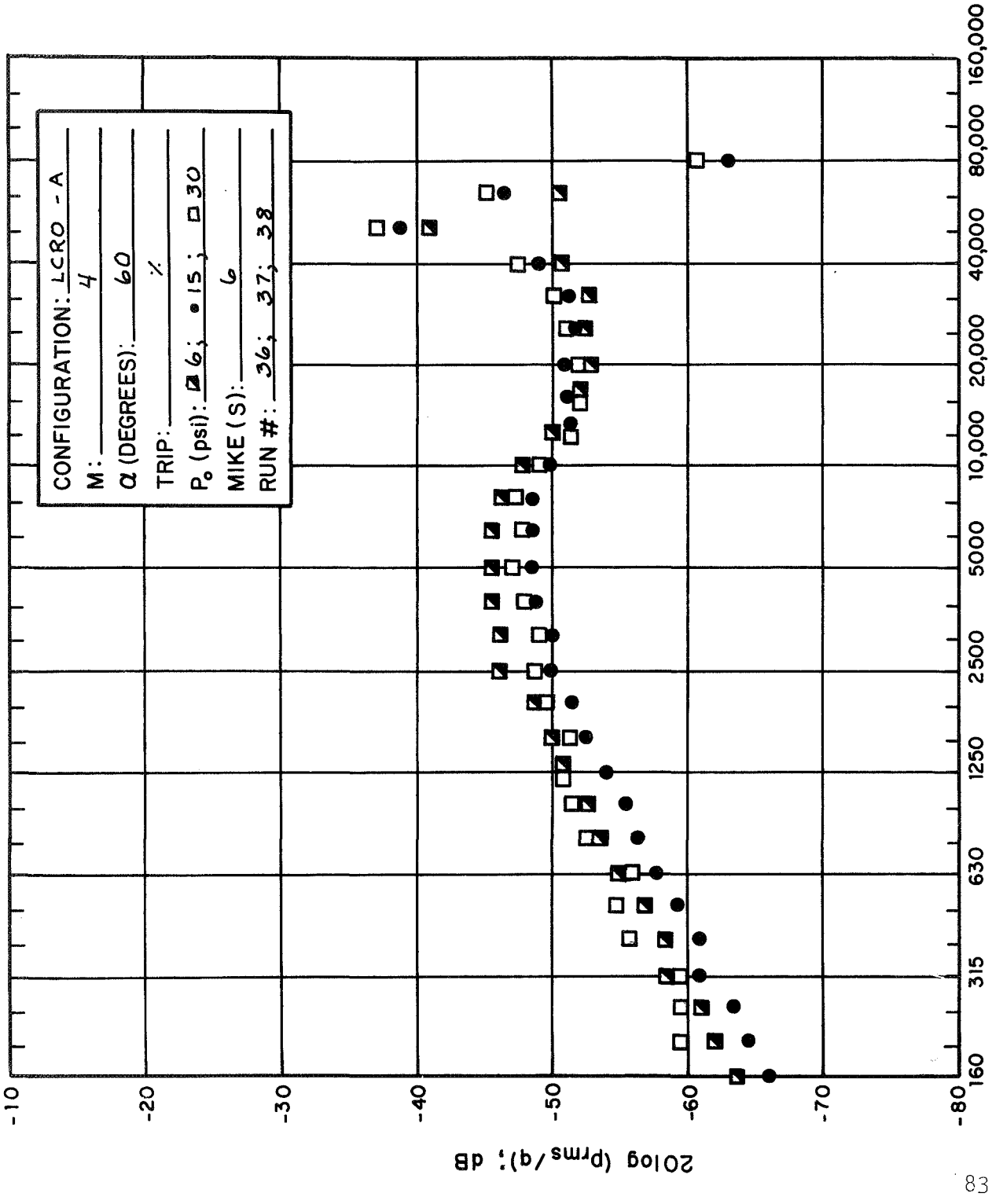

FIG. 42f SEMINORMALIZED PRESSURE SPECTRA; MODEL A; M=4; MICROPHONE #6

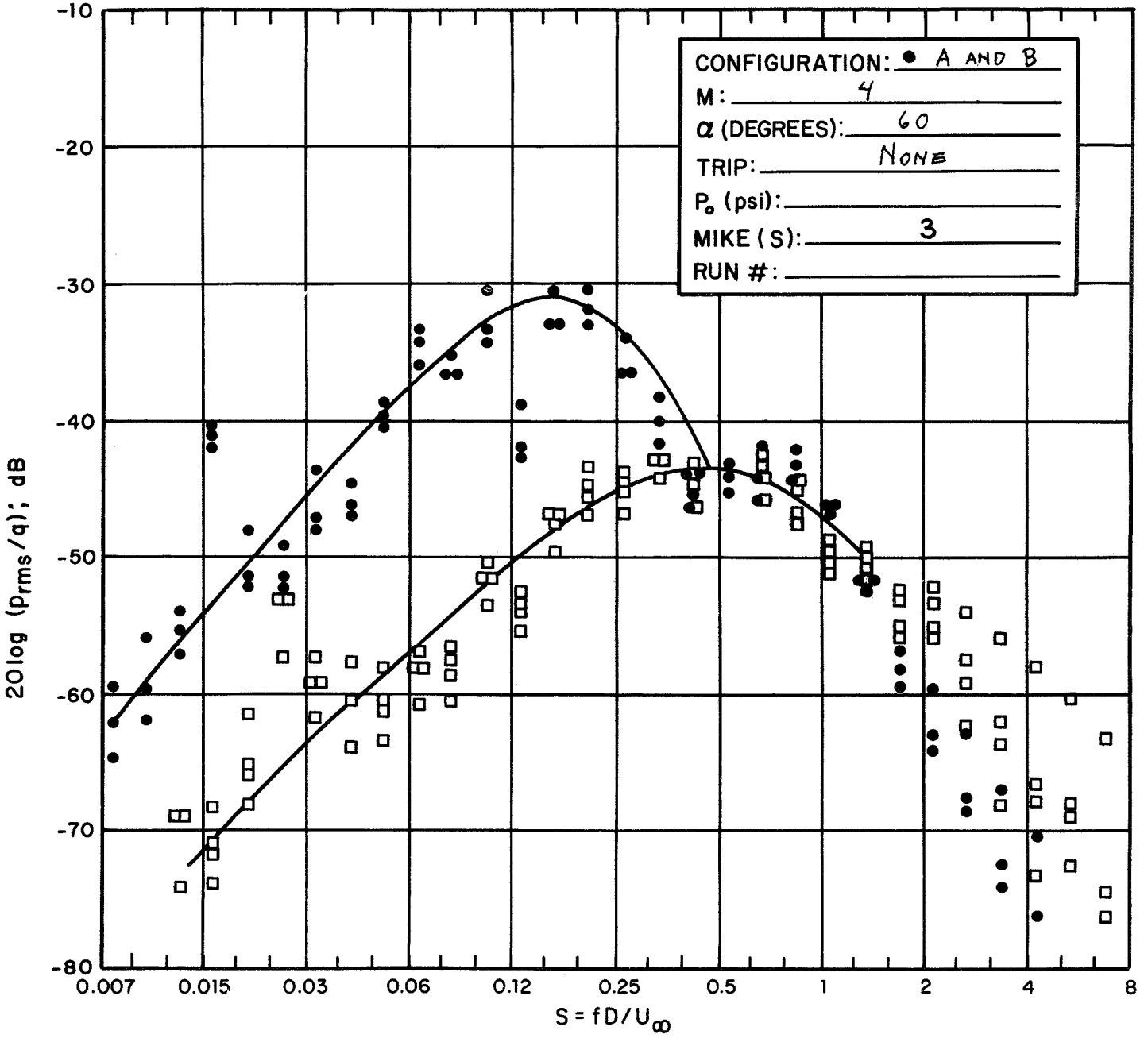

FIG. 43 NORMALIZED PRESSURE SPECTRA; MODELS A AND B; M=4; MICROPHONE #3

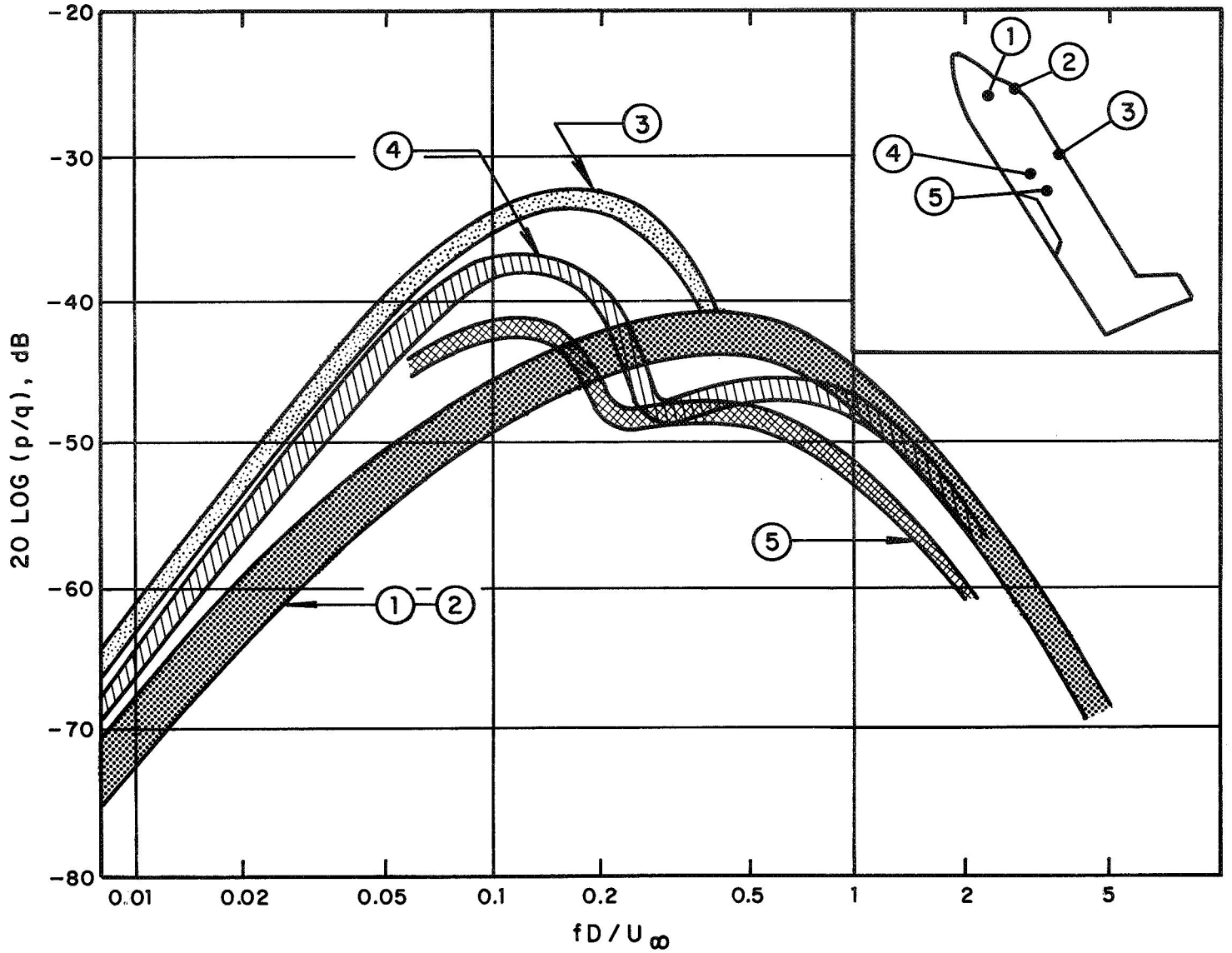

FIG. 44 SUMMARY OF TEST RESULTS FOR M = 4

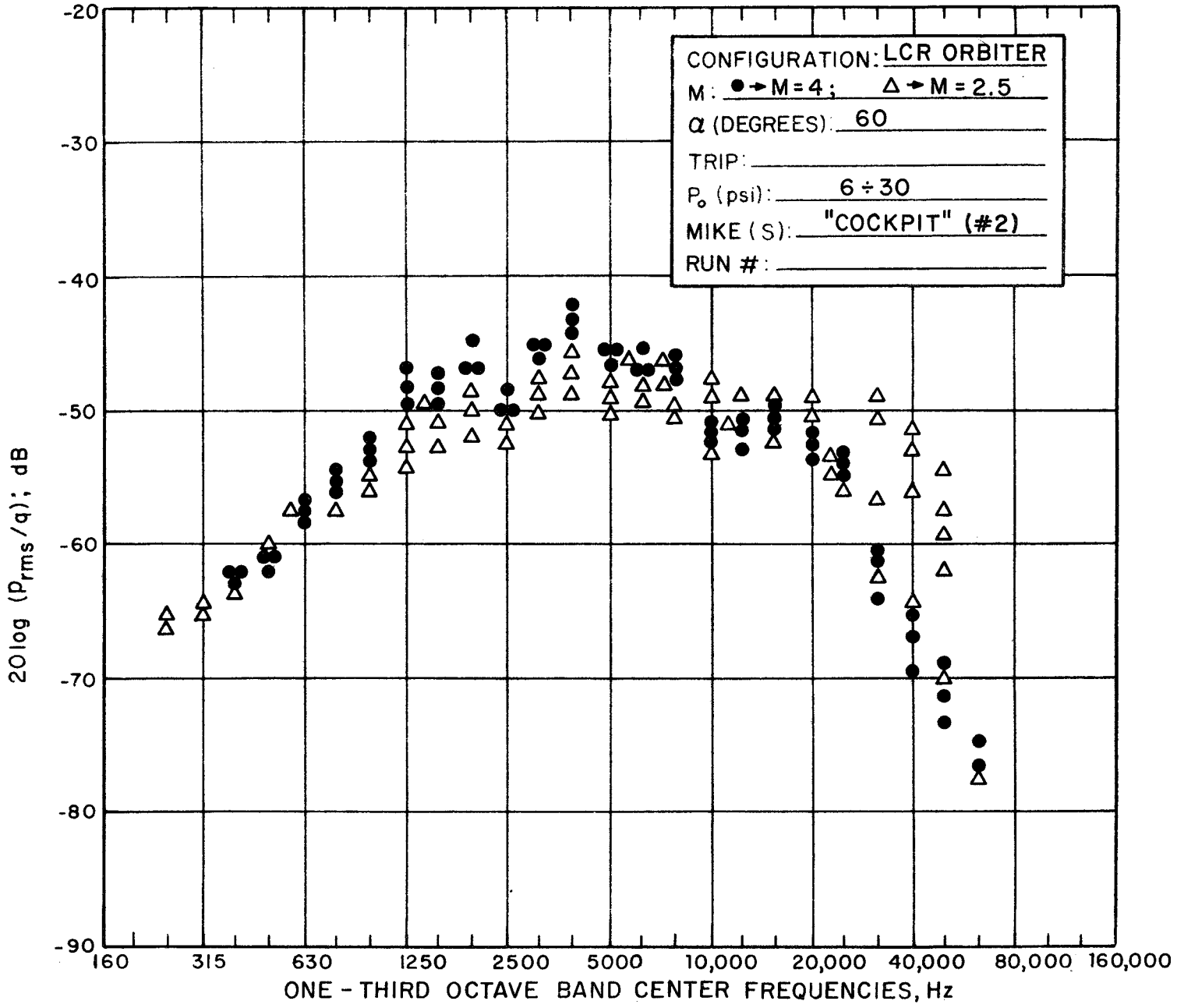

FIG. 45 NORMALIZED SPECTRA; MODEL A; M = 4 AND 2.5; MICROPHONE #2

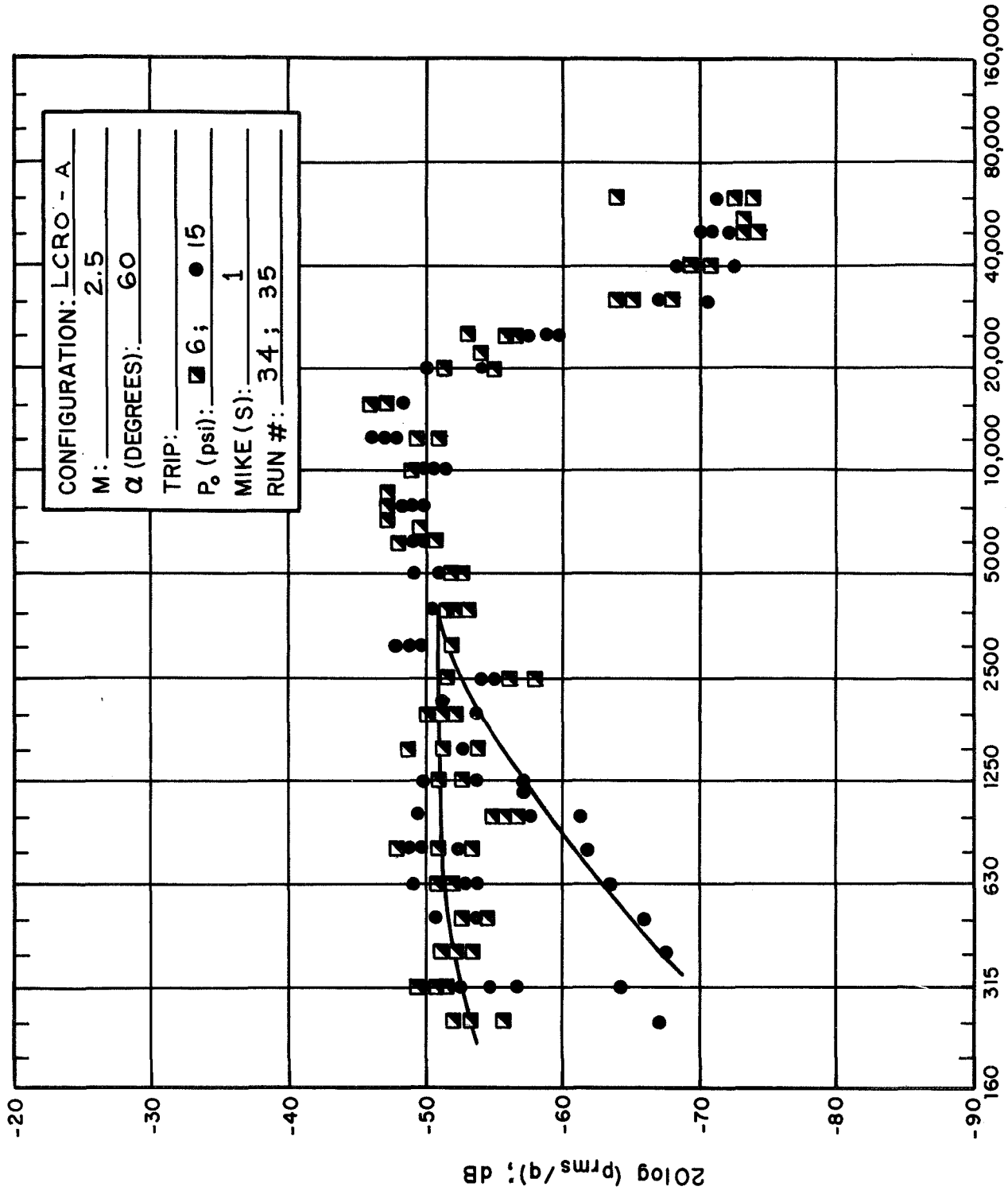

FIG. 46 SEMINORMALIZED PRESSURE SPECTRA; MODEL A; M = 2.5; MICROPHONE #1

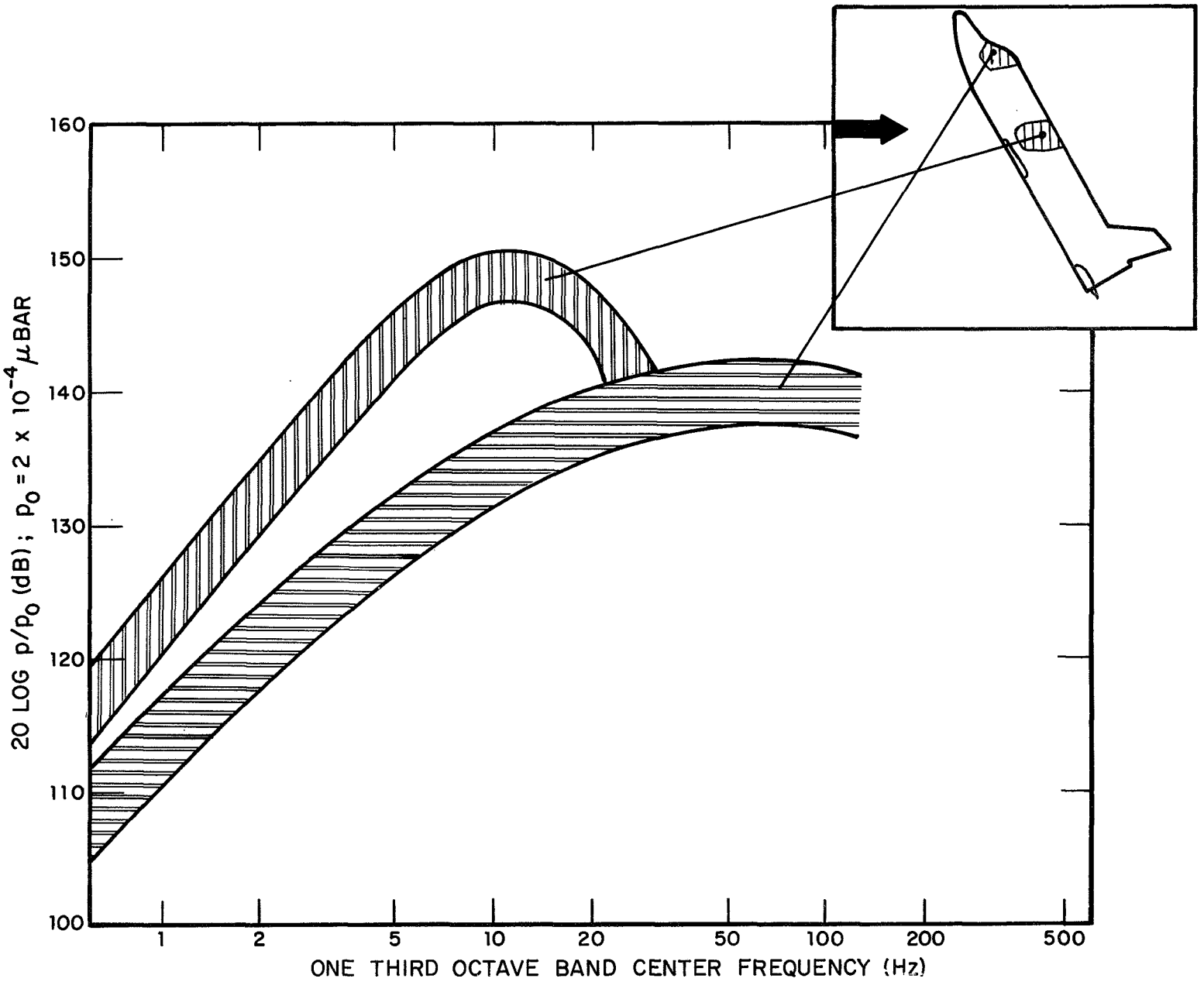

FIG. 47 ESTIMATED FLUCTUATING PRESSURE SPECTRA AT TWO LOCATIONS ON FULL-SCALE LCRO AT M = 4

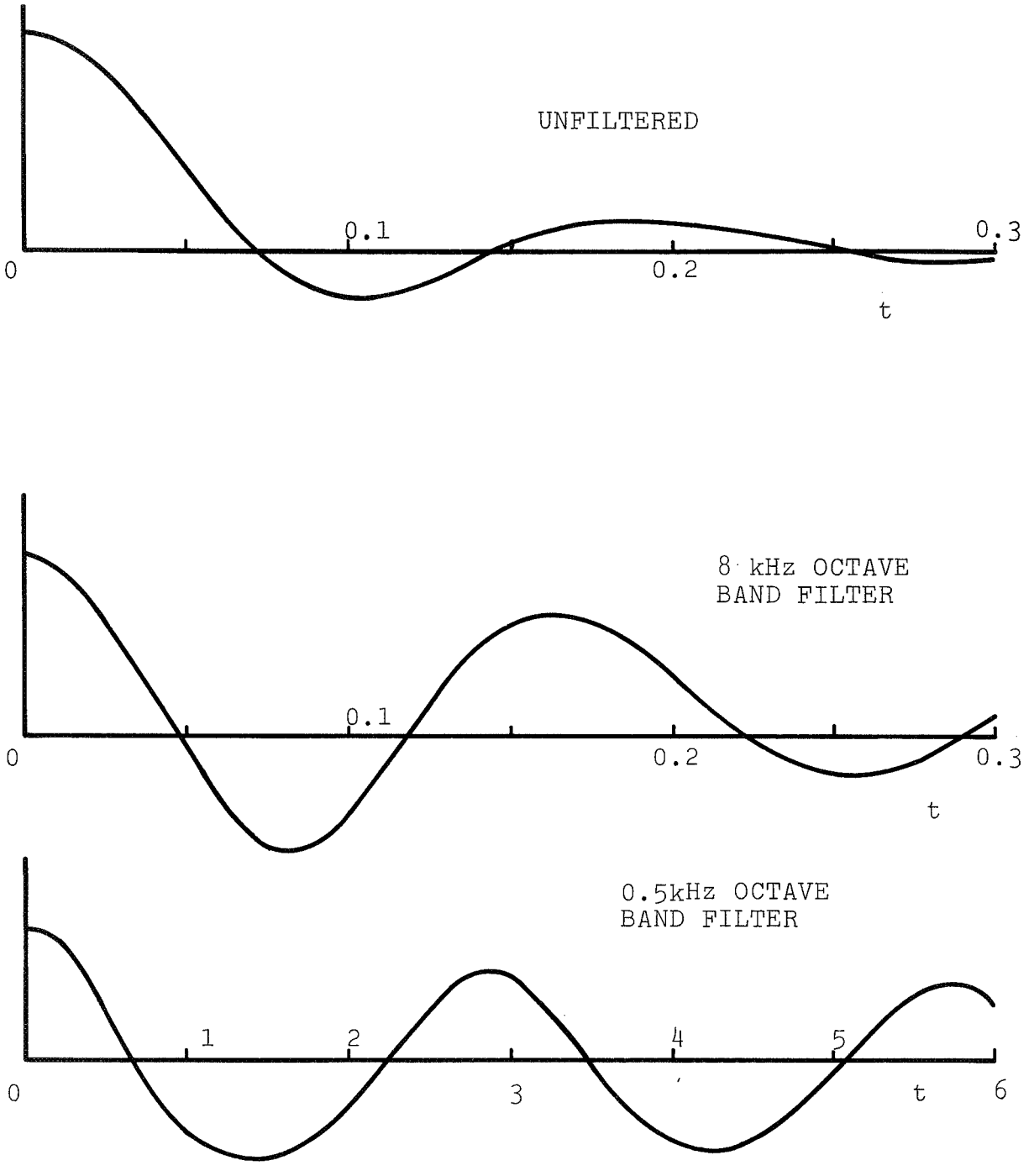

FIG. A-1 AUTOCORRELATIONS AT MICROPHONE #4; HORIZONTAL SCALE, msecs; VERTICAL SCALE, ARBITRARY

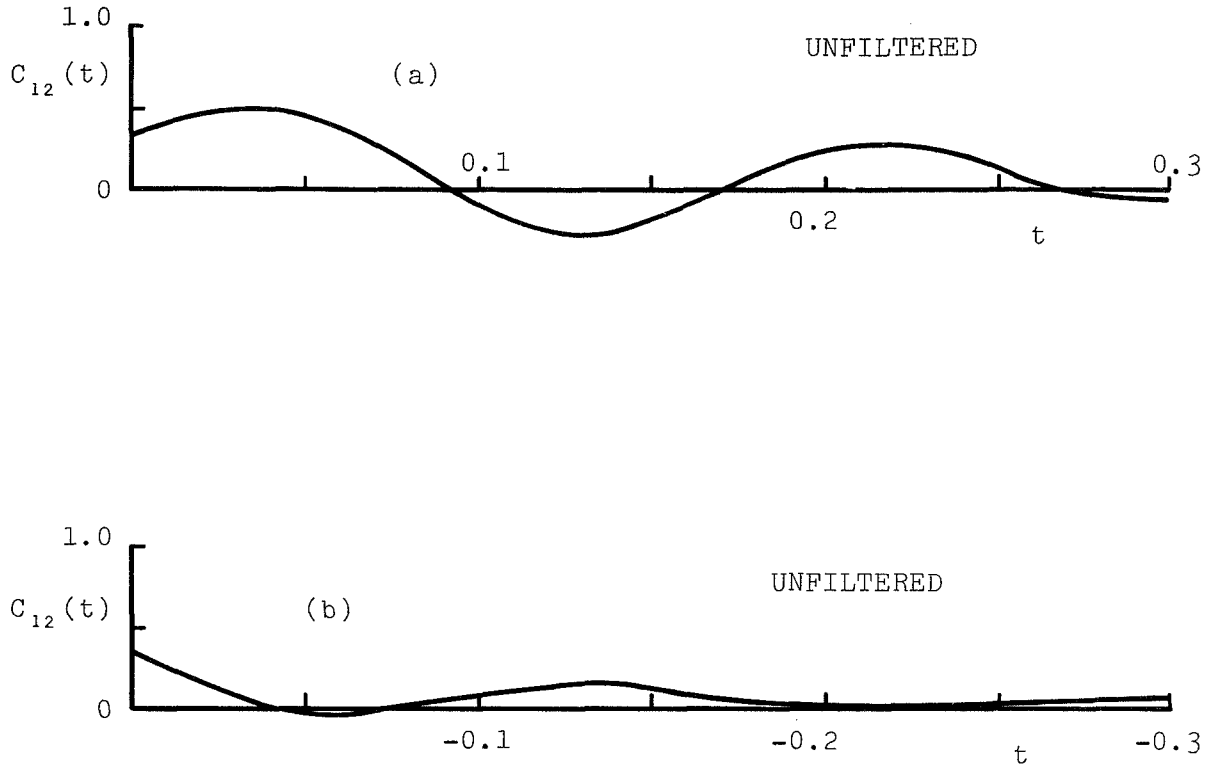

FIG. A-2 CROSS-CORRELATIONS BETWEEN MICROPHONES #1 AND #2; HORIZONTAL SCALE, msecs; VERTICAL SCALE, CROSS-CORRELATION COEFFICIENT; UNFILTERED. (a) MICROPHONE #1 RETARDED. (b) MICROPHONE #2 RETARDED.

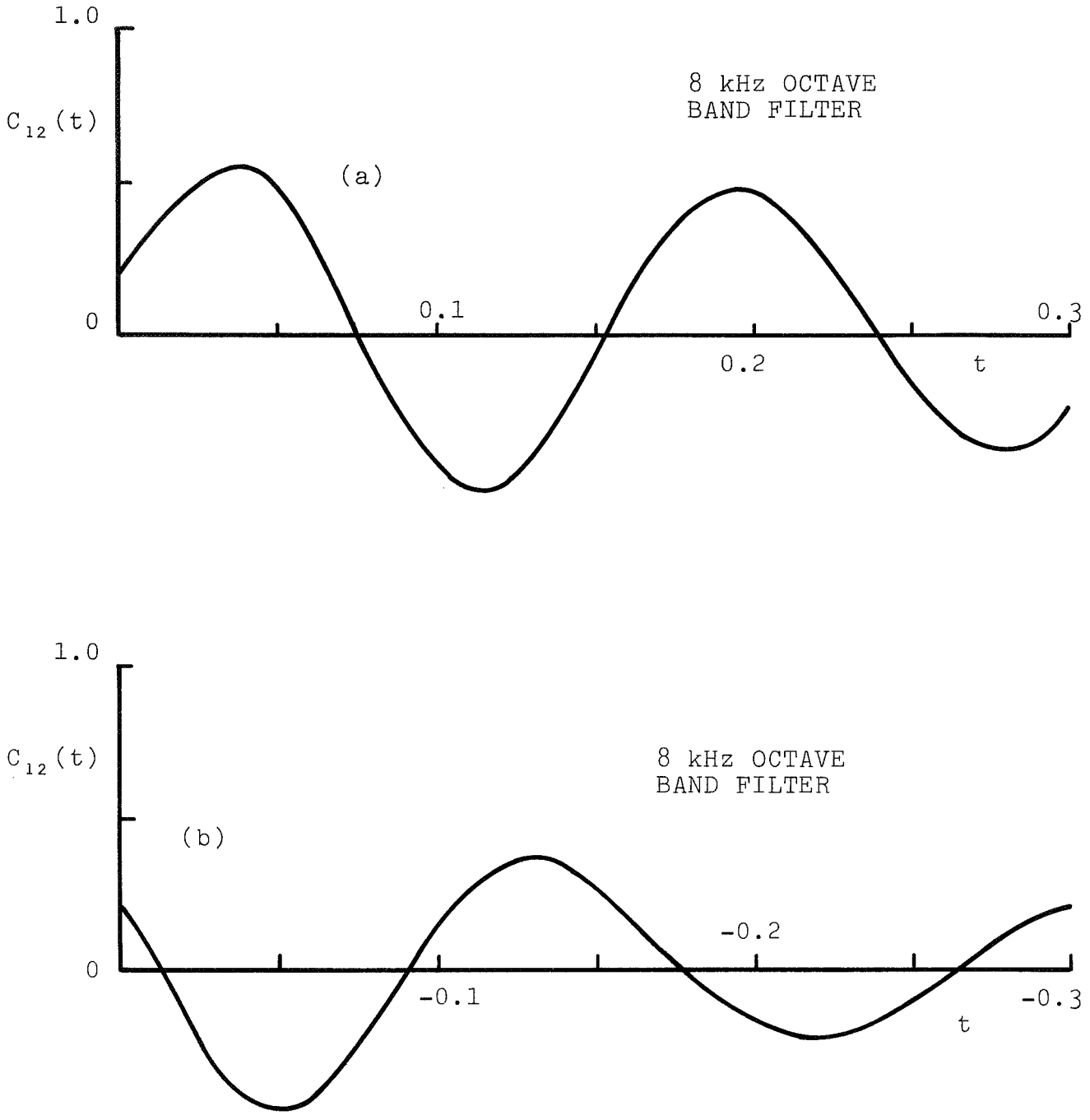

FIG. A-3 CROSS-CORRELATIONS BETWEEN MICROPHONES #1 AND #2; HORIZONTAL SCALE, msecs; VERTICAL SCALE, CROSS-CORRELATION COEFFICIENT; 8 kHz FILTER. (a) MICROPHONE #1 RETARDED. (b) MICROPHONE #2 RETARDED.

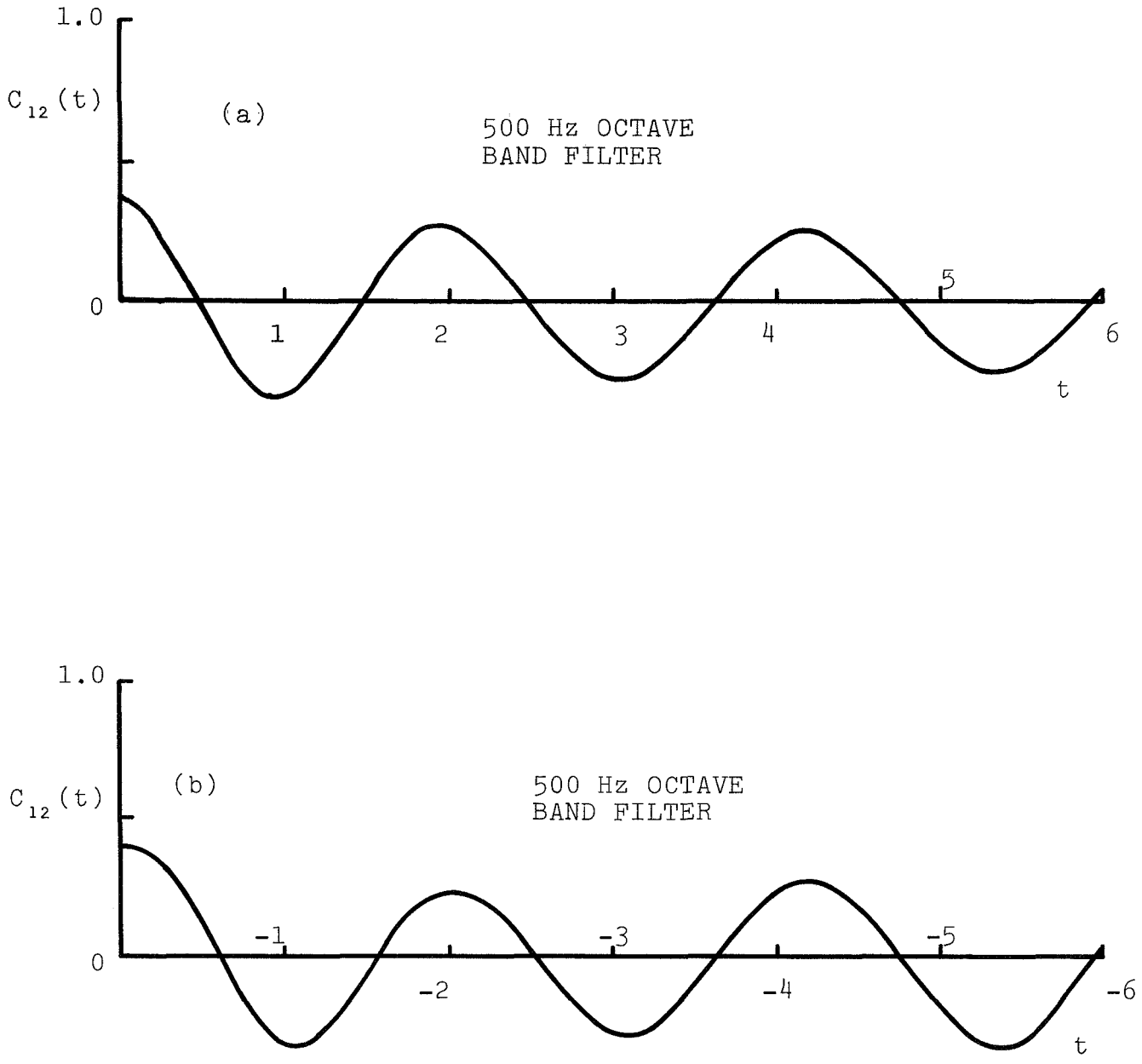

FIG. A-4 CROSS-CORRELATIONS BETWEEN MICROPHONES #1 AND #2; HORIZONTAL SCALE, msecs; VERTICAL SCALE, CROSS-CORRELATION COEFFICIENT; 500 Hz FILTER. (a) MICROPHONE #1 RETARDED. (b) MICROPHONE #2 RETARDED.

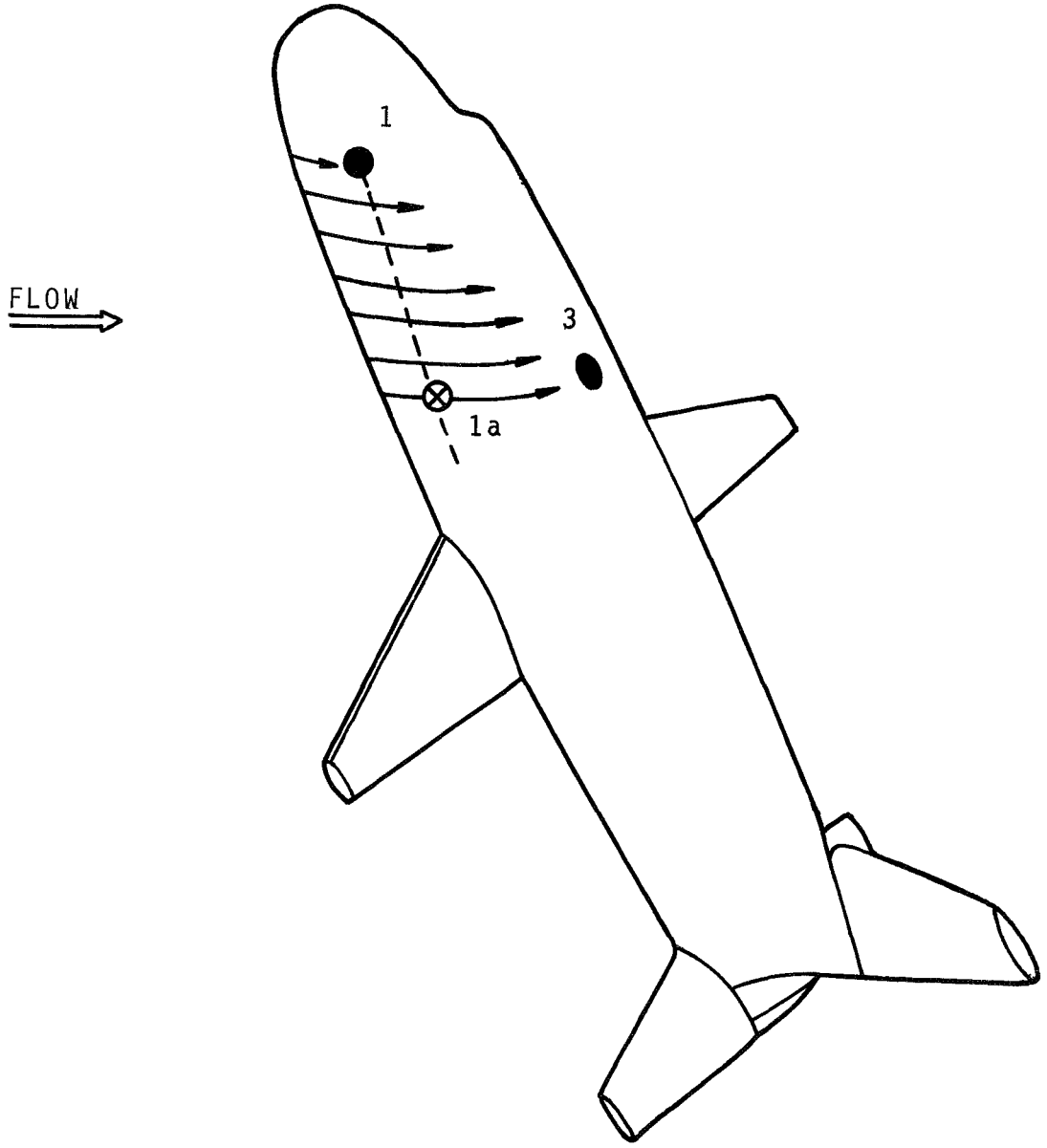

FIG.A-5 SCHEMATIC OF FLOW ON MODEL